EVALUATING THE USE OF TURBIDIMETRY FOR STUDYING FIBRIN STRUCTURAL PROPERTIES

By

Heather A. Belcher

May, 2023

Director of Dissertation: Dr. Nathan E. Hudson

Major Department: Physics

ABSTRACT

A fibrin fiber mesh forms the structural backbone of blood clots. Many pathological conditions result in fibrin gels with altered structural properties, so there is interest in developing rapid and accurate ways to characterize fibrin features. One method of determining the diameter and mass-length ratio of fibers is turbidimetry, which uses light scattering theory for randomly oriented, thin, cylindrical rods to estimate fibrin fiber structural properties from scattering data. There are several different approaches that use turbidimetry to solve for these parameters, each of which has different simplifications and assumptions of full light scattering theory. Although these different approaches are all commonly utilized, the validity of their approximations has not been investigated and the accuracy of the fitting parameters has not been tested against experimental data under a range of physiologically relevant conditions. Therefore, this research will evaluate the accuracy of the commonly utilized turbidimetric approaches by theoretically comparing them to full light scattering theory, and by comparing the acquired diameter values to those obtained experimentally using SEM and super-resolution imaging. The summation of this work will provide a framework for utilizing turbidimetry to study fibrin and pave a path for utilizing turbidimetry in a clinical setting.

EVALUATING THE USE OF TURBIDIMETRY FOR STUDYING FIBRIN STRUCTURAL PROPERTIES

A Dissertation

Presented to the Faculty of the Department of Physics

East Carolina University

In Partial Fulfillment of the Requirements for the Degree

Doctor of Philosophy in Biomedical Physics

By

Heather A. Belcher

May, 2023

Director of Dissertation: Nathan E. Hudson, PhD
Dissertation Committee Members:
Michael Dingfelder, PhD
Martin Guthold, PhD
Elizabeth Ables, PhD
Regina DeWitt, PhD

ACKNOWLEDGEMENTS

I have many people to thank who have given me guidance and support throughout this project. I would like to express my sincerest gratitude to my advisor, Dr. Nathan Hudson, for accepting me into his lab, introducing me to the wonderful world of biophysics, teaching me the skills necessary to complete this project, and encouraging me to pursue this project even though it fell slightly outside of his lab’s usual endeavors.

I would like to thank those who have collaborated with me on this project. Dr. Martin Guthold provided a great deal of ideas which allowed this project to take shape, and also welcomed me to Wake Forest University to learn SEM imaging sample preparation techniques. Dr. Karen Litwa taught me how to perform STORM imaging and analysis of my samples.

I am grateful to the NIH for providing the funding for this project.

I am thankful for the feedback and suggestions of my lab members, especially Grega Popovic who taught me how to perform many of the assays required for my project, Spencer Lynch who taught me how to make fibrin clots for fluorescent imaging, and Nick Kirby for providing feedback on my data analysis.

I am grateful to Dr. Bart Vos for sharing his Python code for the Ferri fitting approach, Dr. Fabio Ferri and Dr. Mattia Rocco for their insight into the conditions required for using turbidimetry, Dr. Lars Øgendal for sharing his knowledge on light scattering theory, Dr. Sean Laverty for assistance on the statistical analysis, and Gabriel Abuna for assistance in using the SEM microscope.

I would like to thank my committee members who have graciously provided their time in reading my dissertation proposal and defense and provided valuable feedback throughout this project. I would like to thank Dr. Jun Lu who was extremely helpful in the beginning stages of

this project, sharing her knowledge of light scattering by small objects, but who we heartbreakingly lost this past year.

Finally, I would like to thank my family whose love and support have driven me throughout my life. I would especially like to thank my grandparents, Ann and Ken Eubank, who have been my biggest supporters throughout my life and pushed me to be my best self. I would like to thank my dad, Wade Hundley, and my sister, Amber Hundley, for listening to me vent and encouraging me when I was overwhelmed. Last, but certainly not least, I would like to thank my amazing husband, Wesley Belcher, who not only provided assistance in my mathematical analyses, but who put up with me and encouraged me when I started to get discouraged or burnt out.

TABLE OF CONTENTS

LIST OF TABLES

LIST OF FIGURES

LIST OF SYMBOLS OR ABBREVIATIONS

A	Absorbance	36
a	Attenuance	36
A(q)	Blob form factor	15
α	Polarizability of particles	7
α_c	Absorption coefficient	36
β	Amplitude of spatial correlations	16
c	Protein concentration	8
$CaCl_2$	Calcium chloride	53
cm	Centimeter	7
cos	Cosine	7
Csc	Cosecant	121
d	Fibrin fiber diameter	6
δ	Fiber density	7
D	Diffusion coefficient	107
Da	Dalton	7
$d_{adjusted}$	Adjusted fiber diameter	69
$d_{CorrYer}$	Diameter obtained from Corrected Yeromonahos approach	69
d_{LST}	Diameter plugged into full light scattering theory equation (Eq. 9) to create theoretical dataset	85
d_{SEM}	Average diameter obtained from SEM imaging	85
d_{turb_exp}	Diameter obtained from fitting turbidimetric approach equations to experimental turbidimetry dataset	85

d_{turb_sim}	Diameter obtained from fitting turbidimetric approach equations to theoretical dataset created with full light scattering theory equation (Eq. 9)	85
δd	Uncertainty in diameter	13
DLS	Dynamic light scattering	53
$\delta\mu$	Uncertainty in mass-length ratio	13
D_m	Mass fractal dimension	16
dn/dc	Specific refractive index increment of solute in solvent	7
<dn/dc>	Spectral average of specific refractive index increment	12
$d\Omega$	Solid angle	9
ξ	Blob/pore size	16
EDM	Euclidean distance map	44
FXIII	Factor XIII	39
FXIIIa	Activated Factor XIII	6
FpA	Fibrinopeptide A	3
FpB	Fibrinopeptide B	3
g	Grams	20
HBS	HEPES buffered saline	12
I_0	Incident light intensity	7
i_θ	Scattered light intensity	7
I_T	Transmitted light intensity	36
J_1	First order Bessel function	8
K	Optical contrast constant	8
k_B	Boltzmann’s constant	107

kDa	Kilodalton	3
k_0	Wave number	121
L	Fiber length	8
L-U	Loewy-units	39
ln	Natural log	37
λ	Wavelength of light	7
μ	Mass-length ratio	6
M	Protein molecular weight	8
mA	Milliamps	41
mAU	Milli-absorbance units	53
mg	Milligrams	20
mL	Milliliters	20
μL	Microliters	40
mm	Millimeters	41
mM	Millimolar	12
μm	Micrometers	20
m_f	Protein mass in one fiber	122
n	Index of refraction of solution	7
$\langle n \rangle$	Spectral average of refractive index of solution	12
N	Number of particles	7
η	Ratio between blob size and average distance between blobs	16
N_A	Avogadro’s number	7
NA	Numerical aperture	48

NaCl	Sodium chloride	53
NIH-U	National Institutes of Health units	39
nm	Nanometers	20
n_p	Index of refraction of protein	7
N_P	Average numbers of protofibrils per cross-section	7
n_s	Index of refraction of solvent	7
OD	Optical density	37
$P(q,L,d)$	Form factor as a function of the wavevector, length, and diameter	8
$P(\theta)$	Form factor as a function of the scattering angle	8
P_{rod}	Scattering function due to fiber length	8
P_{seg}	Segment form factor	15
q	Wavevector	8
q_{max}	Maximum wavevector	117
r	Fiber radius	107
ρ	Fiber density	16
R_g	Radius of gyration	107
R_h	Hydrodynamic radius	107
$R(q)$	Rayleigh ratio as a function of the wavevector	8
r_o	Distance from scattering event that the scattered light is detected	7
$R(\theta)$	Rayleigh ratio as a function of the scattering angle	7
SD	Standard deviation	142
SEM	Scanning electron microscopy	2
Si	Sine integral	8

Sin	Sine	8
$S(q)$	Structure factor	9
S_{sec}	Scattering function due to fiber length	8
STORM	Stochastic optical reconstruction microscopy	2
T	Transmittance	36
T_s	Temperature of the suspension	107
tanh	Hyperbolic tangent	16
θ	Scattering angle	7
τ	Turbidity	9
V	Sample volume	7
ν	Viscosity	107
x	Pathlength	36

PREFACE

Sections of Chapters 1, 2, 3, and 5, as well as Appendix A and B have been published in "Belcher, H.A.; Litwa, K.; Guthold, M.; Hudson, N.E. The Applicability of Current Turbidimetric Approaches for Analyzing Fibrin Fibers and Other Filamentous Networks. *Biomolecules* 2022, 12, 807. http://doi.org/10.3390/biom12060807." [1], of which copyright is retained, and therefore no permission was needed.

CHAPTER 1: INTRODUCTION

Overview

A fibrin fiber network is a major structural component of blood clots. Several different diseases have been linked with altered fibrin structure, so it is important to be able to reliably determine the structure of fibrin fibers. Understanding what impacts fibrin structure could provide insight into these diseases which could potentially lead to better treatment or prevention.

One method of determining the diameter and mass-length ratio of fibrin fibers is with turbidimetry, which involves taking turbidity measurements at several wavelengths on a fully formed clot. However, there are four different commonly utilized turbidimetric fitting approaches, each applying different simplifications of full light scattering theory to obtain different equations for fitting turbidity versus wavelength datasets to obtain fiber diameter and mass-length ratio. Although there are many labs who use turbidimetry for determining fiber structure, there has been no comparison between the four different fitting approaches to determine which is the most accurate, nor has there been any determination as to the limitations of these approaches regarding what clot conditions they are able to reliably provide structural information. Furthermore, there is disagreement in the field on what the best wavelength range is to use for taking turbidimetry measurements, as well as whether it is necessary to account for the wavelength dependence of the refractive index and specific refractive index increment in the fitting equations. This dissertation describes a research program wherein we addressed these questions.

In Chapter 1, the process of fibrin network formation is described, and the full light scattering theory equations used for describing fibrin networks are provided, with a detailed explanation of the four commonly utilized turbidimetric fitting approaches (the Carr-Hermans, Original Yeromonahos, Corrected Yeromonahos, and Ferri approach), with an explanation of the simplifications they each make from full light scattering theory.

In Chapter 2, this work theoretically compares the Carr-Hermans, Original Yeromonahos, and Corrected Yeromonahos approaches to full light scattering theory through the use of simulations in order to determine how accurately the different turbidimetric fitting approaches estimate the fiber diameter and mass-length ratio. This is done for a range of fiber lengths and diameters, for two wavelength ranges commonly utilized for taking measurements, as well as with constant and wavelength corrected values of the refractive index and specific refractive index increment.

In Chapter 3, this work experimentally compares the diameters obtained using the Carr-Hermans, Original Yeromonahos, Corrected Yeromonahos, and Ferri approaches to those obtained from scanning electron microscopy (SEM) and stochastic optical reconstruction microscopy (STORM) for a range of fibrinogen/thrombin concentrations. The analysis of the turbidimetric fitting approaches was done utilizing the same two wavelength ranges investigated theoretically in Chapter 2, as well as the entire wavelength range covering those two. Analysis also included a comparison of results when using constant values for the refractive index and specific refractive index increment, as well as when accounting for the wavelength dependence of those terms.

In Chapter 4, there is a discussion of the congruence between the theoretical results obtained in Chapter 2 and the experimental results in Chapter 3, with an investigation into the cause of any discrepancies between the two.

In Chapter 5, there is an examination of the limitations to full light scattering theory, as well as the experimental limitations of the turbidimetric fitting approaches.

In Chapter 6, a summary of the work is provided, with some possible future directions that this project could take.

By determining the accuracy and limitations of the different turbidimetric fitting approaches, this work is paving a path toward standardization of turbidimetry methodology among different labs and for use in clinical settings.

Fibrin

Fibrin fiber networks are a major component of blood coagulation and wound healing. They are formed when the protein fibrinogen is converted into fibrin by the enzyme thrombin. Fibrinogen is a 340 kDa glycoprotein made up of two sets of three polypeptide chains (an Aα, Bβ, and γ chain), held together by 29 disulfide bonds in a region referred to as the “central nodule” [2]. From the central nodule, the chains then extend into α-helices that form a triple coiled coil structure, terminating with a series of disulfide bonds linking the three chains together. Beyond this the Bβ and γ chains form a compact, globular β-nodule and γ-nodule, respectively, while the Aα chain turns backwards, forming a 4th α-helical structure that continues for part of the coiled coil, before extending into a primarily unstructured region (the αC region) [3]. The αC region is subdivided into the structured αC-domain and the unstructured αC-connector. The fibrinogen structure can be seen in Figure 1A.

To convert fibrinogen to fibrin, the enzyme thrombin cleaves fibrinopeptide A (FpA) from the α chain, exposing knob ‘A’ and in a slower reaction, cleaves fibrinopeptide B (FpB) from the β chain, exposing knob ‘B’ and releasing the αC domain from the center of the molecule, as shown in Figure 1B [2]. Polymerization occurs through the binding of knob ‘A’ to hole ‘a’ in the γ-nodule of a nearby molecule. As this reaction is repeated for many molecules, double stranded polymers called protofibrils form. Electron microscopy studies suggest the formation of half-staggered protofibrils from the center of one molecule binding to the ends of two other molecules, shown in Figure 1C and D [2]. Once the protofibrils are formed, exposure of knob ‘B’ leads to the lateral aggregation of protofibrils into thicker fibers, likely mediated by interactions between the αC regions of the molecules (Figure 1D and E). The formation of fibers continues to form a fibrin network (Figure 1F).

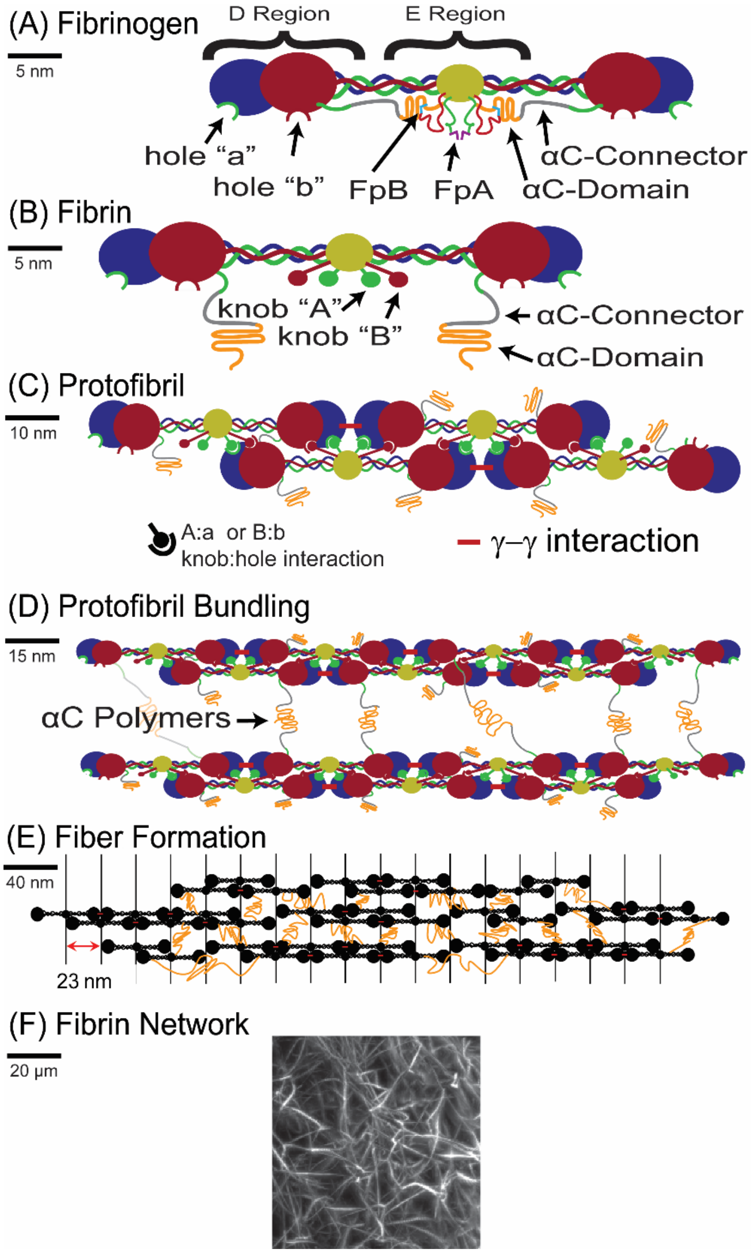

Fig. 1: Schematic of the polymerization process: A) Cartoon of the fibrinogen protein: the α chain is shown in green, β chain in red, and γ chain in blue; the disulfide bond-rich center of the molecule, where all six chains are connected, is depicted in yellow. B) The fibrin molecule: upon thrombin cleavage of FpA and FpB, knob A and knob B are exposed to bind the respective hole a and hole b. C) A half-staggered protofibril grows longitudinally as the knobs in the central region of one molecule bind to the holes in the distal region of two opposite molecules. D) Lateral aggregation of protofibrils, likely mediated by interactions of the αC regions. E) Further aggregation of protofibrils into fibrin fibers. F) A representative image of fibrin fibers in a gel. The image is a maximum intensity projection of a fibrin clot formed from human plasma spiked with 0.1% Alexa-488 labeled fibrinogen, imaged using a Bruker MuVi-SPIM light sheet microscope. Solid black lines on the left of each panel show the approximate scale of features.

Many pathological conditions such as diabetes [4], myocardial infarction [5], ischemic stroke [6], venous thromboembolism [7], and COVID-19 [8] result in gels and fibers with altered structural properties. Therefore, it is important to understand the structure of fibrin fibers and how that relates to fibrin network formation and its function in blood clots. Although the formation of fibrin networks has been studied for over sixty years, there is still much that is unknown. One difficulty is that the structural properties of fibrin, such as fiber length, diameter, mass-length ratio, pore size, and the number of protofibrils per cross-section are determined by many factors including chemical and enzyme concentrations, blood flow rates, and cellular content (such as platelets and tissue-factor bearing cells) [9]. The structural and mechanical properties can also be impacted by the protransglutimanase Factor XIIIa (FXIIIa), which creates cross-links between residues in the γ and α chains of fibrin monomers. This crosslinking has been shown to make the clots less susceptible to fibrinolysis, and to also decrease the elasticity and extensibility of the fibers [3].

Light Scattering Theory

One method for studying fibrin structure and polymerization is turbidity. Turbidity is defined as the fractional decrease of a primary beam's intensity over unit distance due to scattering as it passes through the sample [10]. Turbidity is commonly used to study the kinetics of fibrin gel formation [11], where an increase in turbidity is interpreted as being caused by the bundling of protofibrils into fibers [12].

Turbidity experiments are often performed at different wavelengths in a process referred to as turbidimetry [13]. Turbidimetry can be used on a fully formed fibrin clot to extract fiber properties such as diameter (d) and mass-length ratio (μ) by using simplifications of light scattering theory. The mass-length ratio has been used to estimate the average number of protofibrils per cross-section (N_P) by dividing the mass-length ratio by the mass-length ratio of a single protofibril (1.44*10^{11} Da/cm). The mass-length ratio and diameter can also be used together to determine the fiber density (δ) through the relationship $\mu = \pi\delta\left(\frac{d}{2}\right)^2$.

The Rayleigh ratio, $R(\theta)$, is a quantity (with units of cm^{-1}) used to characterize the scattering intensity at the scattering angle (θ) [14]. It is derived from the Rayleigh-Gans approximation, which assumes the refractive index of the particles (n_p) is close to that of the surrounding medium (n_s). This allows it to be applied to particles that are larger than the Rayleigh scattering limit [15]. The Rayleigh ratio is given by the equation [15]:

$$R(\theta) = \frac{{r_o}^2 i_\theta}{I_0} \qquad [1]$$

where r_o is the distance that the scattered light is observed from the origin, I_0 is the incident light intensity, and i_θ is the scattered light off of N particles in a dilute solution of volume V, given by:

$$i_\theta = \frac{I_0 N N_A}{V}\frac{8\pi^4\alpha^2}{{r_o}^2\lambda^4}(1+\cos^2\theta) \qquad [2]$$

for unpolarized incident light, where N_A is Avogadro's number, λ is the wavelength of the light, and α is the polarizability of particles at concentration c, given by:

$$\alpha = \frac{ncV}{2\pi N N_A}\left(\frac{dn}{dc}\right). \qquad [3]$$

Because polarizability arises due to a difference in the index of refraction between the polymer and the solvent [15], the polarizability is dependent on the index of refraction of the solvent, n (sometimes abbreviated n_s), as well as the specific refractive index increment, $\frac{dn}{dc}$. It is also dependent on the molecular weight, M, which in the equation is put in terms of the protein concentration, c, and volume, V $\left(M = \frac{cV}{N}\right)$.

Plugging Equation 2-3 into Equation 1, and replacing V/N with M/c (since the protein concentration, $c = \frac{NM}{V}$, where M is the molecular weight), and simplifying, the Rayleigh ratio becomes:

$$R(\theta) = \frac{2\pi^2 n^2}{\lambda^4 N_A}\left(\frac{dn}{dc}\right)^2 cM(1 + \cos^2\theta). \qquad [4]$$

$\frac{2\pi^2 n^2}{\lambda^4 N_A}\left(\frac{dn}{dc}\right)^2 (1 + \cos^2\theta) = K$, which is the optical contrast constant, so the Rayleigh ratio is given by:

$$R(\theta) = KcM. \qquad [5]$$

However, this is for the case of small particles that scatter light evenly in all directions. In the case of fibrin fibers, this is not going to be the case. Therefore, a form factor, $P(\theta)$, needs to be introduced to account for the scattering based on the shape of the fibers, so that

$$R(\theta) = KcMP(\theta). \qquad [6]$$

Putting the form factor in terms of the wavevector, $q = \frac{4\pi n}{\lambda}\sin\left(\frac{\theta}{2}\right)$, the Rayleigh ratio becomes [16-18]:

$$R(q) = KcMP(q, L, d). \qquad [7]$$

where for thin circular cylinders, the form factor is given by [18]:

$$P(q, L, d) = \left(\frac{2Si(qL)}{qL} - \left[\frac{\sin(qL/2)}{qL/2}\right]^2\right)\left[\frac{2J_1(qd/2)}{qd/2}\right]^2 \qquad [8]$$

where $\left(\frac{2Si(qL)}{qL} - \left[\frac{\sin(qL/2)}{qL/2}\right]^2\right) = P_{rod}(q, L)$, which is the scattering function due to the length (L) of the cylinders, where the sine integral, $Si(qL) = \int_0^{qL}\frac{sinx}{x}dx$, and $\left[\frac{2J_1(qd/2)}{qd/2}\right]^2 = S_{sec}(q, d)$, which is the scattering due to the width of the cylinders, where J_1 is the first order Bessel function. Note that this equation for the Rayleigh ratio assumes that the network consists of individual cylindrical fibers that do not interact with one another. If we were to assume that the fibers were interacting with one another, we would also need to introduce a structure factor term, $S(q)$, which will be discussed in more detail when describing the Ferri approach, as it is the only one of the approaches accounting for this phenomenon.

The turbidity (τ) is equivalent to the Rayleigh ratio integrated over the entire solid angle, $d\Omega$:

$$\tau = \int R(\theta)\, d\Omega \qquad [9]$$

and since the turbidity is a function of the Rayleigh ratio, which is a function of the diameter and mass-length ratio, the turbidity can be used to obtain the diameter and mass-length ratio.

It should be noted that in the case of vertically polarized incident light, the optical contrast constant is defined as [18]:

$$K = \left(\frac{4\pi^2}{N_A\lambda^4}\right) n^2 \left(\frac{dn}{dc}\right)^2 \qquad [10]$$

in which case the turbidity would then be related to the Rayleigh ratio with the equation:

$$\tau = \int R(\theta)\, \frac{1+\cos^2\theta}{2}\, d\Omega \qquad [11]$$

where $\frac{1+\cos^2\theta}{2}$ is the polarization factor [17]. While the Rayleigh ratio itself is dependent on the polarization, as shown by the change in the optical contrast constant, the turbidity is independent of the polarization, as Equations 9 and 11 are equivalent when inputting the equations for the Rayleigh ratio with the differing definitions of the optical contrast constant.

Turbidimetry Approaches

Because Equation 9 cannot be solved analytically, it must be simplified in order to be applied to experimental data. The different turbidimetric fitting approaches commonly used to determine fibrin fiber diameter and mass-length ratio are those introduced by Carr and Hermans [19], the original approach introduced by Yeromonahos et al. [20], the later corrected version of the Yeromonahos approach [21], and the fractal analysis-based approach introduced by Ferri et al. [18], all of which will be described in more detail in the subsequent sections.

The Carr-Hermans, Original Yeromonahos, and Corrected Yeromonahos approaches all use similar simplifications of full light scattering theory. The first simplification made by all three is that the fibers do not interact with one another, meaning the structure factor, $S(q) = 1$. They then all make the assumption that $\frac{qd}{2} \ll 1$ by assuming the diameter is much less than the wavelength. Then by expanding out the Bessel function in the form factor equation (Equation 8) and keeping only the first two terms, S_{sec} becomes $S_{sec}(q,d) = 1 - \frac{(qd)^2}{16} + \frac{(qd)^4}{1024}$. With the assumption that $\frac{qd}{2} \ll 1$, the last term can be neglected, leading to the approximation that $S_{sec}(q,d) \approx 1 - \frac{(qd)^2}{16}$.

Because the form factor is also dependent on the fiber length, but that is not known without a secondary experimental technique, all three turbidimetric approaches make the assumption that the fibers are infinitely long, which leads them to simplify $Si(qL) \approx \frac{\pi}{2}$ and $\left[\frac{\sin(qL/2)}{qL/2}\right]^2 \approx 0$ allowing them to make the approximation that $P_{rod}(q,L) \approx \frac{\pi}{qL}$. Plugging these approximations back into Equations 7 and 9, and integrating, the turbidity becomes:

$$\tau = \frac{88}{15}\frac{\pi^3}{N_A} n \left(\frac{dn}{dc}\right)^2 \frac{c}{\lambda^3} \mu \left[1 - \frac{23}{77}\pi^2 n^2 d^2 \frac{1}{\lambda^2}\right]. \qquad [12]$$

The validity of the different assumptions made by the turbidimetric fitting approaches is discussed in Appendix A.1.

Carr-Hermans Approach

The first approach being investigated is that described by Carr and Hermans [19] in the late 1970s, which will be referred to as the "Carr-Hermans approach." This approach expanded on earlier works by Ferry in the 1940s [22], Casassa in the 1950s [23], and Marguerie and coworkers in the early 1970s [24]. It uses the above approximations along with the assumption that $\frac{23}{77}\pi^2 n^2 d^2 \frac{1}{\lambda^2} \ll 1$, which then with the use of a Taylor expansion leads to the approximation that $\left[1 - \frac{23}{77}\pi^2 n^2 d^2 \frac{1}{\lambda^2}\right]^{-1} = \left[1 + \frac{23}{77}\pi^2 n^2 d^2 \frac{1}{\lambda^2}\right]$, providing the equation:

$$\frac{c}{\tau\lambda^3} = \frac{N_A}{\left(\frac{88}{15}\right)\pi^3 n \left(\frac{dn}{dc}\right)^2 \mu}\left[1 + \frac{23}{77}\pi^2 n^2 d^2 \frac{1}{\lambda^2}\right]. \qquad [13]$$

The Carr-Hermans approach works by plotting experimental data as $\frac{c}{\tau\lambda^3}$ versus $\frac{1}{\lambda^2}$ and then fitting the data with a linear line. Equation 13 can then be fit to the datasets such that the y-intercept and slope can be used to solve for the diameter and mass-length ratio using the equations:

$$\mu = \frac{N_A}{(88/15)\pi^3 n (dn/dc)^2 yintercept} \qquad [14]$$

$$d = \sqrt{\frac{6776\pi\mu(dn/dc)^2 slope}{345 N_A n}} = \sqrt{\frac{77}{23}\frac{1}{n^2\pi^2}\frac{slope}{yintercept}} \qquad [15]$$

Equation 13, which is the equation used in the Carr and Hermans paper [19], assumes a constant value of n and dn/dc; however, these terms actually contain a wavelength dependence, which can be approximated by the equations [18]:

$$n(\lambda) = A_1 + \frac{B_1}{\lambda^2} \qquad [16]$$

$$\frac{dn}{dc} = A_2 + \frac{B_2}{\lambda^2} \qquad [17]$$

where for HBS buffer (150 mM sodium chloride, 20 mM HEPES, pH 7.4), $A_1 = 1.3264$, $B_1 = 3129.8$, $A_2 = 0.1859$, and $B_2 = 1640$, where λ is in nanometers (the software SEDNTERP [25] was used to determine the equation for n and SEDFIT [26,27] was used to determine the equation for dn/dc, as described in more detail in Appendix A.2).

Now since n and dn/dc contain a wavelength dependence, it is necessary to change the plot format so that the slope and y-intercept do not contain the n(λ) or dn/dc(λ) terms. This can be done by plotting the data as y' versus x' where [18]:

$$y' = \frac{\left[\frac{dn}{dc}(\lambda)\right]^2}{\langle\frac{dn}{dc}\rangle^2} \frac{n(\lambda)}{\langle n\rangle} \frac{c}{\tau\lambda^3} \qquad [18]$$

$$x' = \frac{[n(\lambda)]^2}{\langle n\rangle^2} \frac{1}{\lambda^2} \qquad [19]$$

where <n> and <dn/dc> are the spectral averages of the refractive index and specific refractive index increment, respectively, solved for using the equations:

$$\langle n\rangle = \frac{1}{\lambda_2 - \lambda_1} \int_{\lambda_1}^{\lambda_2} n(\lambda) d\lambda \qquad [20]$$

$$\langle\frac{dn}{dc}\rangle = \frac{1}{\lambda_2 - \lambda_1} \int_{\lambda_1}^{\lambda_2} \frac{dn}{dc}(\lambda) d\lambda. \qquad [21]$$

The mass-length ratio and diameter can then be solved for using the equations:

$$\mu = \frac{N_A}{(88/15)\pi^3 <n><dn/dc>^2 yintercept} \qquad [22]$$

$$d = \sqrt{\frac{6776\pi\mu <dn/dc>^2 slope}{345 N_A <n>}} = \sqrt{\frac{77}{23} \frac{1}{<n>^2\pi^2} \frac{slope}{yintercept}}. \qquad [23]$$

The uncertainty in the diameter and mass-length ratio can be obtained using uncertainty propagation, such that:

$$\delta d = \sqrt{\begin{array}{c}\left(\frac{1}{2}\left(\frac{77}{23}\frac{1}{<n>^2\pi^2}\right)^{\frac{1}{2}}\left(\frac{slope}{yintercept}\right)^{-\frac{1}{2}}\frac{1}{yintercept}\right)^2 \delta slope^2 \\ +\left(-\frac{1}{2}\left(\frac{77}{23}\frac{1}{<n>^2\pi^2}\right)^{\frac{1}{2}}(slope)^{\frac{1}{2}}(yintercept)^{-\frac{3}{2}}\right)^2 \delta yintercept^2\end{array}} \qquad [24]$$

$$\delta\mu = \frac{N_A}{(88/15)\pi^3<n><dn/dc>^2}\frac{1}{yintercept^2}\delta yintercept. \qquad [25]$$

Original Yeromonahos Approach

The next approach being investigated is that introduced by Yeromonahos et al. [20] in 2010. It is very similar to that of Carr and Hermans except they do not make the assumption that $\frac{23}{77}\pi^2 n^2 d^2 \frac{1}{\lambda^2} \ll 1$, so they use Equation 12 as their final equation. Rewriting this equation, it becomes:

$$\tau\lambda^5 = \frac{88}{15}\frac{1}{N_A}\pi^3 cn\left(\frac{dn}{dc}\right)^2 \mu\left[\lambda^2 - \frac{184}{154}\pi^2 n^2\left(\frac{d}{2}\right)^2\right] \qquad [26]$$

although the $\frac{1}{N_A}$ term is left out of the equation as given in the Yeromonahos paper. Then the Yeromonahos method works by plotting experimental data as $\tau\lambda^5$ versus λ^2 and fitting the data with a linear line. The slope and y-intercept are then plugged into Equation 26 to solve for the diameter, and the mass-length ratio, such that:

$$\mu = \frac{slope}{(88/15)\pi^3(1/N_A)cn(dn/dc)^2} \qquad [27]$$

$$d = 2\sqrt{\frac{-yintercept}{B*slope}} \qquad [28]$$

where $B = \frac{184}{154}\pi^2 n^2$.

Although Yeromonahos supplied a Letter to the Editor correcting this equation in her dissertation which was completed the following year [21], Equation 26 is still commonly used within the fibrinogen community today [28-30], so this approach will still be investigated.

Equation 26 will be referred to as the “Original Yeromonahos” approach and the corrected version will be referred to as the “Corrected Yeromonahos” approach.

As with the Carr-Hermans approach, this approach assumes a constant value of n and dn/dc. In order to account for the wavelength dependence of these terms, it is necessary to change the plot format to y’ versus x’ where [31]:

$$y' = \frac{\tau\lambda^5}{\frac{88}{15}\pi^3 n(\lambda)^3 c \frac{1}{N_A}\frac{dn}{dc}(\lambda)^2} \qquad [29]$$

$$x' = \frac{\lambda^2}{n(\lambda)^2}. \qquad [30]$$

The mass-length ratio and diameter can then be solved for using the equations:

$$\mu = slope \qquad [31]$$

$$d = 2\sqrt{\frac{-yintercept}{B\prime * slope}} \qquad [32]$$

where $B' = \frac{184}{154}\pi^2$.

The uncertainty in the diameter and mass-length ratio can be obtained using uncertainty propagation, such that:

$$\delta d = \sqrt{\begin{matrix} \left(-\left(\frac{1}{B\pi^2}\right)^{\frac{1}{2}}(-yintercept)^{\frac{1}{2}}(slope)^{-\frac{3}{2}}\right)^2 \delta slope^2 \\ +\left(-\left(\frac{1}{B\pi^2}\right)^{\frac{1}{2}}(-yintercept)^{-\frac{1}{2}}(slope)^{-\frac{1}{2}}\right)^2 \delta yintercept^2 \end{matrix}} \qquad [33]$$

$$\delta\mu = \delta slope. \qquad [34]$$

Corrected Yeromonahos Approach

The Corrected Yeromonahos approach [21] changes the 184/154 term of the original equation (Equation 26) by a factor of 2/3, leading to the fitting equation:

$$\tau\lambda^5 = \frac{88}{15}\frac{1}{N_A}\pi^3 cn\left(\frac{dn}{dc}\right)^2 \mu\left[\lambda^2 - \frac{184}{231}\pi^2 n^2\left(\frac{d}{2}\right)^2\right] \qquad [35]$$

Then experimental data is plotted as $\tau\lambda^5$ versus λ^2 and fit with a linear line. The slope and y-intercept of the linear fit line are then plugged into Equation 35 to solve for the diameter and mass-length ratio, such that μ and d are given by Equations 27-28, except that now $B = \frac{184}{231}\pi^2 n^2$.

The change in the 184/154 term is described as being due to averaging the form factor, P(q,L,d), over all solid angles [21]; however, it was done so erroneously, as discussed in more detail in Appendix A.3. Thus the "corrected" equation still has its flaws.

Again, Equation 35 is assuming constant values of n and dn/dc. In order to account for the wavelength dependence of those terms, the plot format can be changed to y' and x', using Equations 29-30, except that now $B' = \frac{184}{231}\pi^2$.

Ferri Approach

The final turbidimetry approach being investigated is that described by Ferri et al. in 2015 [18]. Unlike the previous three methods, this one considers the fibers to be fractal "blobs" rather than noninteracting individual fibers. This makes the Rayleigh ratio a little more complicated, as it now includes the structure factor term, $S(q)$, which was ignored by the previous methods, and also introduces a blob form factor term, $A(q)$, so that the Rayleigh ratio becomes:

$$R(q) = KCMS(q)A(q)P_{seg}(q) \qquad [36]$$

where K, C, and q are the same as earlier defined (using Equation 10 for K). The molecular weight is now the blob molecular weight, given as:

$$M \approx N_A \frac{\rho\pi}{4} \xi^{D_m} d^{3-D_m} \quad [37]$$

where ρ is the density, ξ is the blob size, assumed to be equivalent to the pore size, and D_m is the mass fractal dimension.

The structure factor, $S(q)$, is given by:

$$S(q) = 1 - \beta \exp\left(-\frac{q^2\xi^2}{4\pi\eta^2}\right) \quad [38]$$

where β is a dimensionless parameter controlling the amplitude of spatial correlations, and η is the ratio between the blob size and the average distance between blobs, both assumed to be 1.

The blob form factor, $A(q)$, is given by:

$$A(q) = \frac{1}{\left[1+\left(\frac{q\xi}{\delta(D_m)}\right)^2\right]^{D_m/2}} - \frac{(d/\xi)^{D_m}}{\left[1+\left(\frac{qd}{\delta(D_m)}\right)^2\right]^{D_m/2}} + (d/\xi)^{D_m} \quad [39]$$

where

$$\delta(D_m) = \pi - 0.38\left[\frac{\tanh\left[\frac{D_m-1.44}{0.1}\right]+1}{2}\right]^{0.5}. \quad [40]$$

The segment form factor, $P_{seg}(q)$, is:

$$P_{seg}(q) = \left[\frac{2Si(qd)}{qd} - \left(\frac{\sin(qd/2)}{(qd/2)}\right)^2\right]\left[\frac{2J_1(qd/2)}{(qd/2)}\right]^2. \quad [41]$$

Equation 11 with this new definition of the Rayleigh ratio can then be fit to a turbidity versus wavelength dataset to extract the diameter and mass-length ratio. However, a secondary experimental technique, such as confocal imaging, has to first be used to determine the pore size and mass fractal dimension in order to be able to input those values into the equation prior to fitting them to turbidimetry data.

Conclusion

To conclude, turbidimetry is a measure of light scattering at various wavelengths and can be utilized for determining the individual fibrin fibers making up a fibrin network by applying light scattering theory equations to the dataset. However, the full light scattering theory equations involve an integral that cannot be solved analytically, and therefore must be simplified in order to be applied to an experimental dataset. There are four commonly utilized turbidimetric fitting approaches used in determining the structure of fibrin fibers: those introduced by Carr and Hermans [19], Yeromonahos et al. [20], a “corrected” version of that introduced by Yeromonahos et al. [21], and that introduced by Ferri et al. [18], each making different simplifications of full light scattering theory. The Carr-Hermans, Original Yeromonahos, and Corrected Yeromonahos approaches all make the assumption that the fibers are infinitely long and thin compared to the wavelengths being used for measurement, and that the individual fibers do not interact with one another, but they apply different simplifications to the full light scattering theory equation based on these assumptions, resulting in slightly different fitting equations. The Ferri approach is more complex than the other three approaches in that it assumes that the fibers do interact with one another, forming a three-dimensional “blob” and thus uses a more complex equation for the Rayleigh ratio. This more advanced equation requires knowledge of the pore size and mass fractal dimension, which must be determined by a secondary experimental technique, such as confocal imaging.

Since each of these different fitting approaches has been used in some capacity for determining the structure of fibrin fibers, it is necessary to determine which is the most accurate, and under what conditions they are no longer reliable. In order to determine the accuracy of these different turbidimetric fitting approaches, this work utilizes simulations comparing the results from these fitting equations to those from full light scattering theory (see Chapter 2), as well as experimental comparisons between the diameter values obtained using the different turbidimetric approaches to those from SEM and super-resolution fluorescence imaging (see Chapter 3). This was done for a variety of experimental conditions in order to determine which approach and experimental conditions should be used to obtain the most reliable results.

CHAPTER 2: THEORETICAL ANALYSIS OF TURBIDIMETRIC APPROACHES

Introduction

This work theoretically assesses the accuracy of three turbidimetric fitting approaches commonly utilized for analyzing fibrin fiber structure: the Carr-Hermans (Equation 13), Original Yeromonahos (Equation 26), and Corrected Yeromonahos (Equation 35) approaches. Each of these approaches has been derived based on simplifications of light scattering theory (Equations 7-9) and assumptions about the structural arrangements of fibers within a clot, as described in Chapter 1. Therefore, in order to determine the accuracy of these three approaches, numerical simulations were used to compare the fitting approaches to full light scattering theory.

This work also used simulations to investigate the effects of wavelength range and correcting for the wavelength dependence of the refractive index and specific refractive index increment on the accuracy of turbidimetry results.

The Ferri approach was not evaluated here due its use of a slightly altered equation for the Rayleigh ratio (Equation 36) and its need for additional experimental techniques other than turbidimetry to determine the pore size and mass fractal dimension, making it difficult to compare theoretically with the other approaches.

While this chapter focuses on theory to analyze the accuracy of the turbidimetric approaches, an experimental analysis was also performed, as discussed in Chapter 3, and a comparison between the results obtained using the simulations and those obtained experimentally are provided in Chapter 4.

Methods

Data were numerically generated using a custom code in Mathematica (Wolfram, Champaign, IL). Numerical integration was done to create a turbidity dataset using full light scattering theory (Equations 7-9) for a fibrinogen concentration of 0.0001 g/mL, and mass-length ratio of $4.73*10^{12}$ Da/cm, with diameters ranging from 10-200 nm, every 10 nm, and lengths ranging from 0.5-10 μm, every 0.5 μm. The diameter and length ranges were chosen based on findings by Ryan et al. [32] that fibers for conditions similar to blood (fibrinogen concentration of 3 mg/mL, pH of 7.5) contain fibrin fibers with average lengths of 0.3-4.8 μm and average diameters of 44-147 nm, as well as findings by Pretorius et al. [33] that fibrin fibers for healthy patients have average diameters of 89.97±44.16 nm, while stroke patients have fibrin fibers with diameters of 27.37±17.03 nm. The fibrinogen concentration and mass-length ratio were chosen to match values used by Ferri et al. [18]; however, the results are independent of both parameters, as discussed later in this chapter. To confirm the Mathematica numerical integration was correct, we also performed a trapezoidal rule numerical summation, which generated similar results, as discussed in more detail in Appendix B.1.

Since many papers in the turbidimetry literature use constant values for the index of refraction (n) and specific refractive index increment (dn/dc) (for example, see [13,19,20]), ignoring the wavelength dependence of those terms, we compared the percent error in the fitting approach values when using constant values for n and dn/dc to the percent error in the values when accounting for the wavelength dependence of those terms. Therefore, with data from the full light scattering theory in hand, datasets for either $\frac{c}{\tau\lambda^3}$ versus $\frac{1}{\lambda^2}$ (Carr-Hermans) or $\tau\lambda^5$ versus λ^2 (Yeromonahos) were created to test the standard fitting equations using constant values of n

and dn/dc, as well as datasets for $\frac{\left[\frac{dn}{dc}(\lambda)\right]^2}{\langle\frac{dn}{dc}\rangle^2}\frac{n(\lambda)}{\langle n\rangle}\frac{c}{\tau\lambda^3}$ versus $\frac{[n(\lambda)]^2}{\langle n\rangle^2}\frac{1}{\lambda^2}$ (Carr-Hermans) or $\frac{\tau\lambda^5}{\frac{88}{15}\pi^3 n(\lambda)^3 c\frac{1}{N_A}\frac{dn}{dc}(\lambda)^2}$ versus $\frac{\lambda^2}{n(\lambda)^2}$ (Yeromonahos). Values for HEPES Buffered Saline (HBS), a buffer commonly used to study fibrin, were used in Equations 16-17 to determine $n(\lambda)$ and $\frac{dn}{dc}(\lambda)$. For the constant values of n and dn/dc, the values at 633 nm were chosen, as that is what Carr and Hermans used in their work [19].

Using a custom Mathematica code, the data were then fit with the Carr-Hermans, Original Yeromonahos, or Corrected Yeromonahos equations (Equations 13, 26, and 35, respectively). The diameter and mass-length ratio obtained from the linear fits, and the percent error between the value obtained from the fits and the value used to create the dataset using full light scattering theory were determined. A parameter sweep was then used to calculate the percent error for physiologically relevant fiber length and diameter values, based on the values provided by Ryan et al. [32], which was then plotted in a 3D heatmap using a “bar3” command in MATLAB (The Mathworks Inc., Natick, MA).

Analysis was performed using a wavelength range of 350-650 nm, which is the wavelength range used in the original Carr-Hermans paper [19], as well as a wavelength range of 500-800 nm, which is used by the Yeromonahos approaches [20,21], in order to determine which wavelength range provides more accurate results.

An outline of the methods used for analysis are shown in Figure 2.

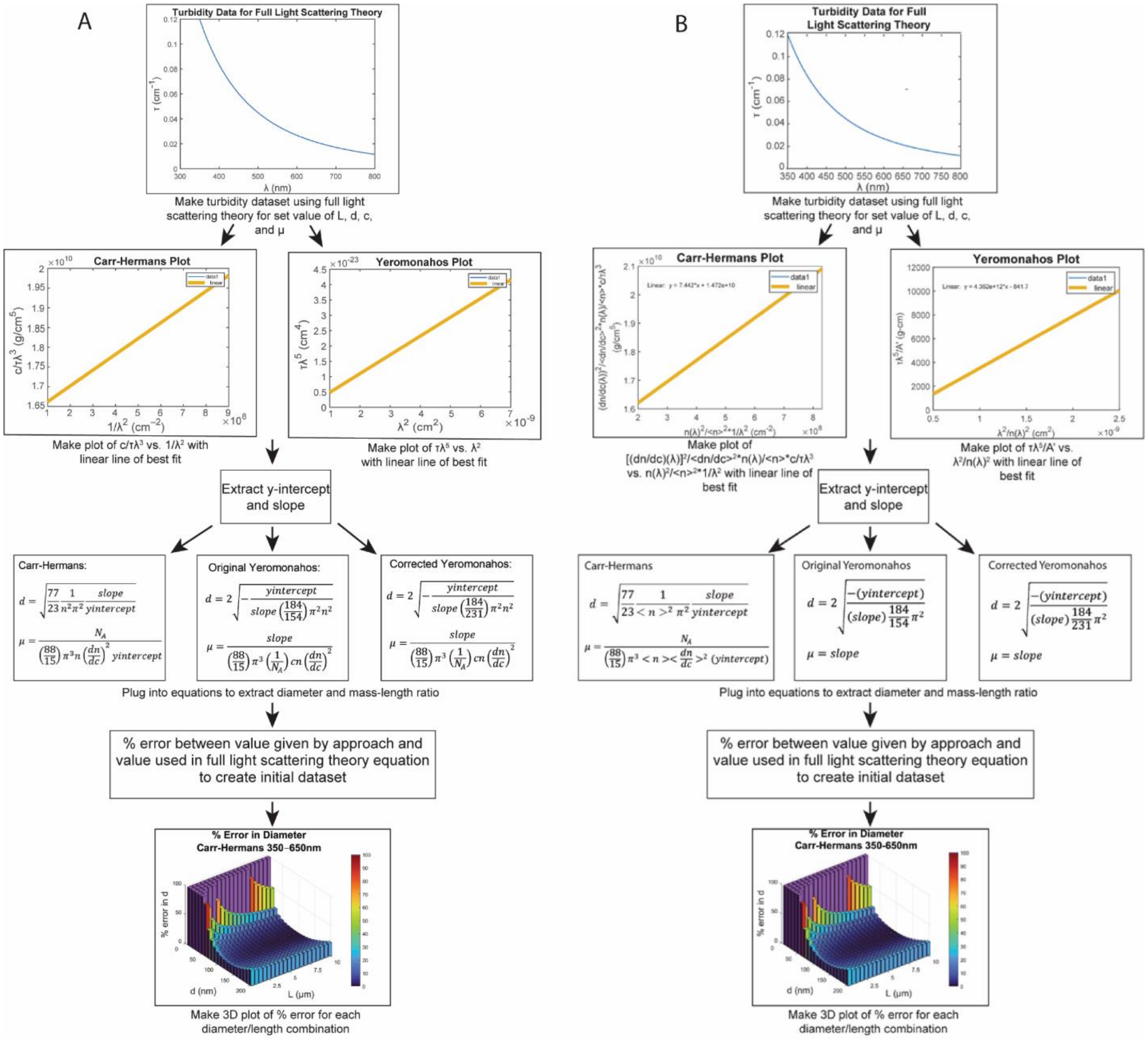

Fig. 2: An outline of the methods for determining the percent error in each turbidimetric approach using A) constant values of n and dn/dc, and B) wavelength-dependence corrected values of n and dn/dc.

Results and Discussion

Wavelength Dependence of n and dn/dc

As mentioned previously, in fitting experimental data with the different turbidimetric approaches, constant values of n and dn/dc are commonly utilized, ignoring their dependence on the wavelength. It was found experimentally by Vos [34] that using constant values for n and dn/dc rather than accounting for the wavelength dependence of those terms can lead to an average difference of 24% in the calculated fiber radius and 3% in the calculated mass-length ratio for fibers with diameters ranging from 110.4 to 218.8 nm. However, the change in the obtained diameter was not compared to light scattering theory or another experimental technique, so we wanted to determine how the accuracy of the obtained diameter changes by accounting for the wavelength dependence of those terms versus using a constant value.

Figures 3 and 4 below show the effect of using constant values of n and dn/dc in the different fitting approaches compared with using wavelength dependence-corrected values in the calculation of the diameter and mass-length ratio, respectively. The original dataset created using full light scattering theory was always corrected for the wavelength dependence of n and dn/dc regardless of whether the fitting approach was. Equations 16-17 were used with the values provided for HBS buffer for the wavelength-corrected values of n and dn/dc. For the constant values of n and dn/dc, the values at 633 nm were used (n=1.3344, dn/dc=0.1901), as that is what Carr and Hermans used in their seminal paper [19]. The error was also determined using the spectrally averaged values of n and dn/dc for both wavelength ranges, although that yielded very similar results as using 633 nm values, and is therefore not shown.

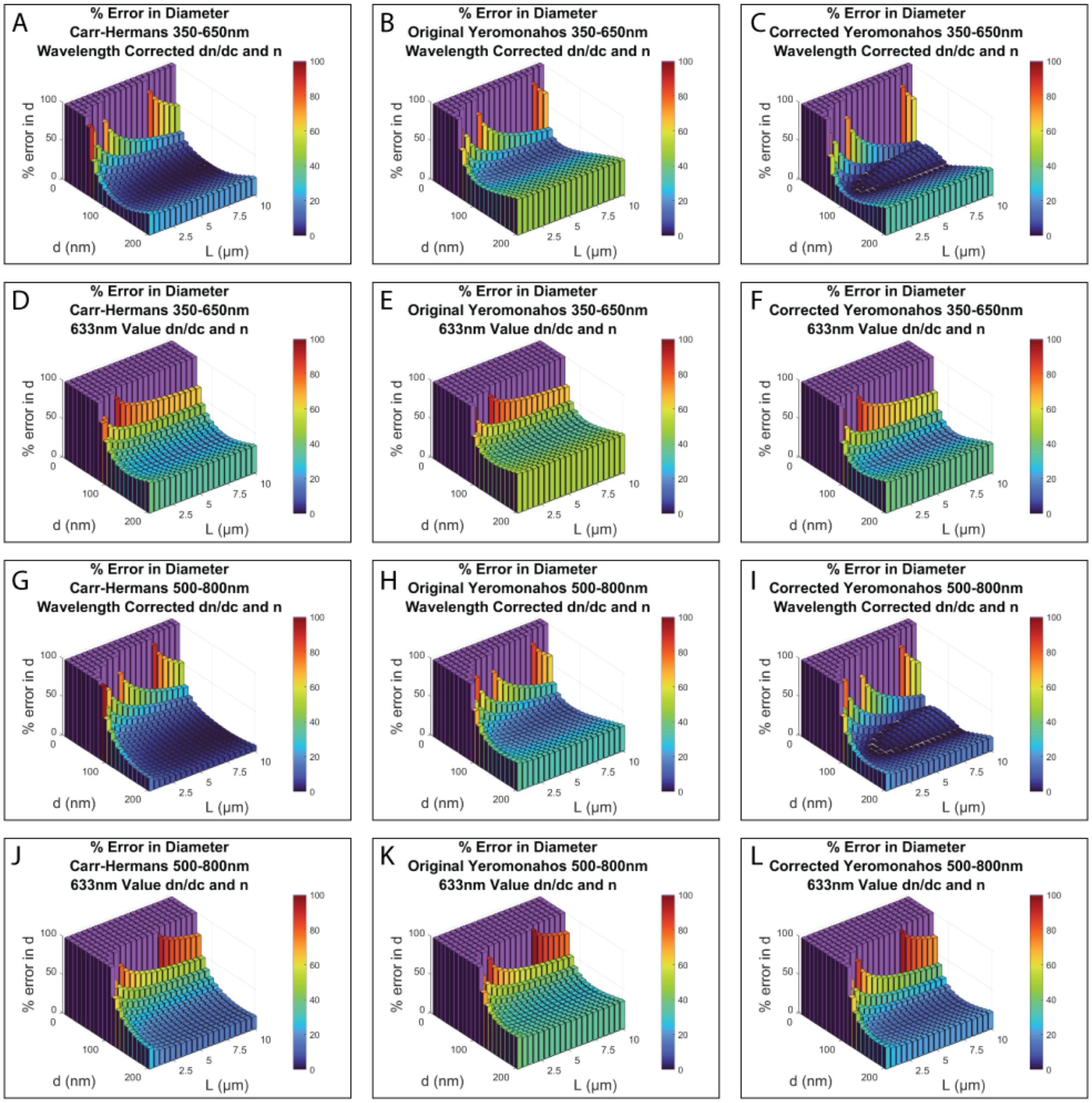

Fig. 3: The percent error in the diameter between the value used to create the full light scattering theory dataset (using Equations 7-9) and the values obtained using the Carr-Hermans (left column), Original Yeromonahos (middle column), and Corrected Yeromonahos (right column) approaches (Equations 13, 26, and 35, respectively), for wavelength ranges of 350-650 nm and 500-800 nm, using wavelength corrected values of n and dn/dc (A-C, G-I), and constant values of n and dn/dc at 633 nm (D-F, J-L). (d=10-200 nm, L=0.5-10 μm, c=0.0001 g/cm^3, μ=4.73*10^{12} Da/cm, values of dn/dc and n for HBS buffer; purple bars represent imaginary values and were assigned 100% error for plotting purposes).

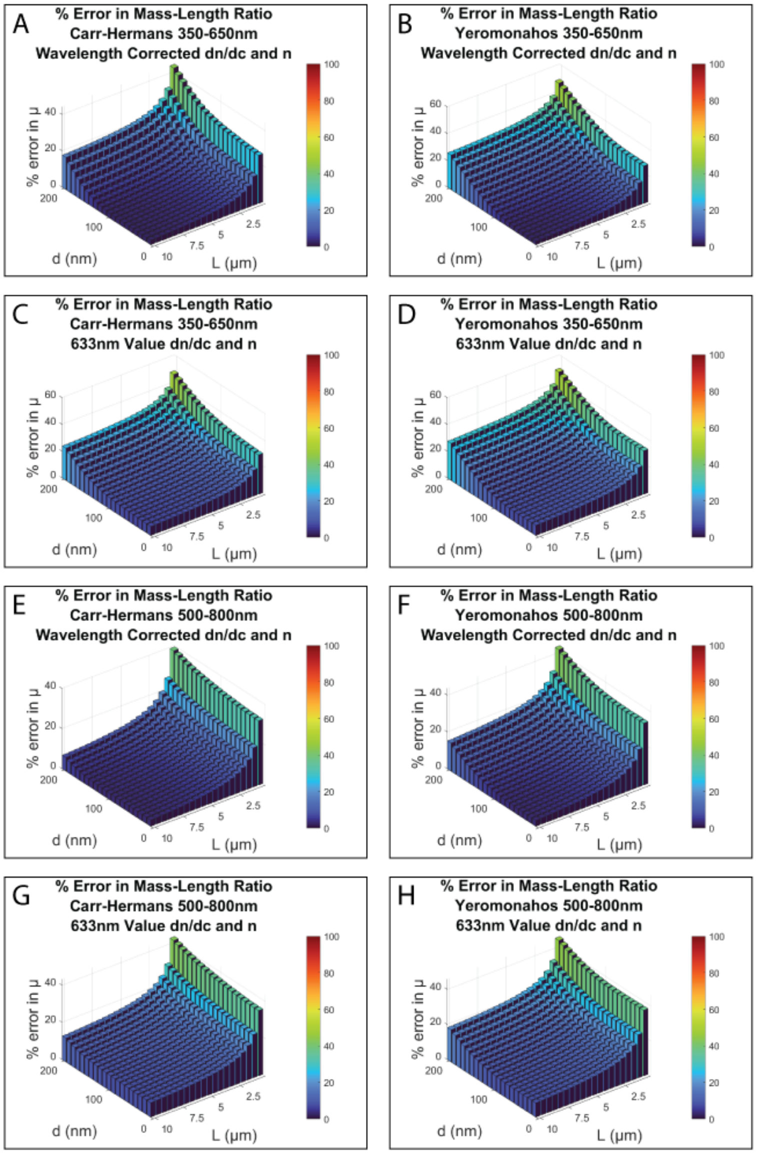

Fig. 4: The percent error in the mass-length ratio between the value used to create the full light scattering theory dataset (using Equations 7-9) and the values obtained using the Carr-Hermans (left column), and Original and Corrected Yeromonahos (right column) approaches (Equations 13, 26, and 35, respectively), for wavelength ranges of 350-650 nm and 500-800 nm, using wavelength corrected values of n and dn/dc (A-B, E-F), and constant values of n and dn/dc at 633 nm (C-D, G-H). (d=10-200 nm, L=0.5-10 µm, c=0.0001 g/cm^3, µ=4.73*10^{12} Da/cm, values of dn/dc and n for HBS buffer).

As seen in Figures 5 and 6, using a constant value for n and dn/dc results in significantly increased error in the calculations of both the diameter and mass-length ratio compared to when accounting for the wavelength dependence of the two terms. This is the case for all three approaches, at both wavelength ranges investigated. This increased error is particularly apparent for smaller diameter values, and especially in the calculation of the diameter. A summary of the average difference in the percent error values when using a constant n and dn/dc compared to using wavelength corrected values is provided in Table 1 for each of the different approaches and wavelength ranges.

Average Difference in Percent Error of Values with Constant n and dn/dc and Wavelength Corrected n and dn/dc		
Approach	**Diameter**	**Mass-Length Ratio**
Carr-Hermans 350-650 nm	33%	5%
Carr-Hermans 500-800 nm	25%	5%
Original Yeromonahos 350-650 nm	24%	3%
Original Yeromonahos 500-800 nm	20%	4%
Corrected Yeromonahos 350-650 nm	28%	3%
Corrected Yeromonahos 500-800 nm	23%	4%

Table 1: Average difference in percent error for diameter and mass-length ratio calculated from numerical simulations with constant values of n and dn/dc (values at 633 nm) and wavelength-dependence corrected values of n and dn/dc (for HBS buffer).

Due to the increased error when using a constant value for n and dn/dc, for all subsequent results the full light scattering theory equation was corrected for wavelength dependence when creating the initial theoretical turbidity dataset, and the approaches were also corrected for wavelength dependence when being fit to the dataset.

Wavelength Range Effects

As mentioned earlier, Carr and Hermans [19] used a wavelength range of 350-650 nm in their work, while Yeromonahos et al. [20] used a wavelength range of 500-800 nm. García et al. [31] argued that it is not as necessary to correct for the wavelength dependence of n and dn/dc if using a wavelength range of 500-800 nm because there is a lesser wavelength dependence of the parameters in that wavelength range than there is at lower wavelengths.

As discussed in more detail in Appendix B.2, it is true that there is less variability in the values of n and dn/dc with changing wavelengths across the wavelength range of 500-800 nm than there is across the wavelength range of 350-650 nm; however, as discussed in the previous section there is still a significant amount of added error in the calculations of the diameter and mass-length ratio with this wavelength range when using constant values for those terms, so it is still necessary to account for their wavelength dependence in order to obtain reliable results.

The percent error in the values of the diameter using each of the three approaches for both wavelength ranges can be seen in Figure 5. All three approaches result in imaginary diameter values for thin fibers (diameters less than ~50 nm) for both wavelength ranges, shown by the purple bars and assigned a percent error value of 100% for plotting purposes. For thicker fibers (diameters of 150-200 nm), all three approaches show better fits with the 500-800 nm wavelength range. The Carr-Hermans approach and the Corrected Yeromonahos approach for the two wavelength ranges work well for fibers of intermediate thickness (diameters over a range of 50-150 nm), and the Carr-Hermans approach with a wavelength range of 500-800 nm is best for thicker fibers (with diameters of 150-200 nm). Some diameter values obtained with the three approaches across this range of diameters and lengths are shown in Appendix B.3. The Carr-Hermans approach and the Original Yeromonahos approach always result in underestimated values of the diameter when compared to the values used to create the dataset using full light scattering theory for all of the diameter/length combinations investigated. The Corrected Yeromonahos approach results in mostly underestimated diameter values, except for the area of increased error at intermediate diameters (~50-150 nm) seen in Figure 5, in which it is overestimating the diameter values. Because the percent error involves taking the absolute value of the difference in the diameter value used to create the initial dataset using full light scattering theory and the calculated value obtained from the fit, the transition from under- to overestimating the diameter results in the “saddle” feature seen in panels C and F.

A summary of which approach/wavelength range is best for each diameter/length combination, and which ones result in less than ten percent error, can be seen in Appendix B.3.

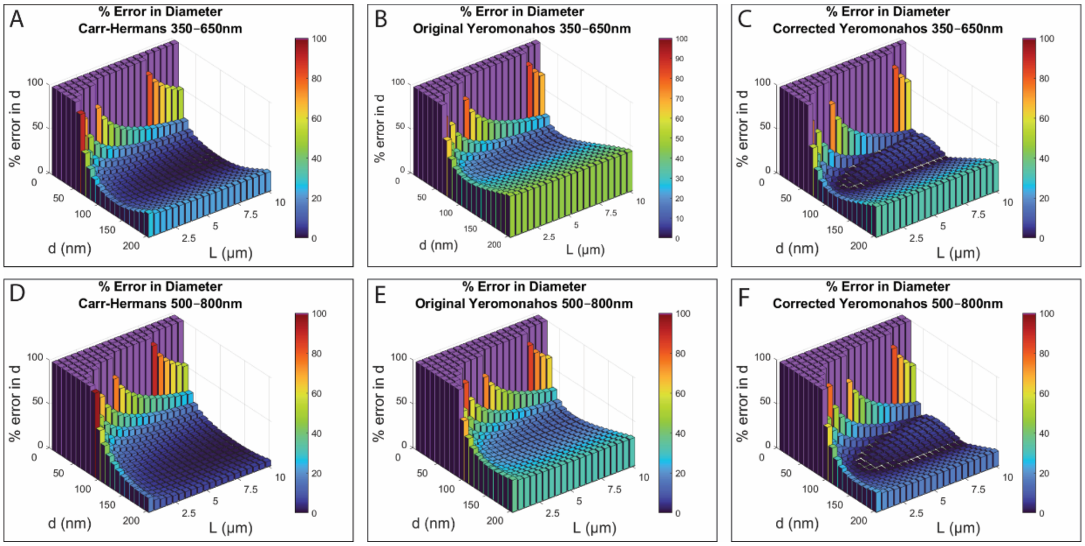

Fig. 5: Percent error between the diameter obtained from fitting the three approaches to theoretical turbidity values created using full light scattering theory, and the value used to create the initial dataset for lengths of 0.5-10 μm and diameters of 10-200 nm for wavelength ranges of 350-650 nm (A-C) and 500-800 nm (D-F). (c = 0.0001 g/cm^3, μ = 4.73 × 10^{12} Da/cm, dn/dc and n corrected for wavelength dependence for fibers in HBS buffer; the purple bars represent imaginary diameter values calculated from the fit and were assigned a value of 100% error for plotting purposes).

The percent error in the mass-length ratio obtained from the three turbidimetric approaches fit to full light scattering theory data compared to the value used to create the dataset are shown in Figure 6 for the two wavelength ranges. Note that the viewing angle is rotated 180° from what it was for the diameter error plots in Figure 5, and the percent error is the same for both the Original and Corrected Yeromonahos approaches, since the one changed term does not have an impact on the calculation of the mass-length ratio.

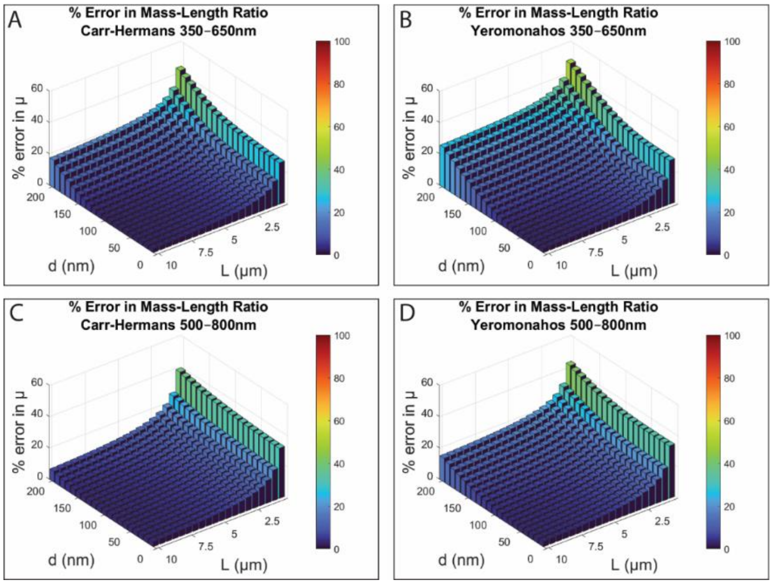

Fig. 6: Percent error between the mass-length ratio obtained from fitting the turbidimetric approaches to theoretical turbidity values created using full light scattering theory, and the value used to create the initial dataset for lengths of 0.5-10 μm and diameters of 10-200 nm for wavelength ranges of 350-650 nm (A-B) and 500-800 nm (C-D). (c = 0.0001 g/cm^3, μ = 4.73 × 10^{12} Da/cm, dn/dc and n corrected for wavelength dependence for fibers in HBS buffer).

Overall, there is much less error in the values of the mass-length ratio than with the diameter values. However, both wavelength ranges for all three of the approaches show an increased amount of error in the values of the mass-length ratio when the fibers are short (less than ~2 μm). All three of the approaches and both wavelength ranges appear to provide the most accurate values of the mass-length ratio when the fibers are thin (less than ~100 nm diameter) and long (5-10 μm length) and the Carr-Hermans approach from 500-800 nm also appears to provide accurate values when the fibers are thick (with diameters of 100-200 nm).

Some values of the mass-length ratio given by the approaches across this range of diameters and lengths are shown in Appendix B.3. The Carr-Hermans approach and the Yeromonahos approaches all result in underestimations of the mass-length ratio values compared to the values used to create the dataset when using full light scattering theory for all diameter/length combinations investigated.

A summary of which approach is best for each diameter/length combination, and which approaches result in a less than ten percent error can be seen in Appendix B.3. It shows that although the Carr-Hermans approach and the Yeromonahos approaches provide less than ten percent error in the mass-length ratio for both wavelength ranges for most diameter/length combinations, the Carr-Hermans approach using a wavelength range of 350-650 nm is the most similar to full light scattering theory when the fibers have diameters of less than ~140 nm, and the Carr-Hermans approach using a wavelength range of 500-800 nm is the most similar when the fibers have diameters of 140-200 nm.

We later determined based on our experimental analysis (see Chapter 3) that fibrin fiber diameters for physiological conditions can contain diameters up to approximately 258 nm, so the plots in this chapter do not quite cover the entire possible range (as they extend up to 200 nm). However, there is a simulated analysis of larger fiber diameters (up to 400 nm) provided in Appendix B.4. Furthermore, a description of the effects of changing fibrinogen concentration, diameter, length, and mass-length ratio can be seen in Appendix B.4.

Best Turbidimetric Approach

Based on the numerical simulations, we found that while the three different approaches worked reasonably well for some fiber diameters and lengths, they also produced unacceptably large errors or imaginary values for other fiber diameters and lengths. Thus, caution needs to be used when extracting fibrin fiber structural properties from turbidity versus wavelength data.

The percent of the diameter/length combinations in which each approach gives less than ten percent error for each of the wavelength ranges investigated is shown in Table 2. As can be seen, the Original Yeromonahos approach never provides less than ten percent error in the calculation of the diameter, and therefore appears to be the most unreliable approach.

As discussed earlier, the Original Yeromonahos approach always underestimates the diameter. However, by multiplying with the extra 2/3 factor in the denominator when solving for the diameter with the Corrected Yeromonahos approach, the calculated value is increased so that it is closer to the actual diameter values. This results in a smaller percentage error, as seen in Figure 5. As seen in Table 2, this allows for the diameter and mass-length ratio of approximately half of the investigated diameter/length combinations to be obtained with less than ten percent error. Although this extra 2/3 factor decreases the percent error in the calculations of the diameter when compared to the Original Yeromonahos approach, the factor was obtained erroneously, as described earlier. Therefore, there is no physical basis for using the "correction".

The Carr-Hermans approach using a wavelength range of 500-800 nm provides less than ten percent error in both the calculated diameter and the mass-length ratio for the most diameter/length combinations investigated, and therefore appears to be the most reliable of the turbidimetric fitting approaches when compared to full light scattering theory. However, as will be described in Chapter 3, this was not the case experimentally.

% of Investigated Diameter/Length Combinations with Less Than 10% Error		
Approach	**Diameter**	**Mass-Length Ratio**
Carr-Hermans 350-650 nm	49.75%	63%
Carr-Hermans 500-800 nm	55.75%	74.5%
Original Yeromonahos 350-650 nm	0%	46%
Original Yeromonahos 500-800 nm	0%	53.75%
Corrected Yeromonahos 350-650 nm	42.25%	46%
Corrected Yeromonahos 500-800 nm	51.25%	53.75%

Table 2: Percent of investigated diameter/length combinations in which each approach and wavelength range provided less than ten percent error in the calculations of the diameter and mass-length ratio.

Conclusion

There is an interest in determining the structural parameters of fibrin fibers because these parameters provide fundamental information regarding fibrin clot formation, and they have been correlated to diseases. Light scattering theory provides a connection between microscopic clot parameters (namely fiber diameter and mass-length ratio), and turbidity, which can be measured easily. However, extraction of the fiber diameter and mass-length ratio from turbidity data requires approximations to light scattering theory so that the scattering equations can be fit to turbidity versus wavelength data. We performed a computational evaluation of the validity of the three most commonly used approximations for physiologically relevant fiber lengths and diameters: the Carr-Hermans, the Original Yeromonahos, and the Corrected Yeromonahos approach, by applying them to turbidity versus wavelength datasets that were created from full light scattering theory.

The first important takeaway from the results is that it is necessary to account for the wavelength dependence of n and dn/dc, rather than using constant values. No matter which wavelength range is used, using a constant value for these factors considerably increases the percent error in the diameter and mass-length ratio calculations.

The results of the numerical simulations show that the utility of all three approaches is limited to certain values of fiber length, diameter, and wavelengths used for the turbidimetry measurements. As shown in Table 2, only the Carr-Hermans approach using a wavelength range of 500-800 nm and the Corrected Yeromonahos approach using a wavelength range of 500-800 nm provide less than ten percent error for over half of the diameter/length combinations investigated, with the Carr-Hermans approach providing less than ten percent error for the most diameter/length combinations investigated. As seen in Figure B.3 of Appendix B, the Carr-

Hermans approach provides less than ten percent error in the calculated diameter for fibers with diameters of 80-200 nm, and the Corrected Yeromonahos approach provides less than ten percent error in the calculated diameter for fibers with diameters of ~60-120 nm, as long as the length is greater than 1 µm. For fibers with diameters of 40-50 nm, the Corrected Yeromonahos approach works best in the 350-650 nm wavelength range. Below 40 nm, all three approaches fail, as they give imaginary values for the diameter.

For the mass-length ratio, the Yeromonahos approaches provide less than ten percent error for fibers with lengths of 3-10 µm and diameters of ~10-140 nm, and the Carr-Hermans approach provides less than ten percent error for fibers with lengths of 3-10 µm and diameters of ~10-200 nm. However, the Carr-Hermans approach always provides the least error in the mass-length ratio, with the Carr-Hermans approach using a wavelength range of 350-650 nm being best for fibers with diameters of less than ~140 nm, and the Carr-Hermans approach using a wavelength range of 500-800 nm being best for fibers with diameters of 140-200 nm. This can be seen in Figure B.4 of Appendix B.

Although the Corrected Yeromonahos approach does provide the most accurate results in calculating the diameter for some fiber diameter/length combinations, the Carr-Hermans approach is more often the most accurate, with less than ten percent error for most diameter/length combinations investigated (69% of all the diameter/length combinations investigated). Even when the Corrected Yeromonahos approach is better at calculating the diameter than the Carr-Hermans approach, it is only by a small difference in the percent error, with the largest difference being 13.37% error, and the average difference being 4.21% error. There is also no physical basis for the “correction” to the Yeromonahos approach, as described earlier. Furthermore, the Carr-Hermans approach always provides the most accurate results in calculating the mass-length ratio. Therefore, according to this theoretical analysis, the Carr-Hermans equation, especially when using the 500-800 nm wavelength range, despite its flaws, provides the most accurate results under many situations.

To summarize, based on comparison with full light scattering theory, the commonly utilized turbidimetric approaches are, for the most part, able to provide accurate values of diameter, as long as the fibers have a length of 1-10 µm and a diameter of 50-200 nm, and the mass-length ratio can be determined with less than ten percent error if the fibers have lengths of 3-10 µm and diameters of 10-200 nm. However, it is unclear whether turbidimetry analysis is able to provide accurate estimates at diameters that are far above 200 nm, as both full light scattering theory and the fitting approaches assume that the fibers are thin when compared to the wavelength values used for measurement.

Because full light scattering theory itself contains some limitations due to assumptions about the fiber and clot behavior, as described in more detail in Chapter 5, it is necessary to compare these results with those obtained experimentally. We have provided an experimental analysis of the turbidimetric fitting approaches in the next chapter (Chapter 3) and compare the theoretical results from this chapter to those obtained experimentally in Chapter 4.

CHAPTER 3: EXPERIMENTAL ANALYSIS OF TURBIDIMETRIC APPROACHES

Introduction

While these different turbidimetric approaches (Carr-Hermans, Original Yeromonahos, Corrected Yeromonahos, and Ferri) are each commonly utilized within the fibrinogen community, and the Original Yeromonahos approach is even patented for use in predicting and treating bleeding disorders clinically [35], there has not been a careful and comprehensive experimental comparison between the different turbidimetric approaches over varying clot conditions, nor a comparison with other experimental methods. Herein, we provide the first comparison of turbidimetry-based diameters from these four methods across a range of physiologically relevant fibrinogen and thrombin concentrations. Furthermore, we provide the first direct comparison of experimental fiber diameters obtained from turbidimetry, electron microscopy, and super-resolution microscopy.

Terminology

In a typical turbidity assay, a spectrophotometer is used to obtain the ratio of the light intensity transmitted through a sample and the incident light intensity, as shown in Figure 7, and typically reports a value of either absorption or optical density, which must then be converted by the user to turbidity. However, while the spectrophotometer often reports an absorbance value, turbidity assumes that the only interaction with the light is scattering by the particulates. Therefore, it is important to understand how to convert data from common optical instruments to turbidity.

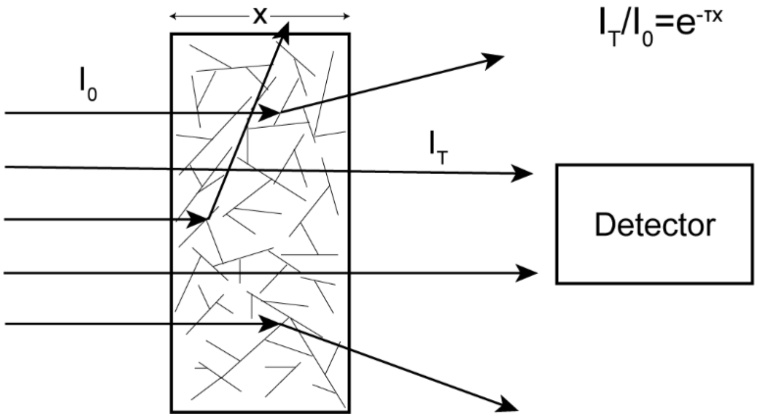

Fig. 7: The incoming light enters the solution and is scattered by the fibers. The transmitted light is collected by a detector. A ratio of the transmitted light to incoming light can be used to determine the turbidity.

Attenuance, a, is defined as the reduction in transmitted light through a sample due to absorption, scattering, or a combination of the two [36], and is given by:

$$a = -\log T = -\log\left(\frac{I_T}{I_0}\right) \qquad [42]$$

where *T* is the transmittance, defined as the ratio of transmitted light intensity, I_T, and incident light intensity, I_0. In the case of attenuation due to either absorption or scattering, the transmitted light intensity decreases exponentially with the thickness of the material through which the light passes [16]:

$$\frac{I_T}{I_0} = 10^{-\alpha_c x} \qquad [43]$$

$$\frac{I_T}{I_0} = e^{-\tau x} \qquad [44]$$

where Equation 43 is for the case where all loss of light intensity is due to absorption and Equation 44 is for the case where all loss of light intensity is due to scattering. α_c is the absorption coefficient (in units of cm^{-1}), τ is the turbidity (in units of cm^{-1}), and *x* is the pathlength, or sample thickness (in units of cm).

The absorption coefficient, α_c, is then related to absorbance, *A*, by [36]:

$$\alpha_c = A/x \qquad [45]$$

where the absorbance is defined as:

$$A = -\log\left(\frac{I_T}{I_0}\right) \qquad [46]$$

which is the same as the definition of the attenuance in Equation 42, except that the definition of absorbance assumes that the only loss of light intensity is due to absorption, and not due to scattering, while for the attenuance, the loss of light intensity could be from either (or both).

The output quantity in spectrophotometry measurements is often given as absorbance, which assumes that all loss of light intensity is due to absorption. However, if both absorption and scattering are taking place, this quantity is actually the attenuance, and if scattering is the only interaction taking place, the quantity should be expressed in terms of turbidity. Thus, when studying turbidity using a spectrophotometer, it is often necessary to convert "absorption" readings into turbidity by setting Equation 43 equal to Equation 44, and putting the absorption coefficient in terms of absorbance:

$$e^{-\tau x} = 10^{-\left(\frac{A}{x}\right)x} = 10^{-A}. \qquad [47]$$

Taking the natural log of both sides and solving for turbidity provides the relationship between turbidity, τ, and the "absorbance" value, *A*, from a typical spectrophotometer:

$$\tau = \frac{A}{x}\ln(10). \qquad [48]$$

Several papers refer to turbidity in terms of optical density, *OD* [13,19,20], and so it is also necessary to understand how optical density relates to absorbance and turbidity. However, this is more complicated by the fact that the definition of optical density is inconsistent within the literature. Thus, the use of this optical density term is discouraged [36]. The most widely used definition of optical density in the literature is [19,29]:

$$OD = -\log\left(\frac{I_T}{I_0}\right) \quad [49]$$

which makes optical density a unitless value with the same definition as absorbance, or attenuance if there is both scattering and absorption. This would mean that optical density and turbidity are related by:

$$\tau = \frac{OD}{x}\ln(10). \quad [50]$$

However, in the original Yeromonahos paper [20], optical density was defined as:

$$OD = -\frac{1}{x}\log\left(\frac{I_T}{I_0}\right) \quad [51]$$

which gives optical density units of cm^{-1}. This led the authors to the incorrect relation that:

$$\tau = 1 - e^{-OD\ln(10)}. \quad [52]$$

While this definition of turbidity was changed in a subsequent letter to the editor [21] to $\tau = OD\ln(10)$, the incorrect definition (Equation 52) has been repeated in more recent papers [11,28].

The lack of the pathlength factor in the updated Yeromonahos definition of turbidity has caused confusion in and of itself, as it has resulted in some researchers inserting the pathlength into the equation incorrectly [11,28]. While the definition of turbidity as $\tau = OD\ln(10)$ using optical density with units of cm^{-1} makes sense when using a pathlength of 1 cm, such as with a standard 1 cm wide cuvette, it may result in errors when using a pathlength other than 1 cm (such as in a 96-well plate). In those cases, it is necessary to calculate the pathlength. This can be performed by loading reference wells with the same volume of water as the liquid volume in the sample wells and taking absorbance measurements at ~975 nm (the absorption peak of water) and 900 nm (a reference wavelength), and then using the equation:

$$x = \frac{A_{(975nm)} - A_{(900nm)}}{K-factor}. \quad [53]$$

where the K-factor is a measure of the absorbance of water at the absorption peak minus the absorbance of water at the reference wavelength for a pathlength of 1 cm [37]. The pathlength can also be determined with a measurement of the height of the sample within the well, although this is difficult to obtain accurately, due to the meniscus of the sample surface.

Materials and Methods

Clotting Reagents:

To create clots, peak 1 fibrinogen, FXIIIa, and human alpha thrombin, all bought from Enzyme Research Labs, were combined in HBS buffer (150 mM sodium chloride, 20 mM HEPES, pH 7.4) with 5 mM calcium chloride. A western blot showing the crosslinking by the FXIIIa can be seen in Appendix C.1.

Clots were made with fibrinogen concentrations of 0.5, 1, 3, and 5 mg/mL and thrombin concentrations of 0.1, 1, and 5 NIH-U/mL (often shorted to U/mL, where U are the standard units determined by the National Institutes of Health for describing thrombin activity), with all samples containing 25 Loewy-U/mL FXIIIa (often shortened to L-U/mL, and describing the amount of enzyme required to form an insoluble clot under certain conditions). The fibrinogen concentrations were chosen to match the range of normal and diseased physiological conditions. Normal levels of fibrinogen are 2-4 mg/mL, hypofibrinogenemia is 0.2-0.8 mg/mL [38], and hyperfibrinogenemia is greater than 4 mg/mL [39]. The lowest physiological concentration of thrombin is 0.1 U/mL [40] so that was chosen as our lowest value, and 1 and 5 U/mL were also chosen, as those have been shown to produce drastically altered fiber structure [32]. FXIII circulates at a concentration of 14-28 μg/mL in plasma [41], which corresponds to approximately

42-84 L-U/mL. The normal activity of FXIII can be as low as 47% [42], thus leading us to choose 25 L-U/mL of FXIIIa for our samples.

Scanning Electron Microscopy (SEM):

To create the SEM samples, 5 holes were cut into the lid of a 600 µL microcentrifuge tube using an 18-gauge needle and the flat part of the lid was covered with parafilm. 50 µL fibrinogen solution, containing the peak 1 and FXIIIa in HBS buffer was loaded into the lid, and topped with 50 µL solution containing thrombin in HBS buffer with 10 mM calcium chloride. The solution was then pipetted up and down once to promote mixing of the thrombin and fibrinogen solutions. The lid was placed into a Petri dish containing a damp Kimwipe and the dish was sealed with parafilm along the outside to create a humidified chamber and incubated at 37°C for one hour. After that hour, the microcentrifuge lid containing the clot was taken out of the incubator and the parafilm was removed. The lid was then placed in a container of HBS buffer such that the clot was submerged below the surface and the flat side of the lid was floating at the top and stirred for twenty minutes. This was repeated two more times in fresh HBS solution. The clot was then submerged in the same manner in an aqueous 2% glutaraldehyde solution and left overnight.

The following day, the clot was again washed three times for twenty minutes each time in HBS solution in the same way. The clot was then placed into solutions of 30%, 50%, 70%, 90%, 100%, 100%, and 100% ethanol, sequentially, for 15 minutes each. It was then placed into a solution of 50% ethanol/50% hexamethyldisilazane for 10 minutes, then in 100% hexamethyldisilazane twice, for 10 minutes each time. The hexamethyldisilazane was then mostly removed, leaving just what was left on top of the clot in the lid, and the clot was left overnight to dry.

The following morning, the dried clot was removed from the microcentrifuge lid and mounted onto a stub topped with double-sided carbon tape. Small droplets of silver conducting paint were then placed at two ends of the mounted clot. Once the paint dried, the sample was sputter coated using a Denton Vacuum Desk V sputter coater for 40 seconds at 30 mA and imaged using a Zeiss EVO 10 scanning electron microscope at 21.96 kx magnification. A diagram outlining the methods for preparing a fibrin clot for SEM imaging are shown in Figure C.2 of Appendix C.2. The methods were adapted from those previously published [11] in collaboration with the Guthold lab.

Fiber diameter values were obtained from the acquired SEM images using the line segment measuring tool in ImageJ (http://rsbweb.nih.gov/ij/). This process was repeated in the same manner for clots of each fibrinogen/thrombin concentration analyzed, with two samples imaged at each investigated concentration. There were on average six images analyzed per concentration, with an average of 185 fiber measurements per concentration.

Stochastic Optical Reconstruction Microscopy (STORM):

To prepare the STORM samples, 5 μL fibrinogen solution (containing the wild-type fibrinogen, AlexaFluor-647-labeled fibrinogen, and FXIIIa) was spread out onto a 22 x 22 mm cover glass and combined with 5 μL thrombin solution. The samples were placed into a closed Petri dish with a damp Kimwipe to create a humidified container, and were allowed to polymerize for one hour at 37 °C. Following polymerization, the samples were topped with 5 μL HBS buffer and 5 μL Vectashield mounting medium to decrease photobleaching of the fluorophores. The cover glass containing the sample was then carefully placed onto a microscope slide, with the fibrin clot between the two, and sealed around the edges using fingernail polish. A representative image of a fibrin clot prepared for STORM imaging is provided in Figure C.3 of Appendix C.2.

STORM images were acquired using Nikon NIS-Elements AR software version 5.11.00 and an Apo TIRF 100x objective (1.49 NA) on a Nikon Eclipse Ti2 inverted microscope, equipped with 405 and 640 nm lasers. Imaging was performed in a slice where fibers were primarily oriented in the imaging plane to ensure accurate fiber diameter measurements. Images were acquired at an image size of 256 × 256 pixels for 20,000 frames using a ProEM HS EMCCD camera (Princeton Instruments), 16-bit with no binning. EM gain was set to 20 MHz with an EM gain multiplier of 300 and a conversion gain multiplier of 1. The 640 nm laser power was set to 100%, and the “Adjusted Laser Powers” setting provided by the NIS-Elements software was used to control the photoswitching of the AlexaFluor-647 fluorophores through activation using the 405 nm laser and excitation using the 640 nm laser.

STORM images were reconstructed from the raw .nd2 files using the NIS-Elements software with the following settings: “Auto Fit ROI”, minimum height 1000, maximum height 65,535; CCD Baseline was set to 100, minimum width 200 nm, maximum width 700 nm, initial fit width 300 nm, maximum axial ratio 2.5, and a maximum displacement of 1 pixel. At the end of the run, the files were processed into .bin files, which contained the molecule count information with the coordinates and the intensity of each blinking event. Drift correction was performed using the automatic drift correction option in the NIS-Elements software. After processing, the final STORM images were displayed as a collection of Gaussian spots representing each blinking event. A 30 × 30 pixel region of interest was captured for each fiber within the image, and saved as a .nd2 file for further analysis. Subsequent analysis of the processed .nd2 files was performed with ImageJ (http://rsbweb.nih.gov/ij/) software using the line segment measuring tool to obtain the fiber diameter.

A minimum of two samples were imaged for each investigated fibrinogen/thrombin concentration. The concentration of AlexaFluor-647-labeled fibrinogen for each sample was chosen so that the edges of the fibers could be clearly distinguished in the reconstructed STORM images. The fraction of AlexaFluor-647-labeled fibrinogen to wild type fibrinogen for each sample is noted in Appendix C.2, with a discussion on the effects that changing AlexaFluor concentrations would play on the obtained fiber diameters in Appendix C.3.

Confocal Imaging:

The confocal images were prepared in the same manner as the STORM samples, except that following polymerization, they were only topped with 5 μL HBS buffer, not with Vectashield mounting medium. AlexaFluor-647-labeled fibrinogen was added at 1/65 the concentration of wild type fibrinogen for all samples. Two samples were imaged for each investigated fibrinogen/thrombin concentration.

Confocal images were acquired on each sample using a Zeiss LSM800 laser scanning microscope, using a 63x oil immersion objective. Z-stack images were taken throughout the sample height with equivalent settings used for all samples (slice thickness of 0.3 μm, pin hole size of 55.84 μm, frame size of 1024x1024 pixels, pixel size of 0.1 μm, frame rate of 17.87 seconds, and pixel time of 8.24 μs, at 8 bits per pixel).

Confocal images were used to determine fiber length, mass fractal dimension, and pore size. In order to determine the fiber length, manual measurements were taken on the obtained 3D confocal images using the program Imaris. To determine the mass fractal dimension, the 2D slices making up the 3-dimensional stack were made binary using ImageJ, with the default method and background settings, which set an automatic threshold level based on analysis of the histogram of the image, converting the object to pixel values of 255 and 0, then the fractal box count tool in ImageJ was used to obtain the fractal dimension, using box sizes of 2, 3, 4, 6, 8, 12, 16, 32, and 64 pixels. This tool works by covering the image with a sequence of grids of varying box sizes and plotting the log of the number of boxes containing fibers versus the log of the box size, with the slope of the plot being equal to negative the mass fractal dimension [43]. The pore size was also obtained on the binary images creating the 3-dimensional stack, using the MATLAB code provided by Münster and Fabry [44] which is based on the method proposed by Molteni et al. [45]. This code works by segmenting the image into fiber pixels of value 1 and fluid pixels of value 0, then creating a Euclidean distance map (EDM) that assigns each pixel of the fluid phase a Euclidean distance to the nearest fiber pixel. The EDM value determines the largest radius a circle centered at each pixel can have without overlapping any fibers. Next, the coordinates of all local maxima are determined (a pixel whose eight neighbors all have similar values). The local maxima of the EDM define the locations of the center points of all possible 2D "bubbles". It was shown by Molteni et al. [45] that the diameter values obtained for these 2D "bubbles" are good representations of the 3D pore sizes as long as the pore sizes are isotropic. Once the radii of the pores were provided by the program, the values below a manually measured threshold were removed, as described in more detail in Appendix C.4, and the pixel radii values were converted to diameters in μm. In order to confirm the pore size values obtained, ten manual measurements were performed for each sample using Imaris by placing a sphere in the center of selected pores, sized to fill the pore, and recording the diameter of the sphere. The manual values were compared to those obtained using the MATLAB program and can be seen in Appendix C.4.

Turbidimetry:

"Absorbance" measurements were taken on clots containing each investigated fibrinogen/thrombin concentration in both a cuvette, as well as in a 96 well plate, with each performed in triplicate.

For the experiments performed in a cuvette, a Thermo Scientific Nanodrop 2000c spectrophotometer was used to take the measurements, and the solutions were loaded into disposable micro-cuvettes with a pathlength of 1 cm. This allowed for small volumes to be used without the need for pathlength corrections.

First, measurements were taken on a 100 μL background solution containing the desired concentrations of thrombin and FXIIIa, but with no fibrinogen. Then a cuvette containing 50 μL fibrinogen solution (with the fibrinogen and FXIIIa) was placed into the spectrophotometer and the solution was topped with 50 μL thrombin solution. Immediately following the addition of thrombin to the fibrinogen in the sample solution, "absorbance" measurements were taken at 405 nm every 15 seconds for one hour at 37°C while the clots polymerized. After the one hour of polymerization, measurements were taken every 10 nm over a range of 350-800 nm. The equipment automatically subtracted the "blank" measurements from the sample measurements, removing any background from the sample's absorbance values.

For the measurements performed in a 96 well plate, three wells were prepared for each sample concentration being analyzed, three wells with background solution containing the same concentrations of buffer, thrombin, and FXIIIa as used in the sample solutions, but with no fibrinogen, and three wells with deionized water, all at a final volume of 150 μL per well. For the sample wells, 75 μL fibrinogen solution containing the fibrinogen and FXIIIa in HBS buffer was loaded into the bottom of a 96 well plate. The fibrinogen solution was then topped with 75 μL thrombin solution containing human alpha thrombin in HBS buffer with 10 mM calcium chloride.

Immediately after the addition of thrombin, the sample was shaken by the BioTek Synergy HT plate reader for 5 seconds, then "absorbance" measurements were taken every 15 seconds for one hour at a wavelength of 405 nm and a temperature of 37°C to capture the polymerization process. After that hour, "absorbance" measurements were taken on the same wells every 10 nm from 350-800 nm, as well as at a wavelength of 900 nm and 977 nm, to allow for pathlength measurements. The measurements taken in the 96 well plate were also repeated using a cover, then a double-layered cover, with smaller hole sizes in order to determine the effects of multiple scattering.

The triplicate values for each sample were averaged. In some cases, one of the triplicate values was excluded due to 80-100% of their datapoints falling outside of one standard deviation of the other two samples. This is likely due to a bubble forming during the process of adding the activation solution, leading to a change in scattering that is from the change in medium rather than from the formation or thickening of fibers. The average "absorbance" value from the background wells were then subtracted from the average value for each sample of the corresponding thrombin concentrations for each datapoint. The pathlength (in cm) was calculated by averaging the "absorbance" values for the wells with water and subtracting the value at 900 nm from the value at 977 nm, then dividing by 0.18 (the K-factor).

The "absorbance" values for each of the samples obtained from either the cuvette or from the plate reader were converted to turbidity using Equation 48 and then plotted into the appropriate formats and fit with each of the different turbidimetric approaches to extract the fiber diameter.

This was done for a wavelength range of 350-650 nm, 500-800 nm, and 350-800 nm, both using constant values of n and dn/dc, as well as accounting for their wavelength dependence. When accounting for the wavelength dependence of n and dn/dc, the equations $n(\lambda) = 1.3247 + \frac{3093.9}{\lambda^2}$ and $\frac{dn}{dc}(\lambda) = 0.1853 + \frac{1689.9}{\lambda^2}$ were used. For the constant values, the spectral averages were used, which were $< n >$ = 1.3383 and $< \frac{dn}{dc} >$ = 0.192728 for a wavelength range of 350-650 nm, $< n >$ = 1.33243 and $< \frac{dn}{dc} >$ = 0.189525 for 500-800 nm, and $< n >$ = 1.33575 and $< \frac{dn}{dc} >$ = 0.191335 for 350-800 nm.

A diagram outlining the methods for obtaining turbidimetry measurements on a fibrin clot are shown in Figure C.9 of Appendix C.5.

Results and Discussion

SEM and Super Resolution Imaging

Although SEM imaging is the standard used for determining fibrin fiber diameter, it requires drying and fixation of the samples, which can lead to morphological changes. It is well known that the sample preparation can alter the final imaged sample; however, the full effects are largely undetermined due to the limited number of alternative methods for determining fiber diameter. However, with the recent invention of super-resolution fluorescent microscopy, it is now possible to determine the fiber diameter of fibrin fibers in solution, without the need for drying.

For typical visible light microscopes, the microscope is governed by Abbe's diffraction limit, meaning the lateral resolution is ~$\lambda/2NA$, where λ is the wavelength of light used for imaging, and NA is the numerical aperture of the objective. Assuming that a wavelength of 647 nm is used for imaging and the numerical aperture is 1.4, the resolution limit would be ~231 nm, with anything below that appearing as a diffraction-limited blur [46]. This makes reliable determination of fibrin fiber diameter impossible, as they range on average from 44-210 nm for conditions similar to those in blood, according to SEM imaging [32,47]. However, STORM microscopy is able to obtain over 10x improved resolution through the use of optically switchable fluorophores that can be switched between fluorescent and nonfluorescent states by exposure to light [48]. By using optically switchable fluorophores, only a small number of fluorophores are excited at a time, allowing for a high degree of accuracy in the localization of individual fluorophores with Gaussian fitting [49]. This allows for an imaging resolution of approximately 20 nm [48], allowing for accurate measurement of fibrin fiber diameters.

While a few groups have used super-resolution imaging to analyze fibrin fibers [50-53], an in-depth comparison between diameters obtained using SEM and using super-resolution imaging has yet to be performed. Here, we provide a comparison of the diameters obtained using SEM and STORM imaging across a range of physiological fibrinogen and thrombin concentrations.

Side-by-side SEM and STORM images for fibrin fibers created with the same fibrinogen and thrombin concentrations at similar magnification can be seen in Figure 8. Representative SEM and STORM images for the full range of investigated concentrations can be seen in

Appendix C.2. Plots showing the average diameters obtained using the two methods for each clot condition are shown in Figure 9, with the actual diameter values provided in Appendix C.2.

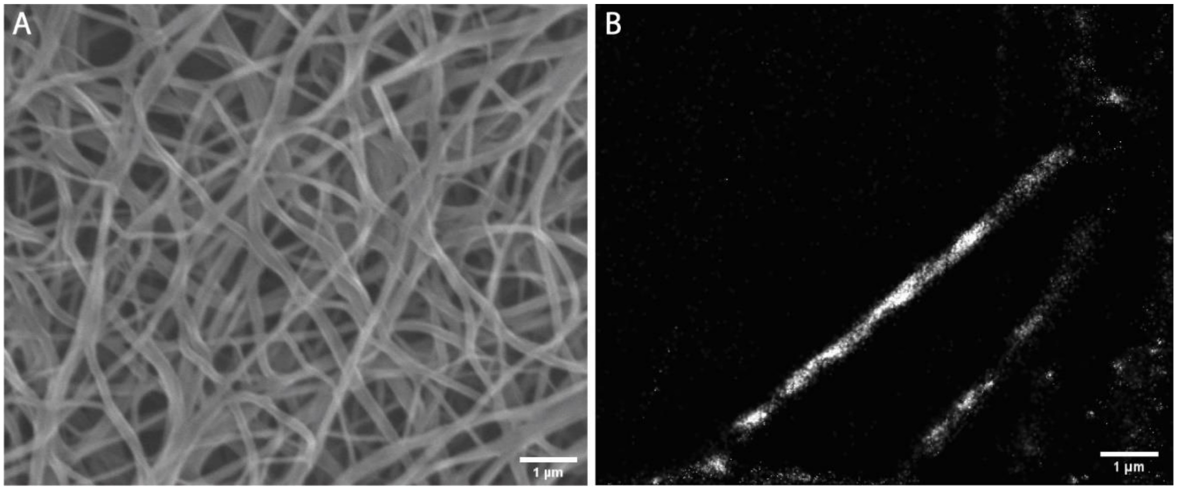

Fig. 8: Representative A) SEM and B) STORM images of clots made with 0.5 mg/mL fibrinogen, 0.1 U/mL thrombin, and 25 L-U/mL FXIIIa (scale bars 1 µm).

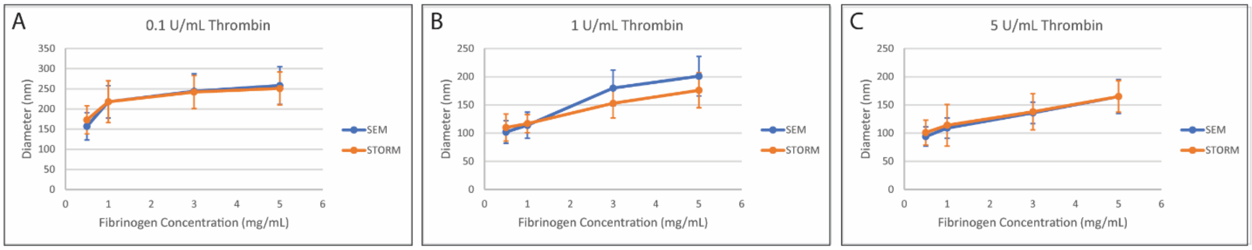

Fig. 9: SEM vs. STORM diameters for fibrinogen concentrations of 0.5, 1, 3, and 5 mg/mL, and thrombin concentrations of A) 0.1 U/mL, B) 1 U/mL, and C) 5 U/mL (error bars represent the standard deviation).

The diameter values obtained from SEM imaging and from STORM imaging were remarkably similar for most clot conditions, with the averages ± standard deviations overlapping for all clot conditions. Furthermore, they both show increased fiber diameter as the fibrinogen concentration is increased, and decreased diameter as the thrombin concentration is increased. This matches previously reported results [54,55]. The opposite trend in the effect of fibrinogen concentration was reported by Ryan et al. [32], who reported decreased fiber diameters with increasing fibrinogen concentrations. However, they reported very similar ranges of diameters for the three investigated concentrations, with only a 26 nm difference in the largest and smallest average diameters reported and considerable overlap between the sample averages when accounting for the standard deviation.

Since the diameter values obtained using SEM and STORM were so similar, we elected to use those from SEM imaging for comparison with those obtained from the turbidimetric approaches, since it is the more commonly utilized of the two methods.

Confocal Imaging

In addition to the turbidimetry measurements, the Ferri approach also requires pore size and mass fractal dimension measurements. The pore size is the size of the spaces between the fibers, and thus describes the density of the network, since the more densely packed the fibers, the smaller the pore sizes will be. The mass fractal dimension is a measure of the complexity of the network pattern. The pore size and mass fractal dimension were obtained using confocal images. Fiber length measurements were also obtained from the confocal images. Representative confocal images for each of the fibrinogen/thrombin concentrations can be seen in Figure 10. The obtained parameter values can be seen in Table 3.

Our results match those predicted based on previous works, showing that the pore size should decrease with increasing fibrinogen concentration [56], the mass fractal dimension should increase with increasing fibrinogen concentration and increase with increasing thrombin concentrations [57], and the fiber length should decrease with increasing thrombin concentration [32].

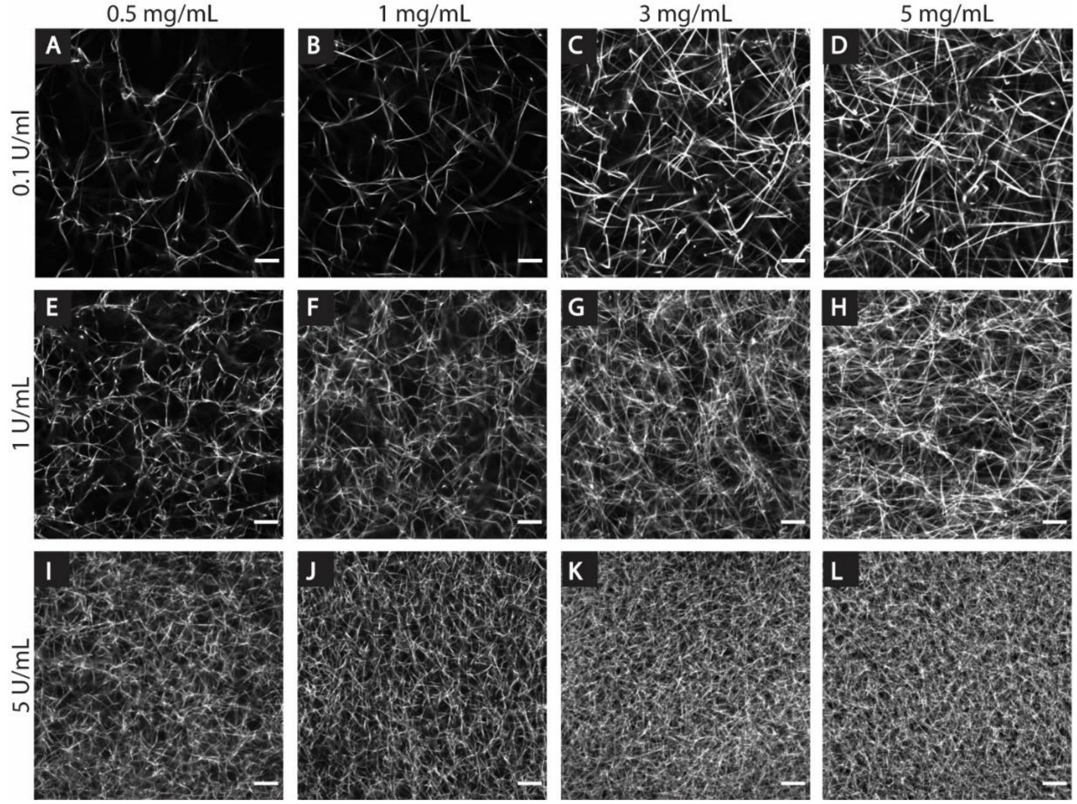

Fig. 10: Representative confocal images for each investigated fibrinogen and thrombin concentration (noted by column and row headings, respectively) imaged using a Zeiss LSM800 with a 63x objective (scale bars 10 µm; brightness/contrast auto adjusted for visualization purposes using ImageJ).

A

Fibrinogen Concentration (mg/mL)	**Pore Size (µm)**	**Fiber Length (µm)**	**Mass Fractal Dimension**
0.5	6.61 ± 2.13 (n=228)	9.26 ± 3.20 (n=104)	1.41 ± 0.03 (n=20)
1	5.47 ± 1.53 (n=323)	8.19 ± 2.86 (n=102)	1.43 ± 0.01 (n=18)
3	2.88 ± 0.54 (n=730)	6.86 ± 2.35 (n=101)	1.58 ± 0.01 (n=20)
5	2.52 ± 0.44 (n=1152)	6.22 ± 1.67 (n=101)	1.64 ± 0.01 (n=23)

B

Fibrinogen Concentration (mg/mL)	**Pore Size (µm)**	**Fiber Length (µm)**	**Mass Fractal Dimension**
0.5	2.82 ± 0.44 (n=488)	5.57 ± 1.49 (n=102)	1.65 ± 0.04 (n=25)
1	2.58 ± 0.54 (n=606)	5.13 ± 1.43 (n=102)	1.73 ± 0.01 (n=22)
3	1.99 ± 0.40 (n=1142)	3.97 ± 1.28 (n=100)	1.74 ± 0.02 (n=18)
5	1.72 ± 0.32 (n=2054)	3.10 ± 0.96 (n=102)	1.78 ± 0.004 (n=20)

C

Fibrinogen Concentration (mg/mL)	**Pore Size (µm)**	**Fiber Length (µm)**	**Mass Fractal Dimension**
0.5	1.63 ± 0.26 (n=1514)	2.61 ± 0.77 (n=101)	1.76 ± 0.04 (n=20)
1	1.37 ± 0.17 (n=2115)	2.20 ± 0.55 (n=102)	1.77 ± 0.02 (n=23)
3	1.17 ± 0.19 (n=3616)	1.85 ± 0.44 (n=101)	1.84 ± 0.009 (n=21)
5	0.96 ± 0.17 (n=5988)	1.45 ± 0.37 (n=102)	1.85 ± 0.008 (n=17)

Table 3: The pore size, fiber length, and mass fractal dimension for 0.5, 1, 3, and 5 mg/mL fibrinogen, with A) 0.1 U/mL thrombin, B) 1 U/mL thrombin, and C) 5 U/mL thrombin. (uncertainty = standard deviation; number of datapoints in parentheses).

Turbidimetry Measurements

Absorption vs. Scattering

Turbidimetry assumes that the only attenuation mechanism is scattering by the fibers, and that no absorption takes place. At first glance, this may seem to be a poor assumption, since tryptophan, tyrosine, and phenylalanine have an absorption peak at approximately 280 nm, and fibrinogen contains a significant number of these amino acids. However, it has been shown that the absorption of these residues falls to zero (or close to it) prior to a wavelength of 350 nm [22,58], which is the lowest wavelength value used in our analysis. We further tested this ourselves by performing absorbance measurements on a solution containing 0.4 mg/mL fibrinogen, with measurements taken every 25 nm from 200-800 nm, as seen in Figure 11. These results confirm that there is little to no absorbance in the wavelength range being investigated (350-800 nm). Thus, absorption plays little to no role in the loss of transmitted light, and so the assumption of most attenuation coming from scattering is reasonable.

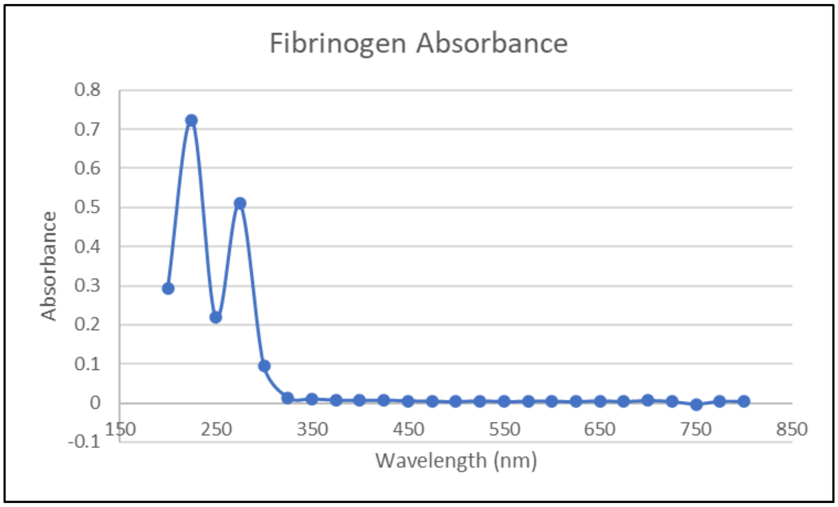

Fig. 11: Absorbance measurements on a solution containing 0.4 mg/mL fibrinogen in HBS buffer, showing that there is little to no absorbance by fibrinogen in the 350-800 nm wavelength range utilized in our experiments.

Effect of Fibrinogen Aggregates

It has been shown that stock supplies of fibrinogen, namely those provided by Enzyme Research Labs, contain a small amount of fibrinogen aggregates [31]. It has furthermore been shown that fibrin polymerization is altered in the presence of aggregates, resulting in thinner fibers [31,59].

In order to test the presence and effect of fibrinogen aggregates on our specific fibrinogen stock, we completed a turbidity assay and widefield fluorescent imaging of fibrin clots created using the stock fibrinogen (Enzyme Research Labs), fibrinogen from that same stock that we then purified using a size exclusion column, and fibrinogen that was run over the size exclusion column and then centrifugally concentrated. All experiments were done on samples made from 0.5 mg/mL peak 1 fibrinogen (Enzyme Research Labs), 0.1 U/mL human α-thrombin (Enzyme Research Labs) in HBS (150 mM NaCl, 20 mM HEPES, pH 7.4) containing 5 mM $CaCl_2$. We also completed dynamic light scattering (DLS) measurements of the three fibrinogen solutions at a concentration of 0.5 mg/mL in HBS buffer.

The results from the size exclusion purification can be seen in Figure 12, where the x-axis provides the number of the fraction collected and the y-axis provides a reading of the absorbance at 280 nm in milli-absorbance units (mAU). The greater the absorbance value, the greater the amount of fibrinogen present in that fraction, which can be calculated quantitatively using the Beer-Lambert Law. We collected fractions 14-19, as those appeared to contain fibrinogen based on the absorbance measurements, and tested the fibrinogen concentration in each of the fractions using a Thermo Scientific NanoDrop 2000c spectrophotometer. The measured concentrations are shown in Table 4. Sometimes the purification equipment skips a collection container in the process of dispensing the liquid, so that is likely the reasoning for the peak of the curve not aligning with the fractions that reported the highest fibrinogen concentrations. Since fractions 16 and 17 contained the largest concentrations of fibrinogen, a portion of those two samples were combined and the sample was concentrated using a centrifugal concentrator. The resulting concentration according to the NanoDrop was 7.35 mg/mL. The stock solution prior to purification was used as the stock sample, fraction 17 was used as the purified sample, and the combined and concentrated fractions 16 and 17 was used as the concentrated sample.

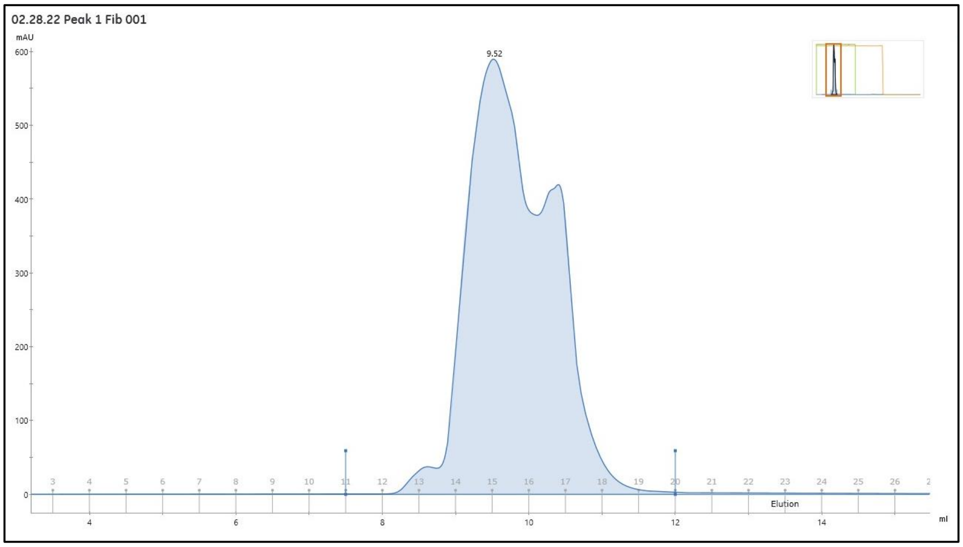

Fig. 12: Fibrinogen purification results using a size exclusion column.

Fraction	Fibrinogen Concentration (mg/mL)
14	0.03
15	0.20
16	1.53
17	1.85
18	1.40
19	0.38

Table 4: The fibrinogen concentration for each of the collected fractions from the size exclusion purification.

For the turbidity measurements, absorbance readings were taken using a BioTek Synergy HT plate reader at 350 nm, with readings taken every 15 seconds for an hour following the addition of thrombin to the fibrinogen. The absorbance values of background solution consisting of 0.1 U/mL thrombin in HBS with 5 mM $CaCl_2$ were subtracted from the absorbance readings of the sample. The results are shown in Figure 13. In addition to the solutions described above, we also tested a sample containing fibrinogen that had been run over the size exclusion column and then flash frozen using liquid nitrogen, stored at -80°C, and thawed again at 37°C to test the effect of freeze/thaw cycles.

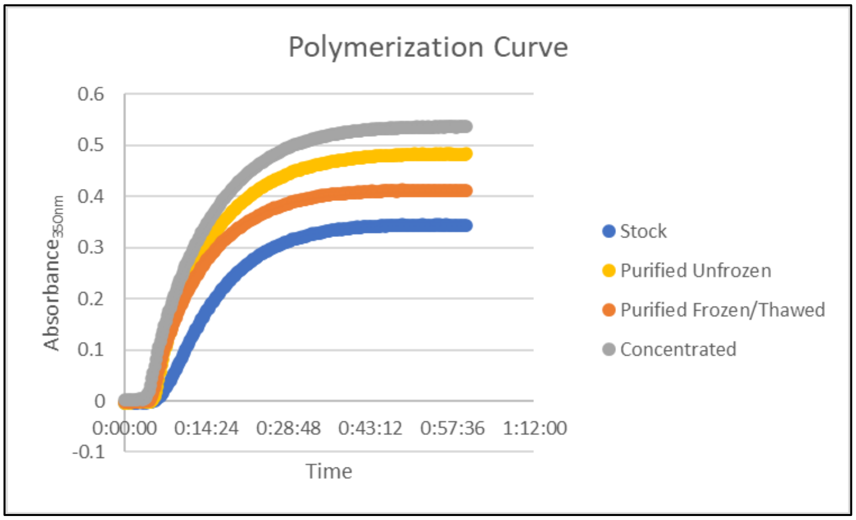

Fig. 13: Turbidity assay polymerization curves for clots created using the stock fibrinogen solution, unfrozen purified fibrinogen, frozen then thawed purified fibrinogen, and concentrated purified fibrinogen.

According to experiments done by Lihong Huang and Susan T. Lord [59], as well as by García et al. [31], the maximum absorbance should be lower for samples containing aggregates. Our measurements suggest similar results, as the stock solution is expected to contain the highest number of aggregates and has the lowest maximum absorbance value, while the purified solution has a much higher absorbance value, and that is slightly decreased for the purified sample that has gone through a freeze/thaw cycle, which likely introduces new aggregates. The purified sample that has been centrifugally concentrated has the highest maximum absorbance value. The reasoning for this is unclear, but could be due to some of the calcium in the buffer being lost during the concentration process. It has been shown that fiber diameter decreases and density increases with decreasing amounts of calcium [32]. Therefore, decreased calcium could lead to increased density, which could increase the maximum absorbance value. This idea is further supported by the widefield fluorescent images of the samples, as shown in Figure 14. The samples were prepared for fluorescent imaging by combining 5 μL fibrinogen solution at 1 mg/mL containing 0.015 mg/mL Alexa-647 labeled fibrinogen with 5 μL thrombin at 0.2 U/mL on a coverglass. This was allowed to polymerize for 1 hour at 37°C in a sealed Petri dish containing a damp Kim wipe to create a humidified container. After polymerization, the sample was topped with 5 μL HBS and 5 μL Vectashield to reduce photobleaching and the coverglass was placed onto a microscope slide and sealed around the edges so that the sample was secured between the coverglass and microscope slide. It was then imaged on a Nikon Eclipse Ti2 inverted microscope using a 640 nm laser and an Apo TIRF 100x objective (1.49 NA). As can be seen, the stock solution and purified solution show similar clot behavior, but the purified sample that has also been concentrated appears to be more dense, with thinner fibers. Although the concentrated sample clearly contains altered clot behavior, the concentration step would be necessary to obtain physiologically relevant concentrations from the purified fibrinogen.

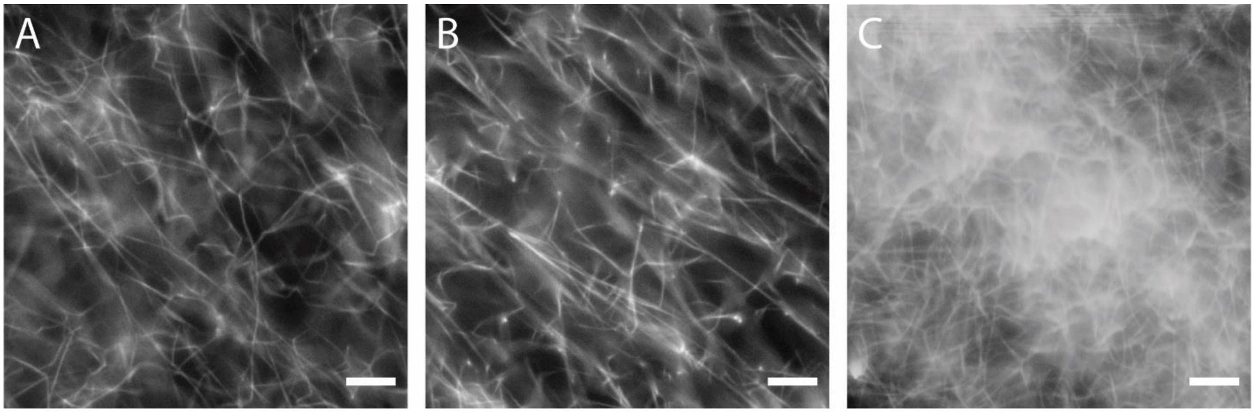

Fig. 14: 2D slice widefield fluorescent images of fibrin clots containing A) stock fibrinogen, B) purified fibrinogen, and C) concentrated purified fibrinogen (scale bar 10 μm).

Finally, to test the amount of aggregates in each of the solutions, DLS measurements were taken on each of the fibrinogen samples at a concentration of 0.5 mg/mL in HBS buffer using a Wyatt DynaPro NanoStar. The results can be seen in Table 5. Pure fibrinogen monomers have a hydrodynamic radius of ~10 nm [60]. As seen, the values we obtained for all three fibrinogen solutions are very close to this expected radius, with the purified fibrinogen having the lowest value, the concentrated purified fibrinogen being a little higher, and the stock fibrinogen being the highest. This further supports the idea that the stock fibrinogen contains aggregates that are removed during purification. Furthermore, the purified fibrinogen only showed one peak, while the stock fibrinogen and concentrated sample contained a second peak of higher radius, likely caused by aggregation, as shown in Figure 15.

	Hydrodynamic Radius (nm)
Stock Fibrinogen	11.6
Purified Fibrinogen	9.3
Purified/Concentrated Fibrinogen	10.5

Table 5: Hydrodynamic radius of stock fibrinogen, purified fibrinogen, and purified then concentrated fibrinogen solutions according to dynamic light scattering.

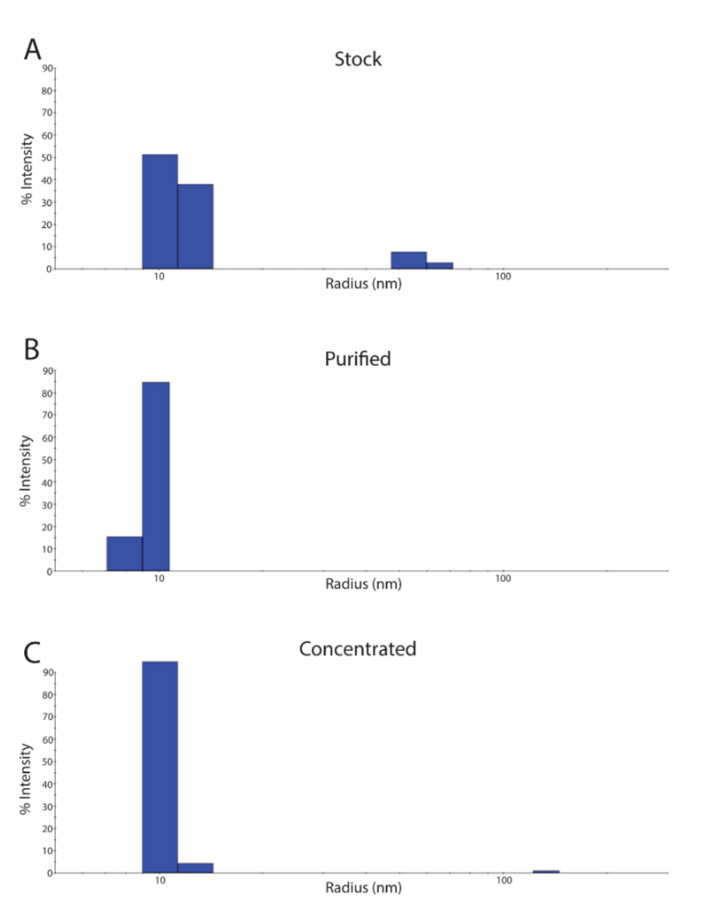

Fig. 15: Dynamic light scattering peaks for A) stock fibrinogen, B) purified fibrinogen, and C) concentrated fibrinogen solutions.

While our stock solution does appear to contain some aggregates, it has been shown that normal plasma contains fibrinogen aggregates, and that those with ischemic diseases and bleeding tendencies have elevated amounts of aggregates present in their plasma [59,61]. Since pathological conditions such as myocardial infarction [5], ischemic stroke [6], and venous thromboembolism [7] have been shown to contain gels and fibers with altered structural properties, in order to further understand these diseases and how they are linked to altered fibrin structure, it is necessary to understand how fibrin behaves with changing parameters under similar environmental conditions. Therefore, in order to make our results more clinically relevant, we elected not to purify the stock solutions in our experiments in order to study how fibrin structural properties change with changing fibrinogen and thrombin concentrations, while also containing fibrinogen aggregates. We furthermore used one stock solution for all experiments in order to ensure that the amount of aggregates was constant between experiments.

Turbidimetry Diameter Values

Due to limitations of the cuvette reader which are discussed in more detail in the subsequent cuvette vs. 96 well plate section, we used analysis of the experiments performed in a 96 well plate in order to analyze the accuracy of the different turbidimetric approaches. Plots showing the diameter values from SEM imaging and obtained using each of the four turbidimetric approaches for each investigated fibrinogen/thrombin concentration are shown in Figures 16-18 for a wavelength range of 350-650 nm, 500-800 nm, and 350-800 nm, respectively. The orange datapoints represent those in which the wavelength dependence of the refractive index (n) and specific refractive index increment (dn/dc) were accounted for and the gray datapoints represent those in which constant values of n and dn/dc were used. A color-coded plot showing the percent error between the diameter obtained using the turbidimetric approaches and those obtained using SEM are shown in Figure 19.

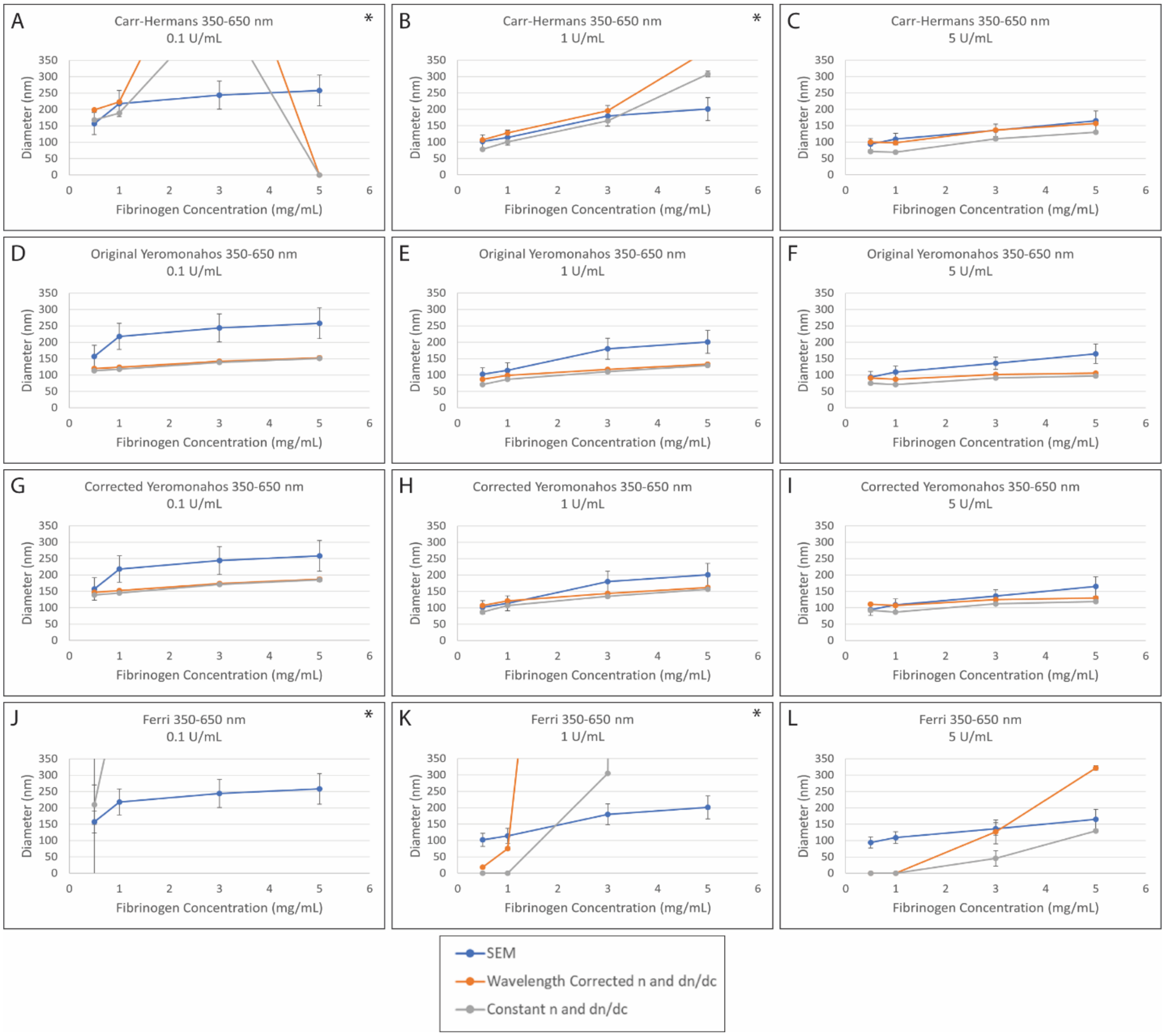

Fig. 16: Plots of diameters obtained using the different turbidimetric approaches (for wavelength corrected n and dn/dc and constant n and dn/dc) and those obtained using SEM for a wavelength range of 350-650 nm (plots with * in top right corner have some datapoints outside of the plot range; imaginary diameter values were plotted as a diameter of 0 nm).

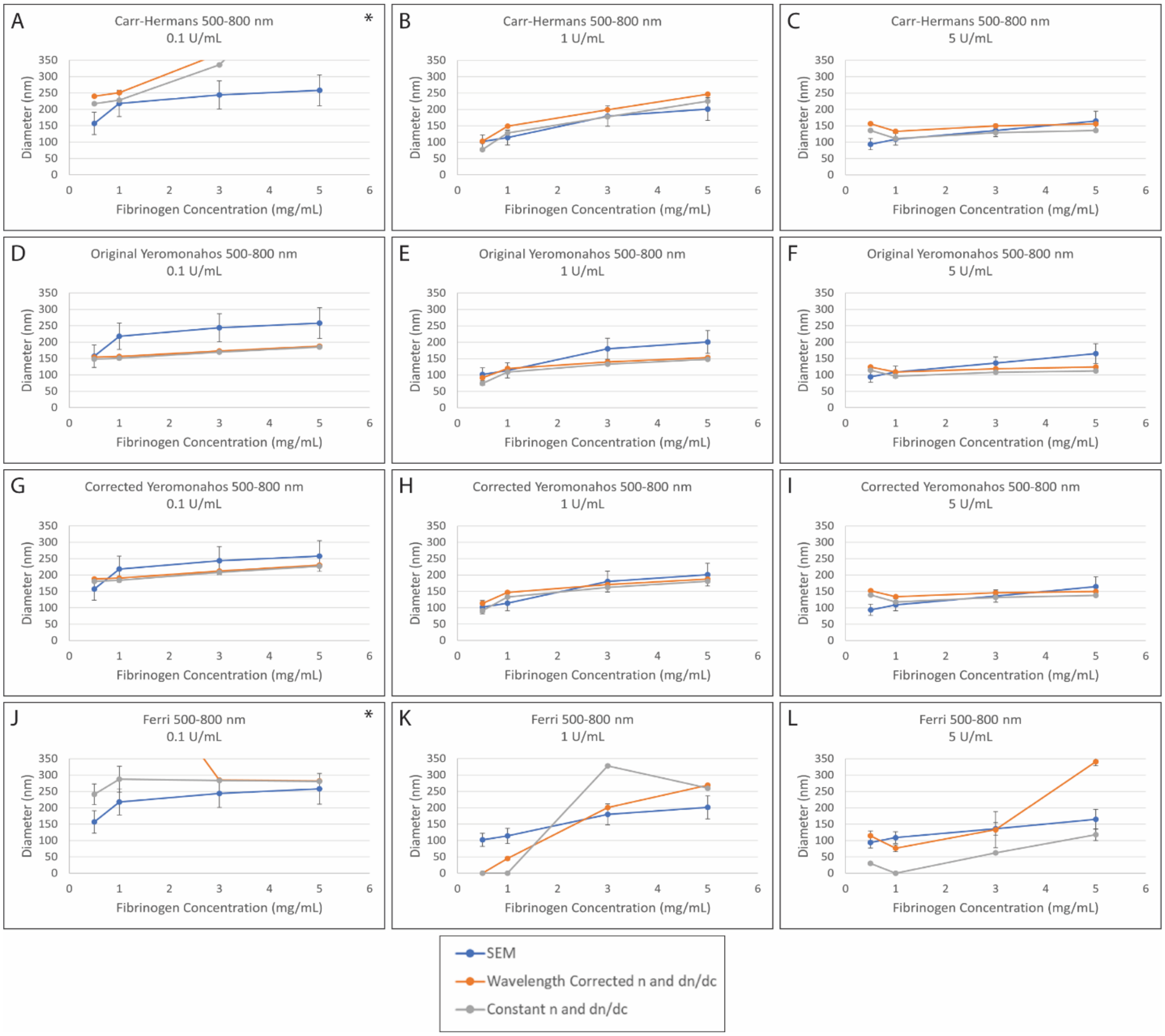

Fig. 17: Plots of diameters obtained using the different turbidimetric approaches (for wavelength corrected n and dn/dc and constant n and dn/dc) and those obtained using SEM for a wavelength range of 500-800 nm (plots with * in top right corner have some datapoints outside of the plot range; imaginary diameter values were plotted as a diameter of 0 nm).

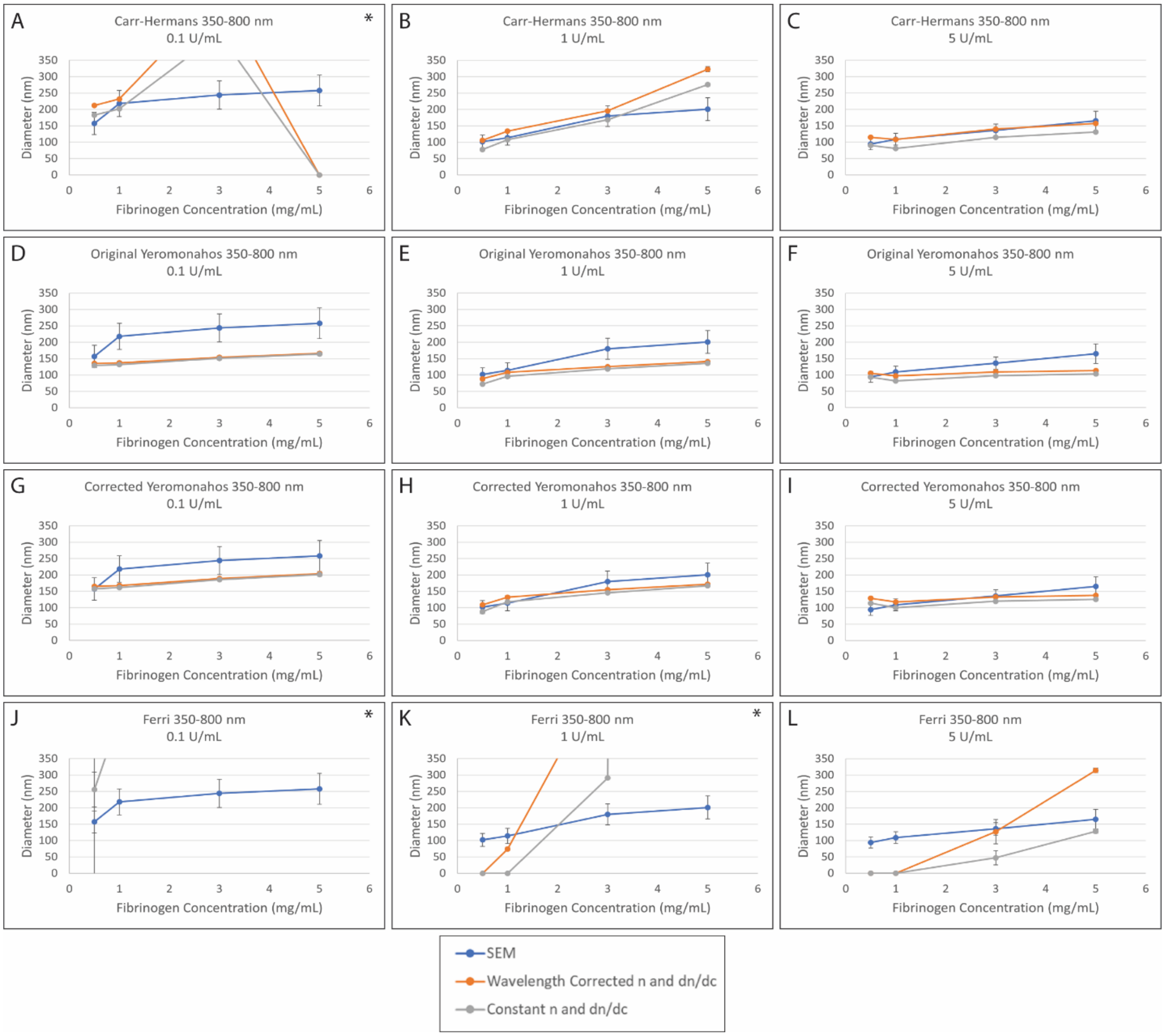

Fig. 18: Plots of diameters obtained using the different turbidimetric approaches (for wavelength corrected n and dn/dc and constant n and dn/dc) and those obtained using SEM for a wavelength range of 350-800 nm (plots with * in top right corner have some datapoints outside of the plot range; imaginary diameter values were plotted as a diameter of 0 nm).

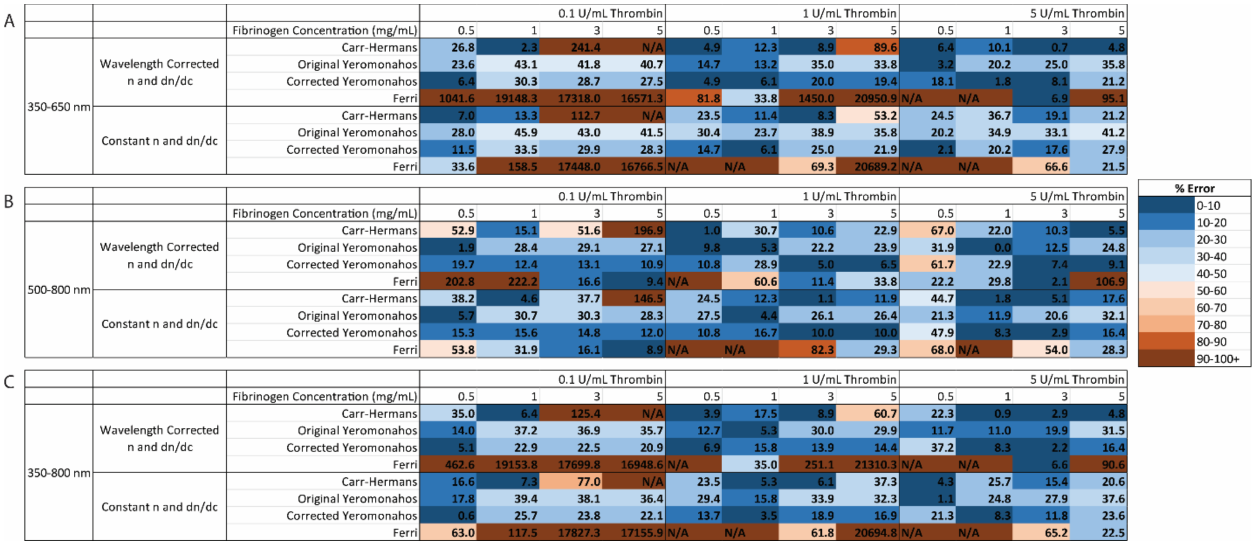

A

			0.1 U/mL Thrombin				1 U/mL Thrombin				5 U/mL Thrombin			
		Fibrinogen Concentration (mg/mL)	0.5	1	3	5	0.5	1	3	5	0.5	1	3	5
350-650 nm	Wavelength Corrected n and dn/dc	Carr-Hermans	26.8	2.3	241.4	N/A	4.9	12.3	8.9	89.6	6.4	10.1	0.7	4.8
		Original Yeromonahos	23.6	43.1	41.8	40.7	14.7	13.2	35.0	33.8	3.2	20.2	25.0	35.8
		Corrected Yeromonahos	6.4	30.3	28.7	27.5	4.9	6.1	20.0	19.4	18.1	1.8	8.1	21.2
		Ferri	1041.6	19148.3	17318.0	16571.3	81.8	33.8	1450.0	20950.9	N/A	N/A	6.9	95.1
	Constant n and dn/dc	Carr-Hermans	7.0	13.3	112.7	N/A	23.5	11.4	8.3	53.2	24.5	36.7	19.1	21.2
		Original Yeromonahos	28.0	45.9	43.0	41.5	30.4	23.7	38.9	35.8	20.2	34.9	33.1	41.2
		Corrected Yeromonahos	11.5	33.5	29.9	28.3	14.7	6.1	25.0	21.9	2.1	20.2	17.6	27.9
		Ferri	33.6	158.5	17448.0	16766.5	N/A	N/A	69.3	20689.2	N/A	N/A	66.6	21.5

B

			0.1 U/mL Thrombin				1 U/mL Thrombin				5 U/mL Thrombin			
		Fibrinogen Concentration (mg/mL)	0.5	1	3	5	0.5	1	3	5	0.5	1	3	5
500-800 nm	Wavelength Corrected n and dn/dc	Carr-Hermans	52.9	15.1	51.6	196.9	1.0	30.7	10.6	22.9	67.0	22.0	10.3	5.5
		Original Yeromonahos	1.9	28.4	29.1	27.1	9.8	5.3	22.2	23.9	31.9	0.0	12.5	24.8
		Corrected Yeromonahos	19.7	12.4	13.1	10.9	10.8	28.9	5.0	6.5	61.7	22.9	7.4	9.1
		Ferri	202.8	222.2	16.6	9.4	N/A	60.6	11.4	33.8	22.2	29.8	2.1	106.9
	Constant n and dn/dc	Carr-Hermans	38.2	4.6	37.7	146.5	24.5	12.3	1.1	11.9	44.7	1.8	5.1	17.6
		Original Yeromonahos	5.7	30.7	30.3	28.3	27.5	4.4	26.1	26.4	21.3	11.9	20.6	32.1
		Corrected Yeromonahos	15.3	15.6	14.8	12.0	10.8	16.7	10.0	10.0	47.9	8.3	2.9	16.4
		Ferri	53.8	31.9	16.1	8.9	N/A	N/A	82.3	29.3	68.0	N/A	54.0	28.3

% Error
0-10
10-20
20-30
30-40
40-50
50-60
60-70
70-80
80-90
90-100+

C

			0.1 U/mL Thrombin				1 U/mL Thrombin				5 U/mL Thrombin			
		Fibrinogen Concentration (mg/mL)	0.5	1	3	5	0.5	1	3	5	0.5	1	3	5
350-800 nm	Wavelength Corrected n and dn/dc	Carr-Hermans	35.0	6.4	125.4	N/A	3.9	17.5	8.9	60.7	22.3	0.9	2.9	4.8
		Original Yeromonahos	14.0	37.2	36.9	35.7	12.7	5.3	30.0	29.9	11.7	11.0	19.9	31.5
		Corrected Yeromonahos	5.1	22.9	22.5	20.9	6.9	15.8	13.9	14.4	37.2	8.3	2.2	16.4
		Ferri	462.6	19153.8	17699.8	16948.6	N/A	35.0	251.1	21310.3	N/A	N/A	6.6	90.6
	Constant n and dn/dc	Carr-Hermans	16.6	7.3	77.0	N/A	23.5	5.3	6.1	37.3	4.3	25.7	15.4	20.6
		Original Yeromonahos	17.8	39.4	38.1	36.4	29.4	15.8	33.9	32.3	1.1	24.8	27.9	37.6
		Corrected Yeromonahos	0.6	25.7	23.8	22.1	13.7	3.5	18.9	16.9	21.3	8.3	11.8	23.6
		Ferri	63.0	117.5	17827.3	17155.9	N/A	N/A	61.8	20694.8	N/A	N/A	65.2	22.5

Fig. 19: Percent error in the diameter obtained from each investigated turbidimetric approach compared to diameters obtained from SEM for a wavelength range of A) 350-650 nm, B) 500-800 nm, and C) 350-800 nm (N/A represents an imaginary diameter value from the turbidimetric approach).

Wavelength Dependence of n and dn/dc

As seen by comparing the orange and gray lines of the individual plots in Figures 16-18, diameter values obtained when accounting for the wavelength dependence of n and dn/dc are very similar to those obtained when using constant values of n and dn/dc. However, the diameters obtained when accounting for the wavelength dependence of those terms is closest to those obtained from SEM imaging for most clot conditions investigated, as shown in Table 6.

	Percent of Clot Conditions with Diameter Closest to SEM Diameter*
Wavelength Corrected n and dn/dc	60.4%
Constant n and dn/dc	20.9%

Table 6: Percent of investigated clot conditions in which the diameters obtained using wavelength corrected values of n and dn/dc or constant values of n and dn/dc resulted in diameters closest to those from SEM imaging (*Total error does not add up to 100% because neither was counted if they both gave imaginary values and both were counted if they contained equal percent errors).

Based on these results, combined with our results comparing the different turbidimetric approaches to full light scattering theory in Chapter 2, and previously reported results [18,34], it is clear that it is necessary to account for the wavelength dependence of n and dn/dc in the fitting process.

Wavelength Range Effects

The wavelength range of 500-800 nm results in the diameter values being closest to those obtained using SEM imaging for most of the investigated clot conditions, as shown in Table 7.

Wavelength Range	Percent of Clot Conditions with Diameter Closest to SEM Diameter*
350-650 nm	18.2%
500-800 nm	64.1%
350-800 nm	16.1%

Table 7: Percent of investigated clot conditions in which the diameters obtained using a wavelength range of 350-650 nm, 500-800 nm, or 350-800 nm resulted in diameters closest to those from SEM imaging (*Total error does not add up to 100% because none were counted if they all gave imaginary values and multiple were counted if they contained equal percent errors).

Based on these results, combined with the simulated results of Chapter 2, it is evident that the wavelength range of 500-800 nm results in more accurate diameter values than using the 350-650 nm wavelength range or 350-800 nm range. While it might be assumed that the more datapoints the better, there is actually a slight curvature to most of the plots when looking at the full 350-800 nm, which is minimized when looking at only 350-650 nm or 500-800 nm. This can be seen visually by the representative turbidimetric fitting plots, and quantitatively by the squared correlation coefficients between the datasets and the fitting equations, which are provided in Appendix C.5.

Best Turbidimetric Approach

Since it is apparent that using wavelength corrected values of n and dn/dc in the fittings and utilizing a wavelength range of 500-800 nm results in the most accurate diameter values, we investigated which approach was the best under those conditions. A color-coded error chart showing the percent error between the diameter values obtained using each of the turbidimetric approaches and those obtained using SEM imaging can be seen in Figure 20. As shown, all of the approaches result in fairly large amounts of error overall for the fibers with small diameter values, especially under 100 nm. Between 102 to 157 nm, the Original Yeromonahos approach provides less than 20% error. For larger diameters, the Corrected Yeromonahos approach was the most consistently reliable, resulting in less than 20% error for all clots with fibers of 136 nm diameter or larger. The Carr-Hermans approach did not work well for the largest diameter values, which makes sense since it contains an additional simplification from light scattering theory assuming that the fibers are thin. It also did not work well for a diameter of 157 nm, which corresponds to a fibrinogen concentration of 0.5 mg/mL and thrombin concentration of 0.1 NIH-U/mL. It appears that this could be due to experimental error rather than a failure of the Carr-Hermans approach, as it was previously found that the Carr-Hermans worked well for this concentration [1], and it worked well for this concentration when using the cuvette for measurements. There was a lot of variability and no clear trend on which diameter values the Ferri approach provided values similar to those from SEM imaging.

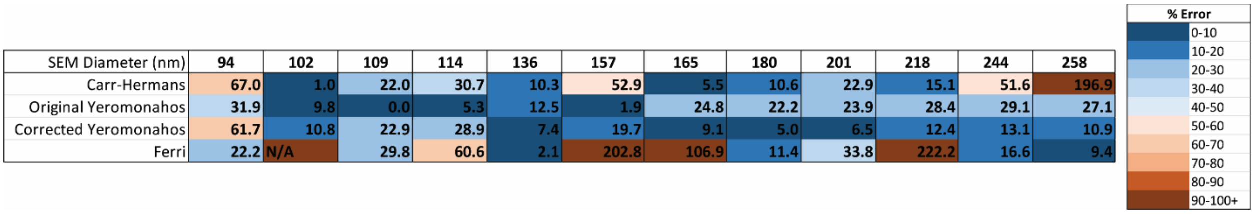

SEM Diameter (nm)	94	102	109	114	136	157	165	180	201	218	244	258
Carr-Hermans	67.0	1.0	22.0	30.7	10.3	52.9	5.5	10.6	22.9	15.1	51.6	196.9
Original Yeromonahos	31.9	9.8	0.0	5.3	12.5	1.9	24.8	22.2	23.9	28.4	29.1	27.1
Corrected Yeromonahos	61.7	10.8	22.9	28.9	7.4	19.7	9.1	5.0	6.5	12.4	13.1	10.9
Ferri	22.2	N/A	29.8	60.6	2.1	202.8	106.9	11.4	33.8	222.2	16.6	9.4

	% Error
■	0-10
■	10-20
■	20-30
■	30-40
■	40-50
■	50-60
■	60-70
■	70-80
■	80-90
■	90-100+

Fig. 20: Percent error in the diameter obtained from each investigated turbidimetric approach compared to diameters obtained from SEM for a wavelength range of 500-800 nm, with the wavelength dependence of n and dn/dc accounted for, arranged for in order of increasing diameter according to SEM analysis (N/A represents an imaginary diameter value from turbidimetric approach).

While our simulated results of Chapter 2 suggested that the Carr-Hermans approach is the most accurate, this is often not the case when the full range of possible fibrinogen and thrombin concentrations are considered.

Furthermore, Ferri et al. and Vos [18,34] reported that the Ferri approach is the most accurate of the methods; however, this was based on the Ferri fitting equation having lower residuals than the other methods, meaning it best described the dataset. When we looked at the squared correlation coefficients for each of the clot conditions, we also found the Ferri approach to best fit many of the datasets – with the correlation being the highest for the Ferri approach in 43.06% of the clot conditions analyzed. However, it only provided the closest diameter to that obtained from SEM imaging in 5.56% of clot conditions, showing that just because the equation fits the dataset the closest doesn't necessarily mean that it results in the most accurate diameter values. We found that the approach with the best correlation was the one with the closest diameter to that obtained from SEM imaging in only 37.5% of the investigated conditions.

Since the Ferri approach also involves a secondary experimental technique to determine the pore size and mass fractal dimension, this could introduce additional error into its use for determining the fibrin fiber diameter, especially since the pore sizes are nonuniform throughout the sample, resulting in only the average value being obtainable, which could easily be skewed by very large or very small pores. Furthermore, we used confocal imaging for determining the pore size and mass fractal dimension, which Ferri et al. [18] argue is not the most reliable method for determining those parameters. This could have led to the poor accuracy of the Ferri approach in determining the fiber diameter for our analysis. A deeper analysis of the effects error in those parameters would have on the calculated fiber diameter is discussed in Appendix C.6, where we found that small errors in the mass fractal dimension cause a large difference in the calculated fiber diameter for thin fibers. Therefore, it is possible that the Ferri fitting approach would have provided more accurate fiber diameter measurements had we used an alternative method for determining the pore size and mass fractal dimension, such as low-angle elastic light scattering.

Although we found that the "correction" to the Yeromonahos approach was obtained erroneously, as described in Chapter 1, the Corrected Yeromonahos approach using a wavelength range of 500-800 nm and wavelength corrected n and dn/dc provided less than twenty percent error for clots with diameters of 136 nm and larger, and therefore appears to be the most versatile of the approaches/conditions. It was also able to result in less than twenty percent error for all four fibrinogen concentrations when using 0.1 U/mL thrombin, and for fibrinogen concentrations of 3 and 5 mg/mL when using 1 and 5 U/mL thrombin. The only time this approach appears to fail is when applied to very thin fibers, created with small amounts of fibrinogen and large amounts of thrombin. Caution should, therefore, be used if analyzing very thin fibers, less than ~136 nm, or when analyzing fibers larger than ~258 nm in diameter, as that is the largest average diameter investigated in this work.

Adjusted Turbidimetric Approach

Since the results of Figure 20 display the percent error, they do not indicate whether the turbidimetry over- or underestimates the experimental SEM values. We decided to explore this further for the Corrected Yeromonahos approach using a wavelength range of 500-800 nm, with n and dn/dc wavelength corrected. Figure 21 plots the turbidimetry and SEM diameters as a function of SEM diameter and shows that turbidimetry systematically overestimates diameters less than 165 nm and underestimates diameters greater than 165 nm.

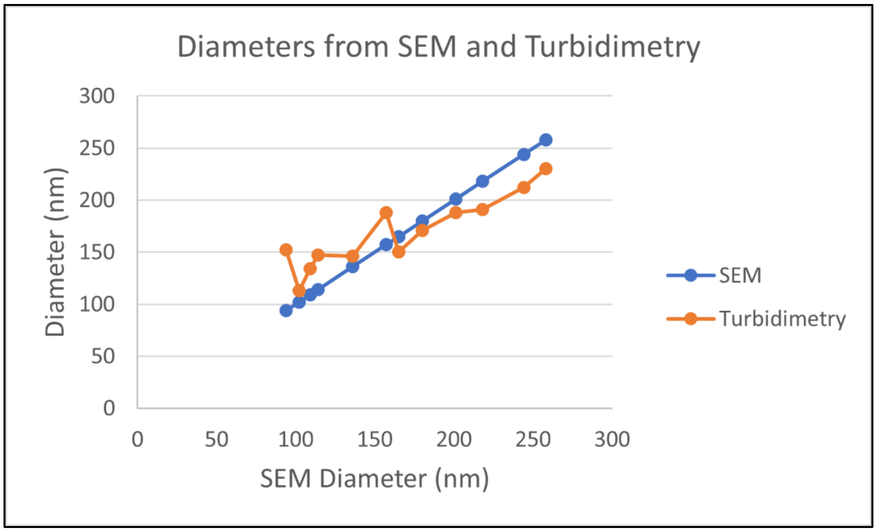

Fig. 21: Diameter values obtained from SEM imaging and from the Corrected Yeromonahos approach (using a wavelength range of 500-800 nm, with the wavelength dependence of n and dn/dc accounted for, in a 96-well plate).

Based on these results, we created a post hoc adjustment function that corrects for the systematic over- and underestimate of the turbidimetry values. To create this adjustment, a plot was made of the diameters obtained using SEM versus those obtained using the Corrected Yeromonahos approach for every clot condition investigated. This was done separately for those in which the turbidimetry diameter overestimates the SEM diameter (94-157 nm), and those in which it underestimates the SEM diameter (165-258 nm), as shown in Figure 22.

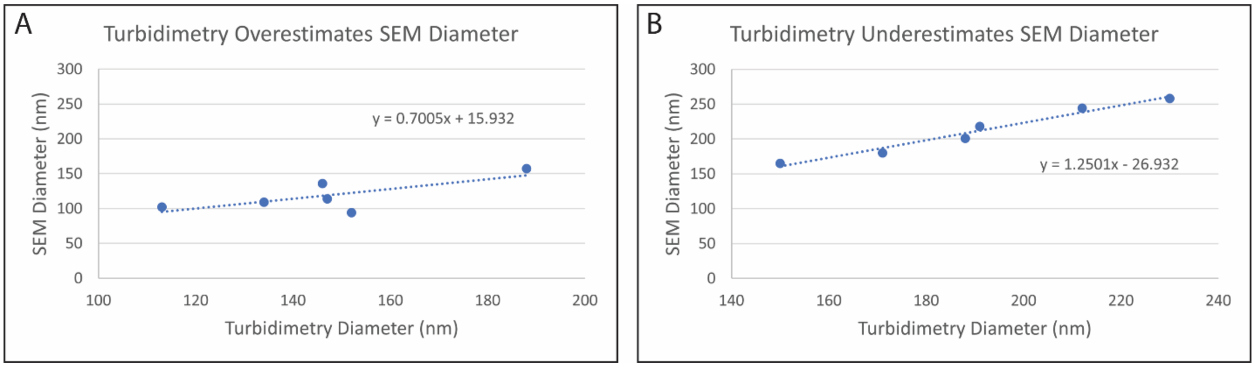

Fig. 22: Diameter values obtained using SEM vs. those obtained from turbidimetry for cases where A) turbidimetry overestimates SEM diameter (94-157 nm), and B) turbidimetry underestimates SEM diameter (165-258 nm) (using the Corrected Yeromonahos approach, with a wavelength range of 500-800 nm, accounting for the wavelength dependence of n and dn/dc; equation represents linear line of best fit).

The plots were then fit with a linear line and the equations for each line were used as a correction. The following equations define the post hoc adjustment:

$$d_{adjusted} = \begin{cases} 0.7005 * d_{CorrYer} + 15.932 & d_{CorrYer} < 160\ nm \\ 1.2501 * d_{CorrYer} - 26.932 & d_{CorrYer} \geq 160\ nm \end{cases} \qquad [54]$$

The percent error in the adjusted diameter values for each clot condition versus those from the Corrected Yeromonahos approach alone can be seen in Figure 23. Applying the adjustment reduces the difference between the diameter values obtained using the Corrected Yeromonahos approach and those obtained from SEM by an average of 6.7%.

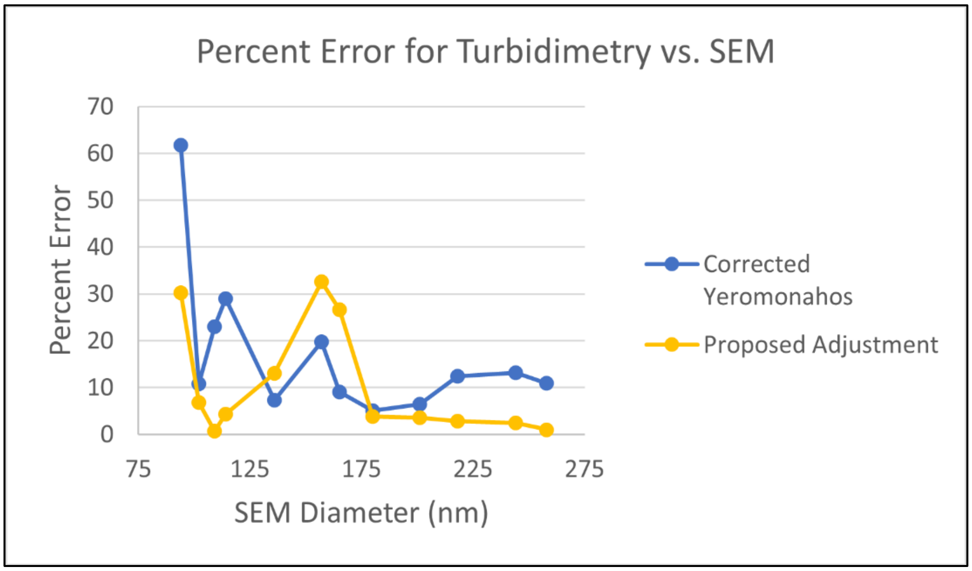

Fig. 23: Percent error in the diameter values obtained with turbidimetry compared to SEM when using the Corrected Yeromonahos approach alone (blue) versus when using the proposed adjustment (yellow) (Wavelength range of 500-800 nm, with n and dn/dc wavelength corrected).

Comparing the diameter values obtained using SEM, super-resolution imaging, and turbidimetry with our proposed adjustment, all three methods provide diameter values within 3% of one another when using 1 mg/mL fibrinogen and 0.1 NIH-U/mL thrombin. As this is an easily accessible concentration for most labs, utilizing relatively small amounts of sample, we recommend using these concentrations as a standard for structural analysis of fibrin fibers with purified fibrinogen.

Cuvette vs. 96 Well Plate

Since turbidimetry measurements can be performed in either a cuvette or a 96 well plate, we wanted to determine if there are any conditions in which one method is better than the other. A figure showing the percent error in the diameter obtained using each turbidimetric fitting approach versus the fiber diameter for each of the three investigated wavelength ranges when using a cuvette and when using a 96 well plate for measurements is shown in Appendix C.7. Based on those plots, there does not appear to be any clear trend to when a cuvette or 96 well plate is better for measurements. We furthermore plotted the percent error in the obtained diameters for each fitting approach versus the fibrinogen concentration when using a wavelength range of 500-800 nm, also shown in Appendix C.7. Again, there does not appear to be any clear trend in when either the 96 well plate or cuvette is more accurate.

Figure 24 shows the average diameter values obtained using the two methods for each fibrinogen/thrombin concentration with a wavelength range of 500-800 nm, with the wavelength dependence of n and dn/dc accounted for, for each of the four turbidimetric fitting approaches. A color-coded table of the percent error in each of the approaches using the two methods for all clot conditions is shown in Appendix C.7.

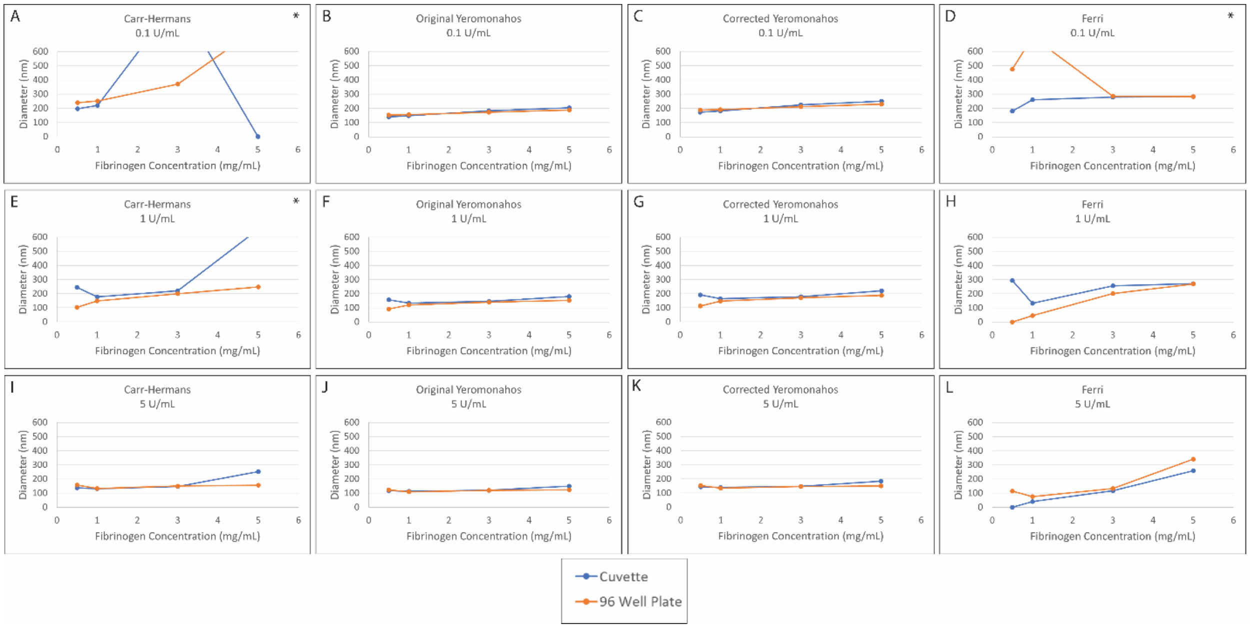

Fig. 24: The diameter value obtained for each turbidimetric approach at the four investigated fibrinogen concentrations with thrombin concentrations of 0.1 U/mL (top row), 1 U/mL (middle row), and 5 U/mL (bottom row) using a cuvette (blue) and 96-well plate (orange) (using a wavelength range of 500-800 nm, with the wavelength dependence of n and dn/dc accounted for; * in the top right corner of the plot means some data is outside of the plot range; imaginary diameter values were represented as a diameter of 0 nm).

As seen, there is good agreement between the diameter values obtained using the two different mechanisms for most investigated fibrinogen/thrombin concentrations, with three exceptions: when the fibrinogen concentration is high and thrombin concentration is low, resulting in thick fibers, when using a concentration of 0.5 mg/mL fibrinogen with 1 U/mL thrombin, and when using the Ferri approach at low fibrinogen concentrations, especially when also using low thrombin concentrations.

The first of these scenarios, when the fibrinogen concentration is high and thrombin concentration is low, is due to limitations of our cuvette reader. Figure 25 shows the absorbance measurements over time taken as the clots formed for samples measured in both a cuvette and 96 well plate. As can be seen, when using high fibrinogen concentrations (3 or 5 mg/mL), and especially when also using low thrombin concentrations, the cuvette measurements reach their maximum absorbance limit, causing the absorbance curves to become less smooth and max out at an absorbance of approximately 2.6, unlike the 96 well plate measurements which remain smooth and increase with increasing fibrinogen concentration. When using a cuvette, the pathlength was 1 cm, rather than the ~0.45 cm pathlength used in the 96 well plate. As the fibers become thicker, they scatter more light, and thus less light is transmitted through the sample. As the sample pathlength that the light has to travel through increases, the amount of light making it all the way through the sample is decreased even further. Therefore, when the fibers become thicker, the amount of light making it all the way through the sample decreased so much that the cuvette was no longer able to get reliable "absorbance" measurements. This problem did not occur in the 96 well plates since the light had less sample that it needed to travel through.

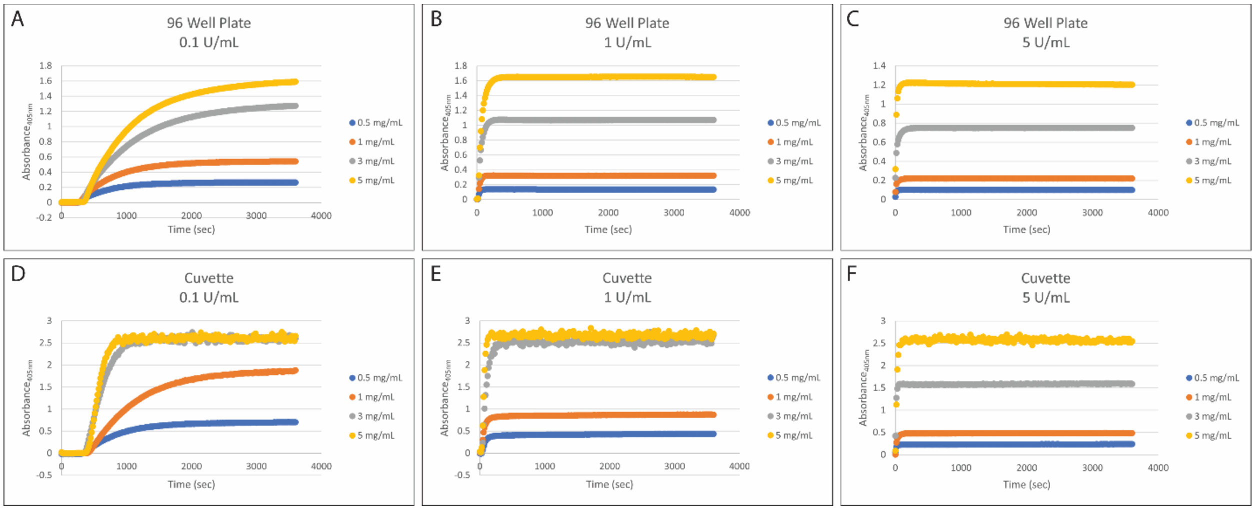

Fig. 25: Absorbance measurements over time as the clot polymerizes for each investigated fibrinogen/thrombin concentration using either a 96 well plate (top row) or cuvette (bottom row).

The second scenario in which the cuvette and 96 well plate diameters disagree is for a fibrinogen concentration of 0.5 mg/mL with a thrombin concentration of 1 U/mL. Looking at the diameter values for the two methods in Figure 24, it can be seen that for all four of the turbidimetric approaches, the diameters increase with increasing fibrinogen concentration, as expected, except for the clots made with 0.5 mg/mL fibrinogen and either 1 or 5 U/mL thrombin. This is due to the fact that the fibers are so thin that the diameter can no longer be reliably determined. For the sample with 0.5 mg/mL fibrinogen and 5 U/mL thrombin, the average diameter was the smallest investigated (94 nm), and both the cuvette and 96 well plate show this as having a larger diameter than the sample with the next highest fibrinogen concentration at this thrombin concentration. For the sample with 0.5 mg/mL and 1 U/mL thrombin, the average diameter was the next smallest we analyzed (102 nm), and the cuvette shows it having a larger diameter value than the next higher fibrinogen concentration at this thrombin concentration, but the 96 well plate does not. This implies that the 96 well plate allows for the reliable determination of fibers down to approximately 102 nm, while the cuvette reader is only able to be used for fibers down to approximately 109 nm diameter.

Finally, the diameter values obtained using the 96 well plate and cuvette differ when using the Ferri fitting approach for low fibrinogen concentrations, especially when also using low thrombin concentrations. This is likely due to error in the calculations of the pore size from the confocal images for these samples. Our measurements showed the largest pore sizes for samples made with 0.5 or 1 mg/mL fibrinogen, with 0.1 U/mL thrombin. Those samples also had the largest standard deviation in the pore size measurements, implying that there is larger heterogeneity in the pore sizes at those concentrations than at the other concentrations. With the larger amount of heterogeneity in the pore sizes, the average would be a less accurate estimation, which could have led to the Ferri fitting approach being less accurate.

Due to these limitations, it is suggested to use a 96 well plate if analyzing thicker fibers, formed with high fibrinogen concentrations and low thrombin concentrations, and to use an alternative method if analyzing very thin fibers, less than approximately 100 nm in diameter. Our results contradict those published previously [62] which compared calculation of the mass-length ratio for fibers formed in a plate versus in a cuvette. They reported that plate readers could be used for qualitatively analyzing fibrin structure, but that a cuvette should be used if exact values are needed. It is unclear, however, if/how they calculated the pathlength of the plate reader samples, so that could be the cause of the discrepancy.

Although we elected to perform our main analysis of the different turbidimetric fitting approaches based on measurements performed in a 96 well plate, the results are similar when also accounting for the measurements performed in a cuvette. When accounting for both measurement techniques, diameters obtained when accounting for the wavelength dependence of n and dn/dc are still closest to those obtained from SEM imaging in 57.6% of the investigated clot conditions. Furthermore, the 500-800 nm wavelength range results in the closest estimations of diameter to those from SEM in 64.1% of clot conditions analyzed, and the Corrected Yeromonahos approach still results in less than 20% error for all fiber conditions with diameters of 136 nm or larger. Therefore, the method used for measurement does not change our overall claims on which clot conditions result in the most accurate measurements of fiber diameter.

Effect of Sample Volume on Cuvette Measurements

We furthermore looked at the effect of changing volume on the cuvette measurements, as we hypothesized that the more volume used, the more the fibers toward the bottom of the cuvette would be compacted due to the weight of the fibers on top of them. This would lead to increased scattering as the fibers would be more densely packed together. To test this, we ran absorbance measurements on clots containing 70, 100, and 130 μL sample volumes to look at differences in the polymerization curves. The polymerization curves are shown in Figure 26, with the lag phase, rate of polymerization, and maximum absorbance values provided in Table 8.

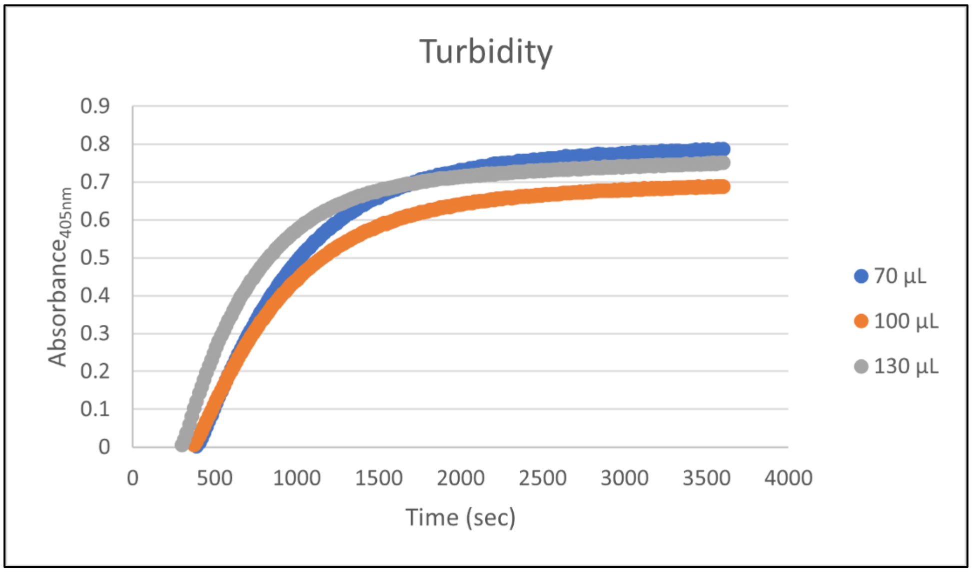

Fig. 26: Absorbance measurements over time as the clot polymerizes for clots created using 0.5 mg/mL fibrinogen, 0.1 U/mL thrombin, 25 L-U/mL FXIIIa, with final sample volumes of 70, 100, and 130 µL.

Volume (µL)	Lag Time (sec)	Rate of Polymerization (Abs/sec)	Max Absorbance
70	389.73	0.0008	0.79
100	390.26	0.0007	0.69
130	315.02	0.0007	0.75

Table 8: The lag time, rate of polymerization, and maximum absorbance values of the polymerization curves for sample volumes of 70, 100, and 130 µL.

The lag time is the time required for protofibril formation [63] and is determined by an absorbance increase of 0.015 from the first measurement [64]. While there is a slightly longer lag time for the sample volume of 130 µL, the samples were not performed at the same time so this is likely due to a difference in reaction time of starting the measurements after adding the thrombin mixture rather than a difference in time for protofibril formation. The rate of polymerization is determined by the slope of the upward increase in the absorbance measurements and was similar for all three samples. The maximum absorbance, which is related to the fiber thickness of the fully formed clot, differed slightly between the three samples, but it does not follow a trend between the samples, so the differences are likely due to experimental variation rather than a difference due to the sample volume.

To further test the differences between the sample volumes, we performed turbidimetry measurements on the fully formed clots. The absorbance versus wavelength plots for the three samples are shown in Figure 27. As seen, the three curves are very similar.

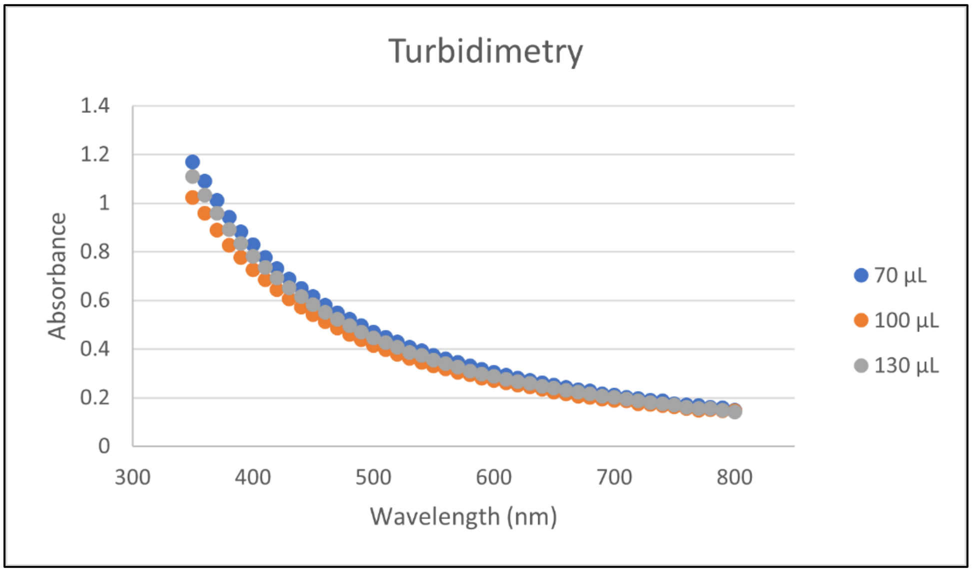

Fig. 27: Absorbance measurements over a wavelength range of 350-800 nm on fully formed clots created using 0.5 mg/mL fibrinogen, 0.1 U/mL thrombin, 25 L-U/mL FXIIIa, with final sample volumes of 70, 100, and 130 µL.

We then used the turbidimetry measurements from 500-800 nm and fit them with the Corrected Yeromonahos approach in order to determine the average fiber diameters of the three samples, which are provided in Table 9. The diameter values for the sample containing 70 µL and 130 µL were only 1 nm apart, with the diameter value for the 100 µL sample being slightly larger. Because the diameters obtained using the 70 µL and 130 µL samples were so similar, there does not appear to be any effect on the fiber diameter measurements due to the sample volume used.

Sample Volume (μL)	**Diameter (nm)**
70	172 ± 3
100	185 ± 5
130	173 ± 3

Table 9: The diameter values obtained using the Corrected Yeromonahos approach with a wavelength range of 500-800 nm, accounting for the wavelength dependence of n and dn/dc, on clots containing 0.5 mg/mL fibrinogen, 0.1 U/mL thrombin, 25 L-U/mL FXIIIa, with final sample volumes of 70, 100, and 130 μL.

We further tested our theory that the fibers toward the bottom of the sample are being compressed by the weight of the fibers on top of them by analyzing the fiber density and fiber length throughout the height of a sample, as discussed in Appendix C.8. While we do find that there is a slight increase in fiber density and a slight decrease in fiber length toward the bottom of the sample compared to those at the top of the sample, suggesting that there is some compression of the fibers, it is not a very drastic change, and combined with the turbidity and turbidimetry results above, it does not appear that it causes a significant change to the fiber diameter, and thus is not a grave concern for measurements performed in a cuvette.

Multiple Scattering Effects

It is likely that for clots containing very densely packed fibers, such as those created with large amounts of thrombin, the light will be scattered off of more than one fiber within the sample. This could lead to light that has been scattered being redirected back toward the detector. However, turbidimetry does not account for multiple scattering, so this could lead to underestimations in the fiber diameter for these clots. One method of reducing multiple scattering effects is by making the light travel through a smaller opening, which would block some of the light coming from indirect angles. It can be reduced even further by making the light travel through multiple sets of small openings.

In order to determine the effect of multiple scattering on our samples, we took the turbidimetry measurements for each sample with no cover, with a cover of smaller holes centered above each well, and with two covers of smaller holes stacked on top of one another and centered on top of the wells. In order to make sure none of the incident beam was being blocked by these covers, we made the diameter of each hole larger than the width of the incident beam. These covers can be seen in Figure 28.

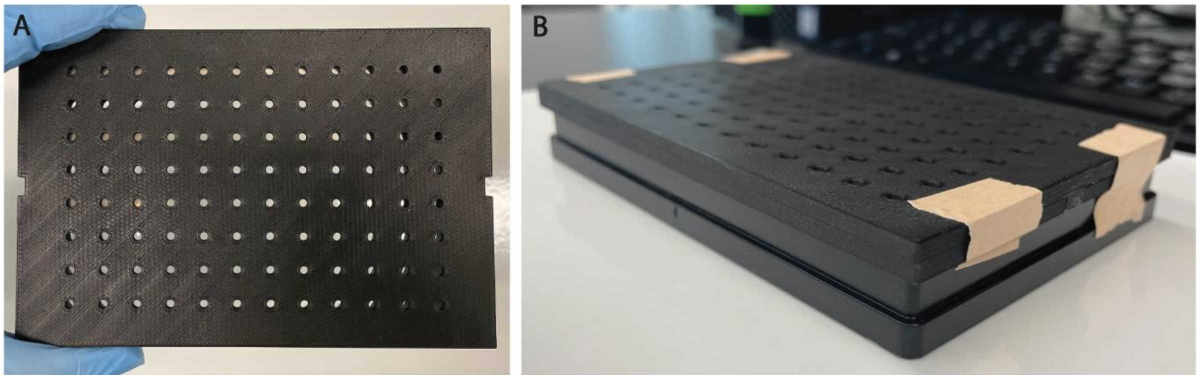

Fig. 28: Images of the 3D printed cover(s) placed on top of the 96 well plates designed to block some multiple scattered light.

The diameter values obtained from our measurements performed with no cover, one cover, and both covers can be seen in Figure 29 for each turbidimetric approach using a wavelength range of 500-800 nm, with the wavelength dependence of n and dn/dc accounted for. As seen, the diameter values obtained when using either one or two covers are usually further from those obtained from SEM imaging than the ones taken with no cover for most clot conditions. This is possibly due to the beam not being perfectly centered on the wells, or being wider than the company said, which resulted in us blocking some of the light that was transmitted through the sample, as discussed more in Appendix C.9. Therefore, we cannot draw any definitive conclusions from the results.

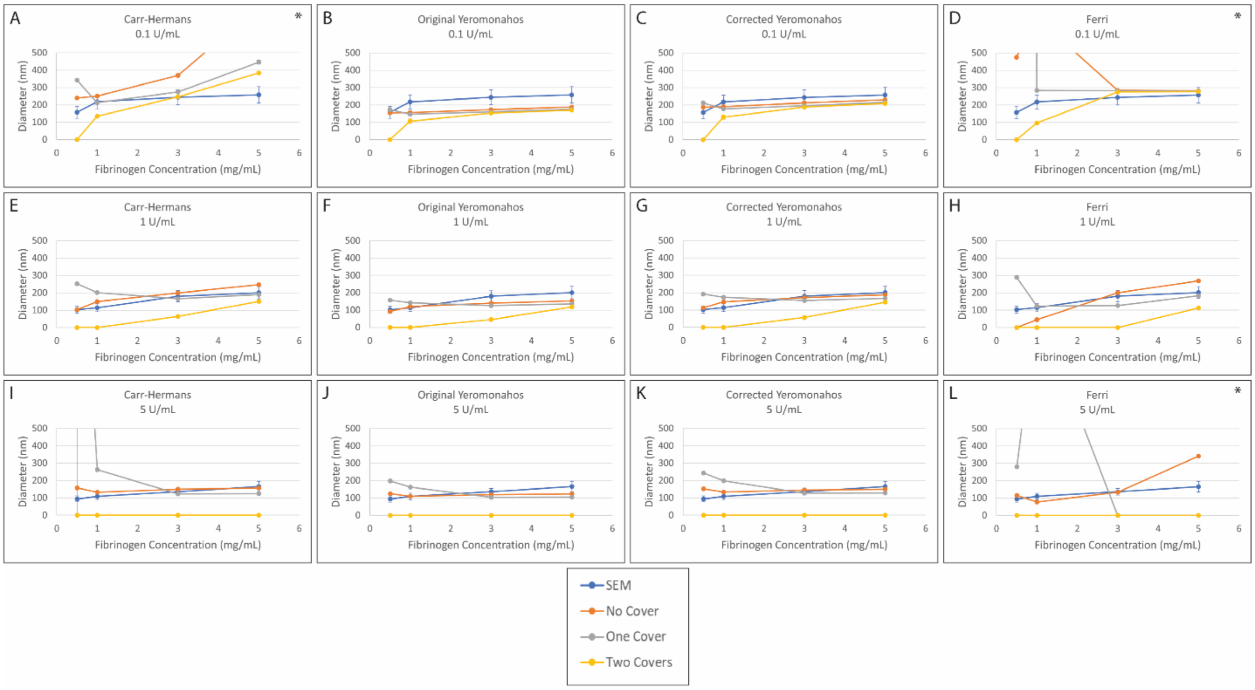

Fig. 29: Average diameter values obtained from SEM imaging (blue) and from the turbidimetric fitting approaches using a 96 well plate with no cover (red), one cover (gray), or two covers (yellow) (500-800 nm wavelength range, wavelength dependence of n and dn/dc accounted for; * in top right corner means some datapoints outside of plot range; imaginary diameter values represented as a diameter or 0 nm).

Turbidimetry Over Time

Although turbidimetry is typically used on a fully formed clot in order to determine the final average diameter, it is also possible to use the Carr-Hermans, Original Yeromonahos, or Corrected Yeromonahos approach to determine the diameter over time as the clot is forming. It is not possible with the Ferri approach, however, as that requires the concentration in the fitting equation, which is unknown precisely during the polymerization process.

This method of taking turbidimetry measurements over time is how the Yeromonahos approach has been used clinically for predicting the risk of bleeding or thrombosis [35], although it makes use of the number of protofibrils over time rather than the average diameter over time, and only requires measurements at two wavelength values between 450 and 850 nm. There are noticeable differences in fiber polymerization between plasma taken from normal patients, hypercoagulant patients, and hypocoagulant patients, so by looking at the structural differences over time as a clot forms, it is possible to predict if someone is at risk of bleeding or thrombosis.

In order to determine the average diameter measurements over time, it is necessary to have a spectrophotometer capable of taking absorbance measurements over time at multiple wavelength values simultaneously. To determine the average diameter measurements over time on a clot containing 1 mg/mL fibrinogen, 0.1 U/mL thrombin, and 25 L-U/mL FXIIIa, we took absorbance measurements every 30 seconds for 1 hour with measurements taken every 50 nm from 500-800 nm. The results are shown in Figure 30. For the first six minutes, the approaches provided imaginary values, which are plotted as a diameter of 0 nm. The diameter value obtained from SEM imaging for this concentration was 218 nm, and is plotted as a yellow line across all timepoints. Although in these results the Carr-Hermans approach is the one which is the closest to the SEM diameter after polymerization is complete, apparently contradicting our previous results reporting that the Corrected Yeromonahos approach is the most accurate for this wavelength range and fibrinogen/thrombin concentration (see Figures 17 and 19), the results provided in Figures 17 and 19 are for measurements performed in a 96 well plate, while these measurements were performed in a cuvette. As shown in Figure C.14, the Carr-Hermans approach actually provides less error for this fibrinogen/thrombin concentration when using a cuvette than the Corrected Yeromonahos approach. However, even for measurements performed in a cuvette, the Corrected Yeromonahos still provides the most accurate values of diameter for the most fibrinogen/thrombin concentrations investigated.

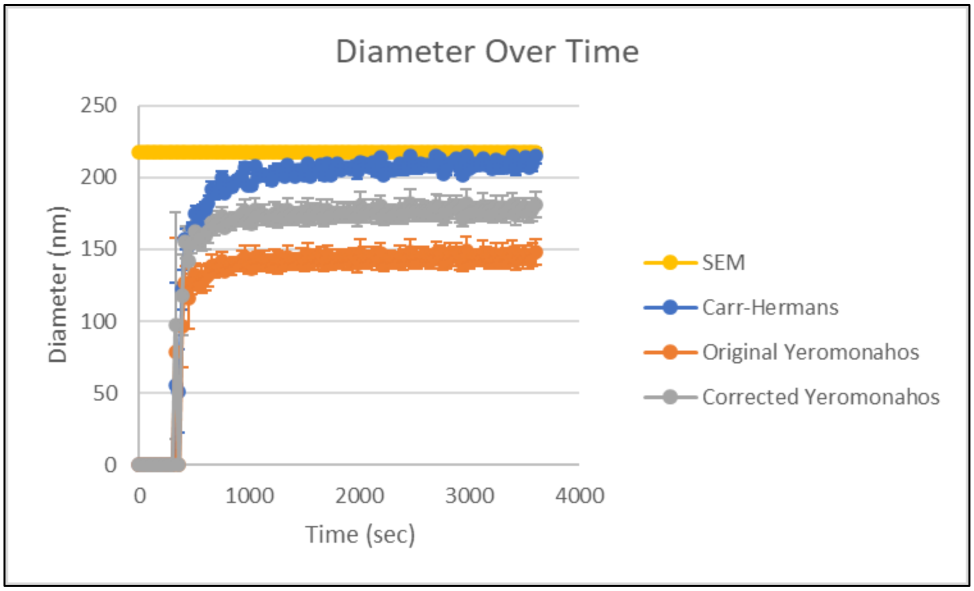

Fig. 30: Average diameter values over time according to the Carr-Hermans, Original Yeromonahos, and Corrected Yeromonahos approaches for a clot containing 1 mg/mL fibrinogen, 0.1 U/mL thrombin, 25 L-U/mL FXIIIa.

Conclusion

In this work, we have provided a comparison between diameter values obtained using SEM imaging, super resolution imaging, and the four different commonly utilized turbidimetric approaches for a range of physiologically relevant clot conditions, in order to determine in which cases and using what parameters each method is able to provide accurate results. The first important takeaway from our results is that the diameter values obtained when using SEM imaging and when using STORM imaging are remarkably similar, suggesting that there are not large structural differences caused by the drying, fixation, and sputter coating required for SEM sample preparation.

The next important takeaway is that there are structural differences caused by the presence of fibrinogen aggregates, so it is important to be consistent in which stock solutions are being used, and to not put the samples through multiple freeze/thaw cycles which introduces new aggregates. There are also structural differences caused by centrifugally concentrating the samples, so this should be limited or remain consistent between samples.

Furthermore, we experimentally confirmed our claim in Chapter 2 that it is necessary to account for the wavelength dependence of the refractive index and specific refractive index increment, as using constants for these terms results in less accurate estimations of the fiber diameters. We also experimentally confirmed our previous claim that using a wavelength range of 500-800 nm provides more accurate diameter values than using a 350-650 nm wavelength range, and showed that it is also more accurate than using the entire range of 350-800 nm.

In contrast to our simulated results, we found that the Corrected Yeromonahos approach is often the most accurate of the turbidimetric approaches, providing diameter estimations with less than 20% error for all fibers with average diameters of 136 nm or larger. None of the approaches were able to provide accurate diameter values for fibers of approximately 100 nm thickness or smaller, so an alternate method such as SEM or super resolution imaging should be utilized if analyzing very thin fibers. Furthermore, we found that for high fibrinogen concentrations, the measurements performed in a cuvette reach their maximum absorbance measurements and are unable to provide reliable diameter values, so it is best to use a 96 well plate if utilizing fibrinogen concentrations of 3 mg/mL or more.

Finally, we have shown that it is possible to use the Carr-Hermans, Original Yeromonahos, and Corrected Yeromonahos approach for determining structural information over time, which can be used for comparing clot formation under different conditions, such as in a lab looking at the effects of different conditions on the clot structure (such as varying concentrations, pH levels, calcium concentrations, the addition of other proteins, etc.) or in a clinic looking at the risk of bleeding or thrombosis.

To summarize, turbidimetry offers a quick estimation of fiber diameter; however, it is necessary to use the appropriate technique and conditions in order to obtain accurate measurements. It should not be used for analyzing very thin fibers, and should be performed in a 96 well plate if analyzing very large fibers. The wavelength dependence of the refractive index and specific refractive index increment should be accounted for in the turbidity plots, and a wavelength range of 500-800 nm, or a similar range resulting in linear plots, should be used for measurements. Finally, the Corrected Yeromonahos approach should be used unless the range of diameter values is known and it is confirmed that one of the other approaches works well for those conditions.

CHAPTER 4: COMPARISON OF THEORETICAL AND EXPERIMENTAL ANALYSIS

Introduction

In order to determine how accurately the simulated error based on comparisons of the turbidimetric approaches to full light scattering theory actually matched experimental error, we compared predicted percent error based on the simulations to the experimental percent error between the diameter values obtained from the different turbidimetric approaches to those obtained from SEM imaging. Since our simulations were only for the Carr-Hermans, Original Yeromonahos, and Corrected Yeromonahos approaches, due to the Ferri approach requiring additional experimental techniques, those three are the ones we will compare in this chapter.

Methods

The Mathematica code used for analysis in Chapter 2 was used for determining the predicted percent error for each investigated clot condition, with fibrinogen concentrations of 0.5, 1, 3, and 5 mg/mL and thrombin concentrations of 0.1, 1, and 5 U/mL. The diameter values used were the averages found for each clot condition from SEM imaging, and the average length obtained for each clot condition based on confocal imaging was input as the fiber length. The mass-length ratio input was $4.73*10^{12}$ Da/cm; however, as explained in Chapter 2, the results are independent of the input mass-length ratio. The Mathematica code then provided the percent error in the diameter value obtained using the Carr-Hermans approach, Original Yeromonahos approach, or Corrected Yeromonahos approach compared to the input diameter value. This was done for wavelength corrected values of the refractive index and specific refractive index increment, as well as using the spectral average for those terms (as provided in Chapter 3). It was also done for a wavelength range of 350-650 nm, 500-800 nm, and 350-800 nm.

The experimental percent error values used for each clot condition/wavelength range were the error between the diameter values obtained from each of the three approaches fit to experimental turbidimetry data and those obtained from SEM imaging, as provided in Chapter 3. This was done for measurements performed in a 96 well plate, as well as those performed in a cuvette.

Results and Discussion

The predicted percent error and the experimental percent error for measurements performed in a 96 well plate and in a cuvette, with the wavelength dependence of n and dn/dc accounted for, are shown in Figures 31-33, for a wavelength range of 350-650 nm, 500-800 nm, and 350-800 nm, respectively. The percent errors when using constant values of n and dn/dc are shown in Figures 34-36 for each of the investigated wavelength ranges. The predicted percent error was the error between the diameter input into the full light scattering theory equation (d_{LST}) (Equation 9) and the diameter obtained from fitting the theoretical turbidity dataset created from full light scattering theory with each of the turbidimetric approach equations (d_{turb_sim}), such that:

$$Predicted\ \%\ Error = \left|\frac{d_{LST} - d_{turb\_sim}}{d_{LST}}\right| \times 100 \qquad [55]$$

The experimental percent error was the error between the average diameter value obtained from SEM imaging (d_{SEM}) and the diameter obtained from fitting an experimental turbidimetry dataset with each of the turbidimetric approach equations (d_{turb_exp}), such that:

$$Experimental\ \%\ Error = \left|\frac{d_{SEM} - d_{turb\_exp}}{d_{SEM}}\right| \times 100 \qquad [56]$$

where the experimental turbidimetry dataset was obtained from measurements performed either in a cuvette or in a 96 well plate.

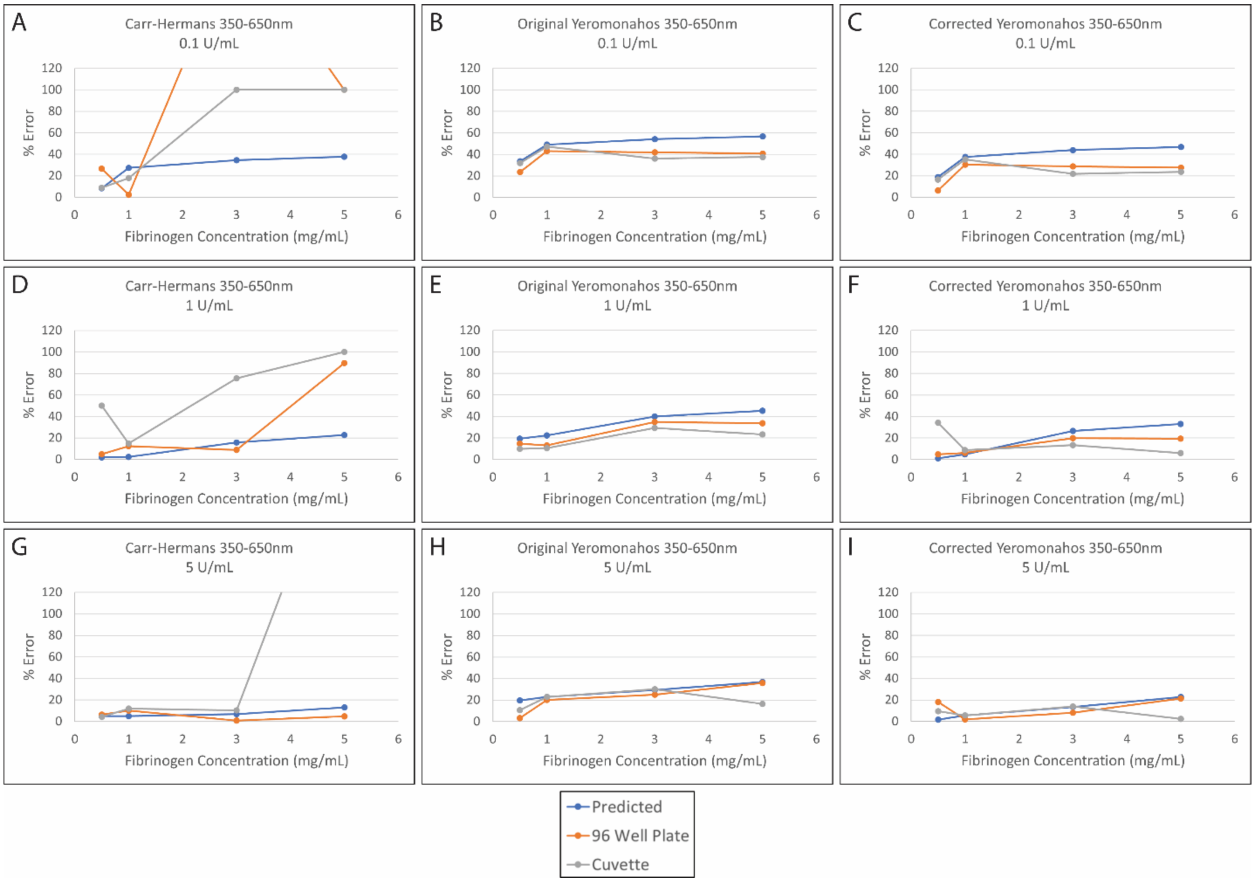

Fig. 31: Percent error in the diameter obtained from each turbidimetric approach compared to from SEM with measurements performed in a 96 well plate (orange) and in a cuvette (gray) and predicted percent error based on simulations of turbidimetric approach versus full light scattering theory (blue) (wavelength range of 350-650 nm; n and dn/dc wavelength corrected).

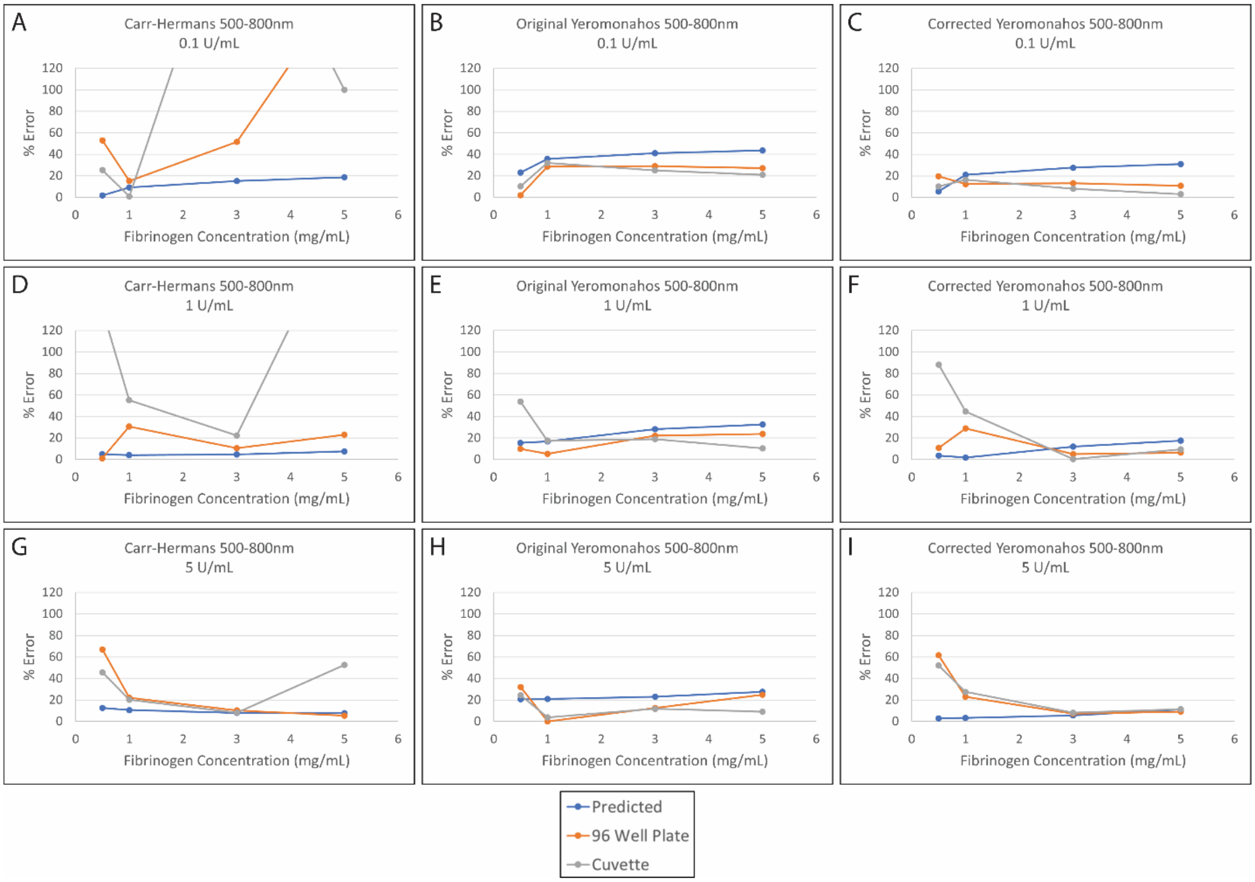

Fig. 32: Percent error in the diameter obtained from each turbidimetric approach compared to from SEM with measurements performed in a 96 well plate (orange) and in a cuvette (gray) and predicted percent error based on simulations of turbidimetric approach versus full light scattering theory (blue) (wavelength range of 500-800 nm; n and dn/dc wavelength corrected).

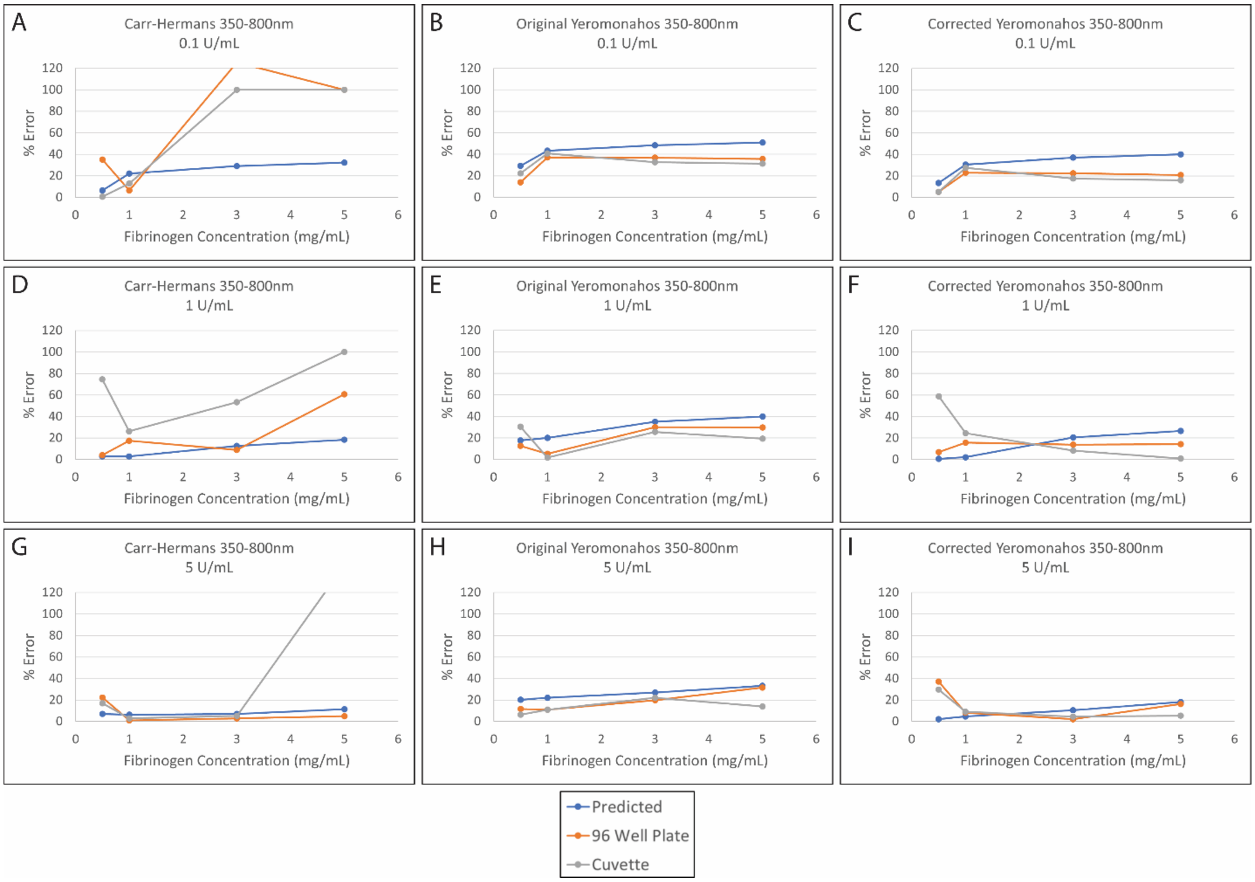

Fig. 33: Percent error in the diameter obtained from each turbidimetric approach compared to from SEM with measurements performed in a 96 well plate (orange) and in a cuvette (gray) and predicted percent error based on simulations of turbidimetric approach versus full light scattering theory (blue) (wavelength range of 350-800 nm; n and dn/dc wavelength corrected).

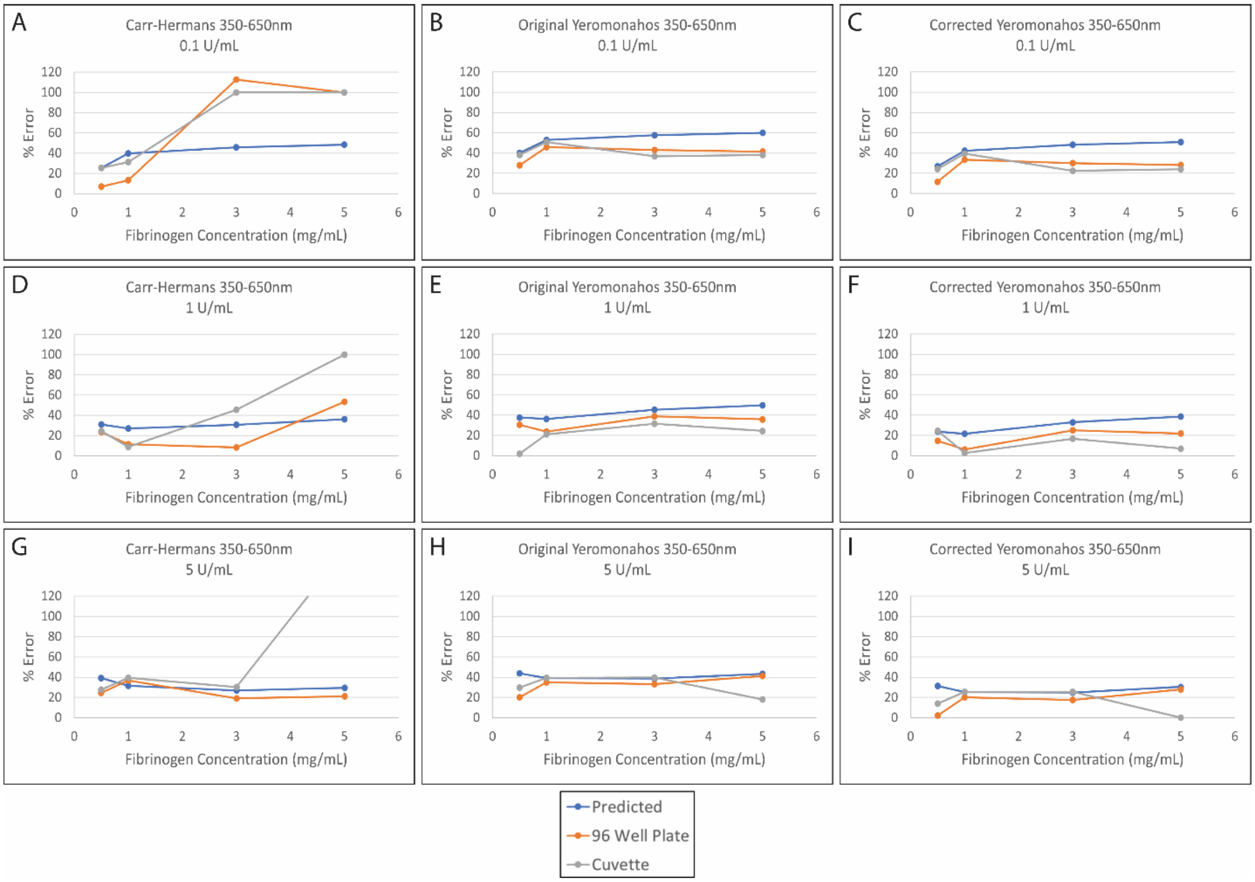

Fig. 34: Percent error in the diameter obtained from each turbidimetric approach compared to from SEM with measurements performed in a 96 well plate (orange) and in a cuvette (gray) and predicted percent error based on simulations of turbidimetric approach versus full light scattering theory (blue) (wavelength range of 350-650 nm; constant n and dn/dc).

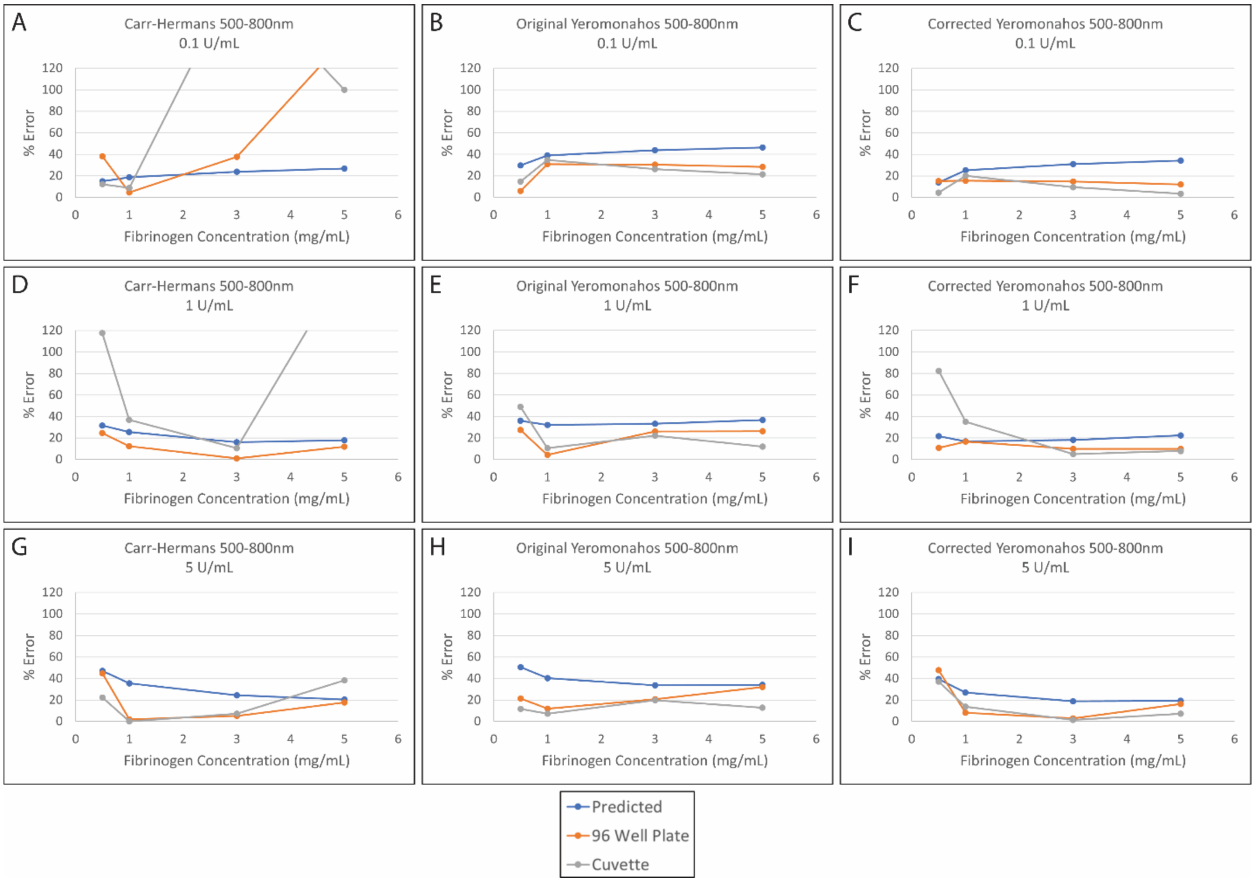

Fig. 35: Percent error in the diameter obtained from each turbidimetric approach compared to from SEM with measurements performed in a 96 well plate (orange) and in a cuvette (gray) and predicted percent error based on simulations of turbidimetric approach versus full light scattering theory (blue) (wavelength range of 500-800 nm; constant n and dn/dc).

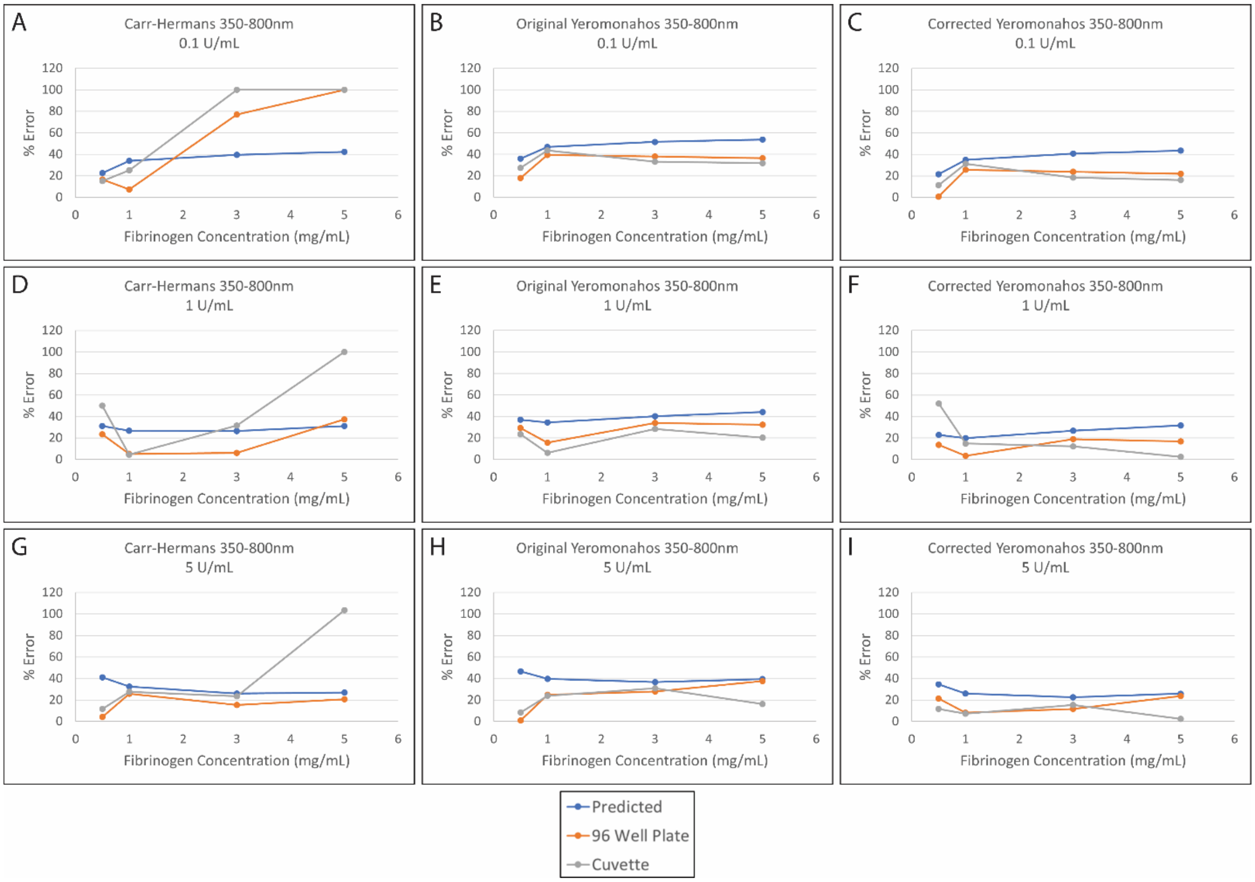

Fig. 36: Percent error in the diameter obtained from each turbidimetric approach compared to from SEM with measurements performed in a 96 well plate (orange) and in a cuvette (gray) and predicted percent error based on simulations of turbidimetric approach versus full light scattering theory (blue) (wavelength range of 350-800 nm; constant n and dn/dc).

As seen, the predicted and experimental percent error were usually very similar for the Original and Corrected Yeromonahos approach, but deviated quite a bit for the Carr-Hermans approach. Furthermore, it appears that the experimental error is typically closer to the predicted error when the wavelength dependence of n and dn/dc is accounted for, and when using a 96 well plate, rather than a cuvette to take measurements. This is confirmed quantitatively in Table 10. For almost all of the approaches, there is a lower percentage of clot conditions in which the predicted and experimental error were within 10-20% of one another when using constant values of n and dn/dc, rather than when using wavelength corrected values of n and dn/dc. Furthermore, for all three approaches, there are fewer clot conditions where the predicted and experimental error were within 10-20% of one another when using a cuvette versus a 96 well plate.

A

	Within 20%	Within 10%
Carr-Hermans	63.9%	47.2%
Original Yeromonahos	94.4%	50%
Corrected Yeromonahos	88.9%	52.8%

B

	Within 20%	Within 10%
Carr-Hermans	41.7%	33.3%
Original Yeromonahos	83.3%	38.9%
Corrected Yeromonahos	58.3%	41.7%

C

	Within 20%	Within 10%
Carr-Hermans	63.9%	36.1%
Original Yeromonahos	83.3%	41.7%
Corrected Yeromonahos	86.1%	44.4%

D

	Within 20%	Within 10%
Carr-Hermans	55.6%	36.1%
Original Yeromonahos	55.6%	22.2%
Corrected Yeromonahos	63.9%	33.3%

Table 10: Percent of clot conditions in which the predicted percent error and experimental percent error were within 20% (middle column) or 10% (right column) of one another for A) measurements taken in a 96 well plate with n and dn/dc wavelength corrected, B) measurements taken in a cuvette with n and dn/dc wavelength corrected, C) measurements taken in a 96 well plate with constant n and dn/dc, D) measurements taken in a cuvette with constant n and dn/dc.

The reasoning for the increased percent error in measurements performed in a cuvette rather than in a 96 well plate is likely due to there being more multiple scattering in the cuvette, since the light has to travel through a thicker section of sample. Since the simulated error did not account for multiple scattering, this would lead to further deviation between the predicted and experimental error. This is supported by Figures 37-38, which show the difference between the predicted and experimental percent errors versus the average diameter according to SEM. As seen, the error in the diameter obtained when using a cuvette (gray datapoints) typically differ from the predicted error more than the measurements performed in a 96 well plate (orange datapoints), especially as the diameter increases. This supports the idea that the discrepancy is due to multiple scattering because there would be increased multiple scattering as the diameter of the fibers increases.

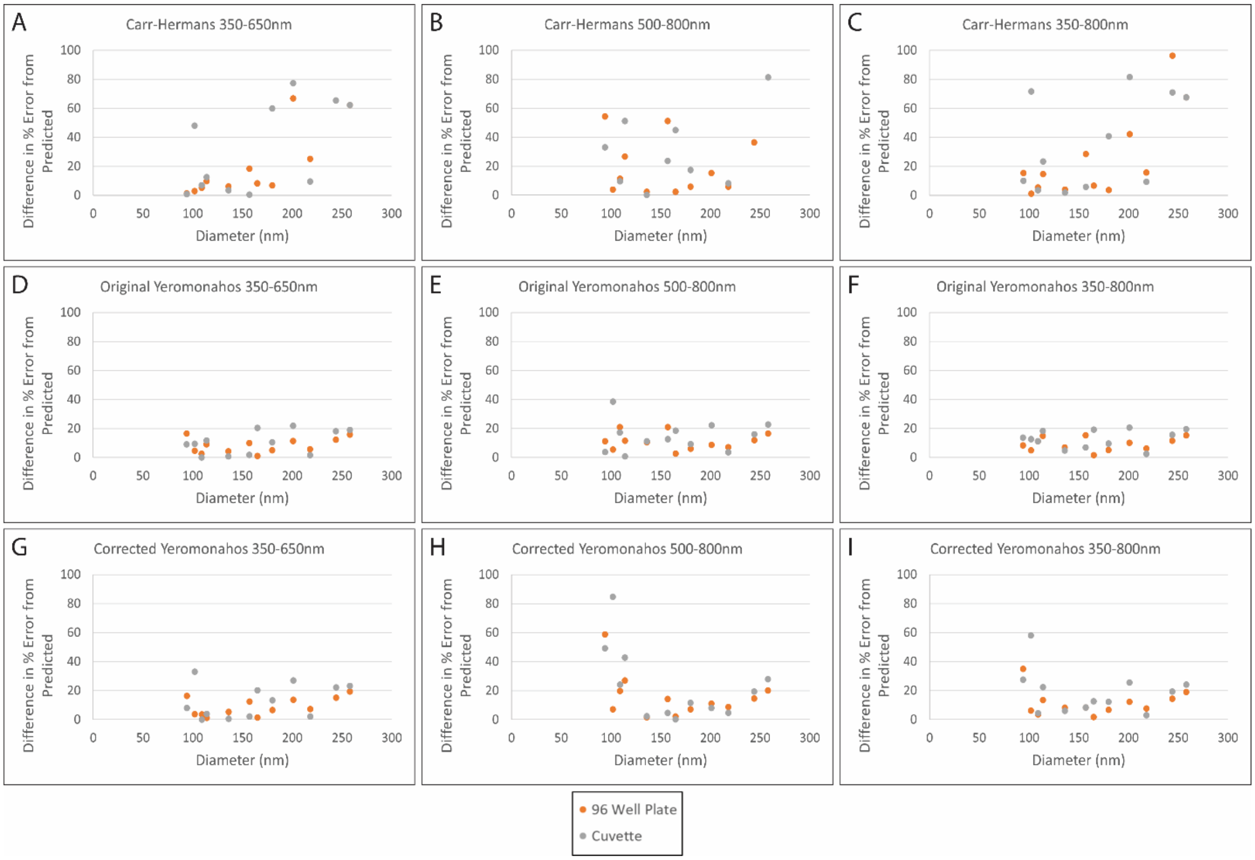

Fig. 37: Difference in predicted percent error based on simulated comparison to light scattering theory and experimental percent error between diameters obtained from turbidimetry and those obtained from SEM imaging (n and dn/dc wavelength corrected).

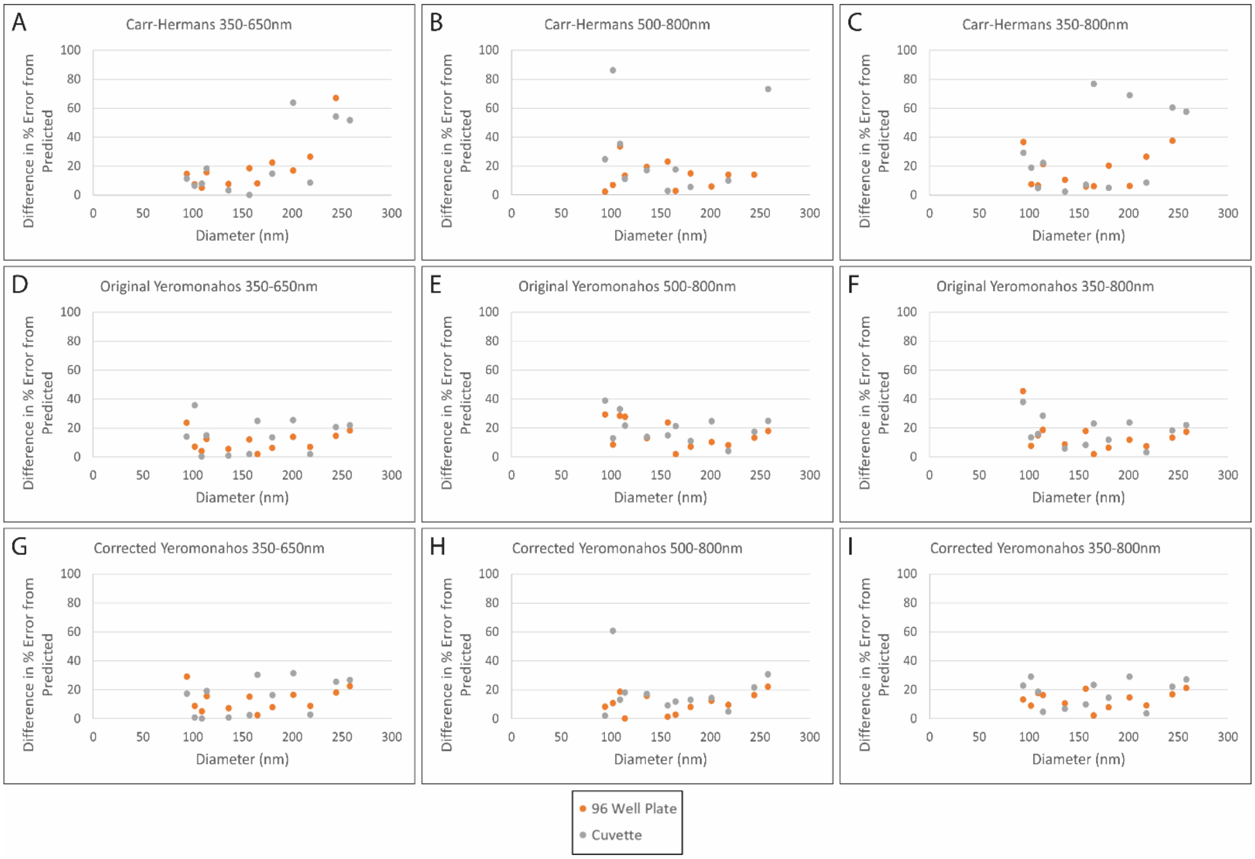

Fig. 38: Difference in predicted percent error based on simulated comparison to light scattering theory and experimental percent error between diameters obtained from turbidimetry and those obtained from SEM imaging (constant n and dn/dc).

Since the percent error in the diameter value involves taking the absolute value of the difference in the diameters, it does not indicate whether the diameter is being overestimated or underestimated. Therefore, in order to determine if the turbidimetric diameters were overestimates or underestimates compared to those from SEM, and whether that matched what was predicted from the simulations, we plotted the actual diameter values for the results obtained in a 96 well plate, using a wavelength range of 500-800 nm, with n and dn/dc wavelength corrected, as shown in Figure 39. As seen, for the Carr-Hermans approach, the experimentally obtained diameter values were almost always overestimates, while the simulations predicted that they would be underestimates. For the Original Yeromonahos approach, both the experimental turbidimetry diameters and the simulated turbidimetry diameters were underestimating the diameter compared to what was found with SEM; however, the experimental turbidimetry error underestimated it by less than the simulations did. For the Corrected Yeromonahos approach, for small diameters (157 nm and less), the experimental turbidimetry diameters were overestimates, while the simulations predicted that the diameter would be underestimated, while for diameters of 165 nm and larger, both the experimental turbidimetry diameters and the predicted turbidimetry diameters were underestimates, although the experimentally obtained diameters were closer than what was expected based on the simulations.

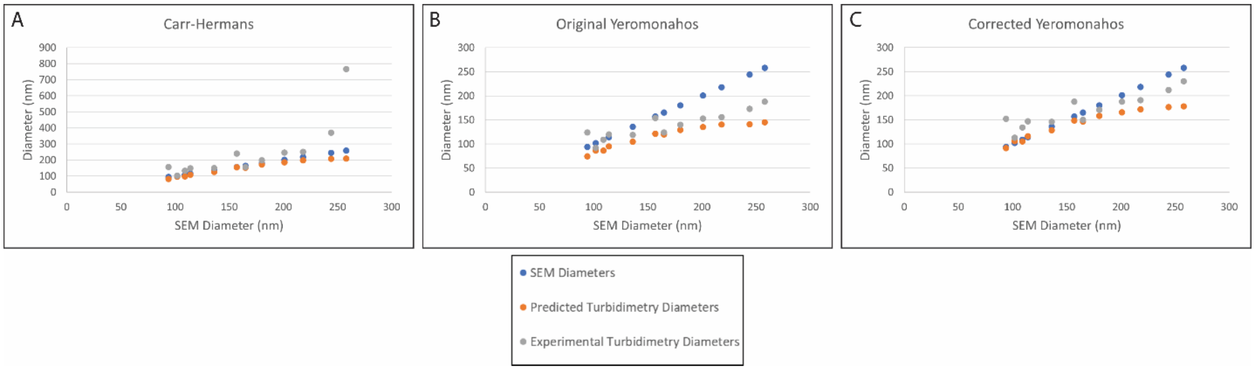

Fig. 39: Diameter values obtained from SEM imaging (blue), and turbidimetric diameters predicted from the simulations (orange), and found experimentally (blue), using the A) Carr-Hermans approach, B) Original Yeromonahos approach, and C) Corrected Yeromonahos approach (wavelength range of 500-800 nm, n and dn/dc wavelength corrected, measurements performed in 96-well plate).

It can also be seen from Figure 39 that the predicted turbidimetry diameters and experimental turbidimetry diameters differ more from one another as the diameter increases for all three approaches. To investigate the reasoning for this, we compared turbidimetry datasets from full light scattering theory to those found experimentally for the same fiber diameters and lengths for four investigated concentrations. The turbidimetry datasets can be seen in Figure 40. As seen, the experimental turbidimetry values were always larger than those predicted from full light scattering theory. Furthermore, while the simulated and experimental datasets contain similar curvatures for the smaller fiber diameters, the curvature changes drastically for the experimental datasets as the diameter increases. We made a log-log plot of the turbidity versus wavelength and used the slope to determine the power relation between the two parameters. An example of one of these log-log plots and the powers for each of the chosen samples are plotted in Figure 41 for both the simulated and experimental datasets at the four investigated concentrations. As seen, the power relationship between turbidity and wavelength is very similar for the simulated dataset and the experimental dataset for diameters of 109 and 165 nm, but increases drastically for the experimental dataset for larger diameters, while it does not for the simulated dataset. Therefore, full light scattering theory did not accurately represent turbidimetric data for larger diameters, leading to the discrepancy between the predicted and experimental diameters, as shown in Figure 39.

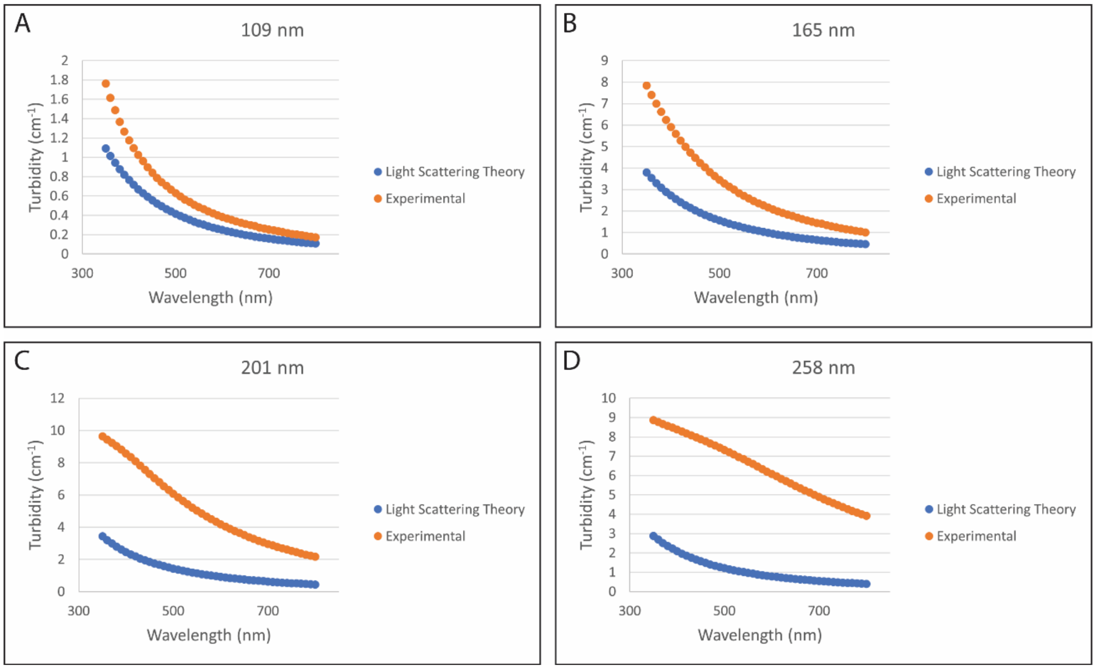

Fig. 40: Simulated turbidimetry datasets from full light scattering theory (Equations 7-9) compared to those found experimentally for fibers with average diameters of A) 109 nm, B) 165 nm, C) 201 nm, and D) 258 nm (according to SEM) (using wavelength corrected n and dn/dc, for wavelengths of 350-800 nm).

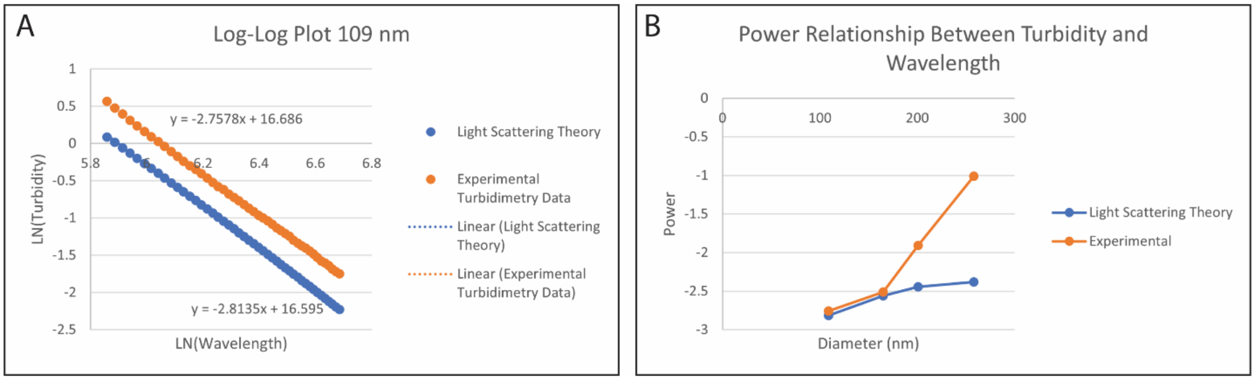

Fig. 41: A) An example of a log-log plot for determining the power relationship between turbidity and wavelength. B) Power relationship between the turbidity and wavelength for average diameters of 109, 165, 201, and 258 nm (according to SEM) for simulated turbidimetry datasets, as well as experimental datasets (with wavelength corrected n and dn/dc).

Conclusion

The predicted diameters based on the simulations comparing the turbidimetric approaches to full light scattering theory differed in many ways from what occurred experimentally. The simulations predicted that the turbidimetric approaches would mostly underestimate the fiber diameter; however, the Carr-Hermans approach almost always overestimated the diameter, and the Corrected Yeromonahos approach overestimated the diameter for thin fibers compared to the values from SEM.

However, despite this difference in the predicted over- or under-estimation of the diameter, the actual diameter values agree reasonably well between what was predicted and what was obtained experimentally for fibers below ~ 165 nm, with the differences between the predicted and experimentally obtained diameters differing more as the diameter increases (see Figure 39). This is due to full light scattering theory and experimental turbidimetry datasets containing different power relationships between turbidity and wavelength as the fiber diameter increases, causing the simulations to be less accurate for all three turbidimetric approaches at large diameter values.

Despite these differences, the predicted percent error based on the simulations comparing the turbidimetric approaches to full light scattering theory were reasonably similar to the experimental percent error between the diameters obtained using the turbidimetric fitting approaches and those from SEM for most clot conditions when using the Original Yeromonahos approach and Corrected Yeromonahos approach. It better matched the experimental error when using a 96 well plate for measurements, due to there being less multiple scattering with the light needing to travel through a smaller section of sample in the 96 well plates than it does in a cuvette, as well as the other cuvette reading limitations discussed in Chapter 3. It furthermore matched the experimental error when using wavelength corrected values of n and dn/dc rather than using constants for those terms. The predicted percent error did not match the experimental percent error as well when using the Carr-Hermans approach, especially as the diameter increased.

Based on these results, even though the simulations predicted that the Carr-Hermans approach is the most reliable of the three (see Chapter 2), the error for the Carr-Hermans approach does not match well with what actually occurs experimentally, with the diameter usually being overestimated instead of underestimated as predicted, resulting in the approach not being as accurate as predicted based on the simulations. Since the simulations found that the Corrected Yeromonahos approach also works well for most investigated fiber conditions, even though that equation was obtained erroneously, it is actually the most reliable of the turbidimetric fitting approaches over the largest range of clot conditions experimentally and matches well with the simulated error, particularly for diameter values of 165 nm and larger.

CHAPTER 5: LIMITATIONS IN TURBIDIMETRIC ANALYSIS OF FIBERS

Limitations of Light Scattering Theory

There are several possible limitations in the use of turbidimetry for determining fibrin fiber structural information. There are limitations originating in the turbidimetric fitting equations themselves, as well as in the experimental methods for determining turbidimetry, which should be considered when analyzing a fibrin network.

The first limitation is that that the equations assume the fibers are Rayleigh-Gans-Debye scatterers. In order to be considered Rayleigh-Gans-Debye scatterers, the ratio of the index of refraction of the fibrinogen (n_p) to the index of refraction of the surrounding medium (n_s) should be close to one. Using the value of 1.6 for the index of refraction of most proteins [65], and the refractive index of HBS buffer (150 mM sodium chloride and 20 mM HEPES, pH 7.4), n_p/n_s is 1.196 ± 0.002 for the wavelength range being investigated (350-800 nm). Therefore, the criterion of being close to 1 is not fully met.

Additionally, the full light scattering theory equations and all of the linear fitting approaches use the form factor for a thin rod. As the wavelength of light approaches the diameter, the justifications for using the thin rod form factor begin to weaken. We furthermore found that the power relationship between turbidity and wavelength expressed with the full light scattering theory equation differs more from what actually occurs experimentally as the diameter value increases. Therefore, caution should be used if analyzing fibers with large diameters.

Furthermore, the Carr-Hermans, Original Yeromonahos, and Corrected Yeromonahos approaches assume that the fibers do not interact with one another, meaning the structure factor in the full light scattering theory equation would be 1. Since the fibers do interact, coming together at junctions to form the three-dimensional network, this could cause full light scattering theory to underestimate the turbidity, and thus underestimate the fiber diameter.

Experimental Limitations

Not only are there limitations in the theory behind the turbidimetric approaches, but there are also potential limitations in the application of the theory to experimental data. One possible limitation in using turbidimetry for analyzing clots is that the light scattering theory equations (Equations 7-9) assume that the fibers are dilute, and they therefore do not account for multiple scattering effects. The effects of multiple scattering were investigated by García et al. [31] who looked at the effect of changing optical pathlength on the estimated number of protofibrils per fiber. They found that the number of protofibrils is independent of the optical pathlength, which suggests that multiple scattering effects are insignificant. However, they only checked this for fibrinogen concentrations of 1 mg/mL and 3 mg/mL, with 0.1 NIH-U/mL thrombin, and we only compared changing volumes for 0.5 mg/mL fibrinogen with 0.1 NIH-U/mL thrombin, so this may not be the case if performing light scattering measurements on higher concentrations. Unfortunately, our experiment using covers to block multiple scattered light was unsuccessful, and therefore further analysis should be done to determine the effect of multiple scattering. However, our experimental results do not show any significant increases in error in the obtained diameters with large fibrinogen concentrations, which should result in thick fibers, or those with large thrombin concentrations, which should result in densely packed fibers, therefore implying that there is not significant multiple scattering for the investigated concentrations.

Furthermore, it is assumed by the equations that the fibers are homogeneous cylinders. However, the fibrin network can consist of fibers of varying lengths and diameters, as well as fibers that are not uniform in diameter along the length of the fiber. Since the light scattering equation uses a form factor that is averaged over all directions, the size parameters are also volume averaged [20], and thus, this polydispersity is not accounted for. Therefore, it is important to keep in mind that the obtained diameter value from the turbidimetric approaches could be skewed by fibers with thick diameters, leading to an overestimation of the diameter. There can also be spatial heterogeneity present in the clot that is not accounted for, particularly if there are aggregates present. However, it has been found that there are stock solutions that do not contain aggregates and that create spatially uniform clots [31], so this problem can be largely avoided. Ferri et al. [18] also discussed the shortcomings of these assumptions, pointing out that although the single fibers might meet the criterion of being straight and randomly oriented, when the entire clot is considered, these assumptions may not be met, resulting in inaccuracies in the investigated turbidimetric approaches. In addition, recent work shows that the fibers themselves have non-uniform internal structures [66], which will cause additional deviations.

Despite these limitations, the turbidimetric approaches are still able to provide reasonable values for the diameter and mass-length ratio, as found through previous comparisons with results from small-angle x-ray scattering [31], dynamic light scattering [20], and permeability measurements [67], as well as our experimental comparisons with SEM and STORM imaging. However, it is necessary to be sure the appropriate approach is being used for turbidimetric analysis, and that the correct conditions are being utilized. This includes using the correct wavelength range for measurements (500-800 nm), accounting for the wavelength dependence of n and dn/dc in analysis, using a 96 well plate for high fibrinogen concentrations, etc.

Furthermore, we also found that turbidimetry is unreliable for fibers of very thin diameters (less than approximately 100 nm), so an alternative method should be used if analyzing clots composed of very thin fibers, such as those created at low fibrinogen concentrations or with high thrombin concentrations. Alternative methods could include SEM, STORM, small angle x-ray scattering, and small angle neutron scattering.

CHAPTER 6: SUMMARY AND FUTURE DIRECTIONS

Summary

Previously, different methods have been used for studying the structure of fibrin among different labs, resulting in discrepancies in how different parameters impact the structure of the fibers. With there being little to no comparison of these different methods, relating results from different studies was difficult, if not impossible. Furthermore, there are four different equations commonly utilized for fitting turbidimetry datasets to determine fibrin structure, but a deep investigation into which equation is the most accurate and under what clot conditions they are able to provide reliable structural information had not been performed. There was also disagreement on what wavelength range is best for taking turbidimetry measurements, as well as if it is necessary to account for the wavelength dependence of the refractive index and specific refractive index increment in the fitting.

In order to address these challenges, we have provided the first comparison of the fibrin fiber diameter obtained using SEM, STORM, and turbidimetry across a range of physiologically relevant fibrinogen and thrombin concentrations. We have furthermore provided the first comprehensive analysis of the four different commonly utilized turbidimetric fitting approaches through comparison with both full light scattering theory and through comparison with secondary experimental techniques. The results of this work provide a step toward standardization in the methodology for determining fibrin fiber diameter, which will allow for direct comparison of results from different studies. It also establishes the limitations of the different turbidimetric fitting approaches, as well as the necessary experimental settings to use in order to obtain accurate structural information, which could be applied to other studies utilizing turbidimetry to determine the structure of rod-like particles. Table 11 shows the state of the field on what information related to the determination of fibrin fiber diameters was previously unknown and debated (red X's) compared to what has now been validated by this work (black X's).

	Validated	Unknown	Debated
Effect of fibrinogen concentration	X		X
Effect of thrombin concentration	X		
SEM vs. STORM diameters	X	X	
Which turbidimetric approach is the most accurate	X		X
Turbidimetric approach limitations (clot conditions)	X	X	
Wavelength-dependence corrected vs. constant index of refraction and specific refractive index increment	X		X
Best wavelength range to use for measurements	X		X

Table 11: The information that was previously unknown or debated (red X's) related to the determination of fibrin fiber diameters, and what has been validated by this work (black X's).

We found with SEM and STORM that the fiber diameter increases with increasing fibrinogen concentration and decreases with increasing thrombin concentration. The same trend was also largely seen with the turbidimetric fitting approaches.

Based on our comparison between the diameters obtained with SEM and STORM imaging, we have determined that there is not a significant impact on the fibrin structure from the drying and fixation steps required for SEM sample preparation.

Additionally, we have determined that the Corrected Yeromonahos approach is the most versatile of the turbidimetric approaches, and we created a post hoc adjustment equation that can be applied to the diameters obtained from the Corrected Yeromonahos approach in order to make them even more accurate.

Based on both the simulated results and the experimental results, we determined that turbidimetry is unreliable for analysis of fibers thinner than ~ 100 nm in diameter, and we established several possible limitations, both experimentally and in the fitting equations, for analysis of fibers with diameters close to the wavelengths being used for measurements. Therefore, turbidimetry can be used for accurately determining fibrin fiber structure but should only be used for a certain range of experimental conditions.

Our results show that as long as the right experimental conditions are used, there can be good agreement between diameter values obtained using SEM imaging, STORM imaging, and turbidimetry. Specifically, we recommend that it become standard practice to use 1 mg/mL fibrinogen and 0.1 NIH-U/mL thrombin for studies analyzing the structure of fibrin made from purified fibrinogen, as the diameter values obtained with the three methods for that concentration differ by less than 3%, and it is a concentration using reasonably low amounts of sample. This agreement requires that in determining the fiber diameter with turbidimetry, a wavelength range of 500-800 nm is used, the wavelength dependence of the refractive index and specific refractive index increment are accounted for, and that our post hoc adjustment is applied.

Future Directions

Further Analysis of Turbidimetric Fitting Approaches Under Varying Conditions

While this work has focused mostly on determining the accuracy of using turbidimetry for determining fibrin fiber diameter, turbidimetry can also be used for determining fiber mass-length ratio, as briefly touched on in Chapter 2. The mass-length ratio can also be used for determining the average number of protofibrils per cross section, which has been patented for use in predicting bleeding risks clinically [35]. The mass-length ratio and diameter can also be used together to determine the fiber density. However, the determination of the mass-length ratio and the density face the same problem of not being confirmed over a range of physiological conditions through comparison with other techniques. Therefore, one potential extension of this work is to experimentally determine the mass-length ratio using each of the turbidimetric fitting approaches to determine under what conditions they are each able to provide accurate measurements. These results could be compared to those obtained using permeability, and could also be compared to our simulated results of Chapter 2.

Furthermore, this work only investigated three wavelength ranges: 350-650 nm, 500-800 nm, and 350-800 nm. We chose these wavelengths due to their use in the investigated turbidimetric fitting approach papers. However, other wavelength ranges could be investigated to determine what wavelength range is the best to use, as well as the best number of datapoints to take. While we took measurements every 10 nm, it is possible that we could have gotten just as accurate of results only taking measurements every 50 nm, which would speed up the analysis process, or it is possible that we would have had more accurate values had we taken more measurements.

We also only investigated the accuracy of the different turbidimetric fitting approaches with changing fibrinogen and thrombin concentrations. However, there are several other experimental conditions which impact fibrin structure, such as pH, calcium, and the addition of other proteins. It is possible that the turbidimetric fitting approaches fail above/below certain concentrations of these other factors.

Comparison of Turbidimetry to Static Light Scattering and Dynamic Light Scattering

In addition to turbidimetry, static light scattering and dynamic light scattering are other experimental techniques which use light scattering information to determine structural properties of a sample. While turbidimetry utilizes a single angle, but multiple wavelengths, static light scattering measures the intensity of light scattered at several angles using just one wavelength. This allows for determination of the radius of gyration (R_g), which can then be used to determine the fiber diameter, which for a cylinder is related by [16]:

$$R_g = \sqrt{\frac{r^2}{2} + \frac{L^2}{12}} \qquad [57]$$

where r is the fiber radius and L is the fiber length. However, this assumes that the fibers are non-interacting cylinders freely floating in a solution, and thus may not be completely accurate for our case of a three-dimensional gel network.

Dynamic light scattering, which utilizes one angle and one wavelength, but takes measurements over several time points, also uses light scattering to determine structural information. This allows for the determination of the diffusion coefficient (D), which can then be used for determining the hydrodynamic radius (R_h) with the equation [16]:

$$R_h = \frac{k_B T_s}{6\pi \nu D} \qquad [58]$$

where k_B is Boltzmann's constant, T_s is the absolute temperature of the suspension, and ν is the viscosity of the liquid. The hydrodynamic radius is the radius of a sphere that would have that diffusion coefficient. While the hydrodynamic radius cannot be directly compared to the diameter values obtained using turbidimetry or static light scattering, it could be used as a secondary method for studying trends in how fiber structure changes under varying conditions.

Further Analysis Using Light Sheet Microscopy

While this work only used the light sheet microscopy images in order to analyze if the fibers toward the bottom of a sample are being compressed, there are several other possible questions that could be answered using the acquired videos and images. There are very few devices capable of capturing the polymerization process of fibrin networks due to the speed in which it occurs and the small diameter of the fibers, particularly during the process of formation. To our knowledge, the only published works visualizing the fibrin polymerization process were performed with spinning-disk confocal microscopy [68]. Spinning-disk confocal microscopy utilizes hundreds of pinholes arranged in a spiral that spins to scan images much faster than typical laser scanning confocal microscopes, which only use a single pinhole. However, it is still using point scanning (just with more than one point), and thus has large amounts of photodamage. It can also have less rejection of out-of-focus light than a laser scanning confocal microscope due to light coming from adjacent pinholes. Light sheet microscopy, on the other hand, has the illumination source and detector placed orthogonally to one another and projects a thin light sheet on the sample, allowing for only a single focal plane to be illuminated at a time. This allows for imaging that is one hundred to a thousand times faster than confocal microscopy, with significantly reduced photobleaching [69]. With its improvements over spinning-disk confocal microscopy, our light sheet microscopy videos of fibrin polymerization could provide new information about the polymerization process. As shown by three images taken from the time series videos provided in Figure 42, it captures the entire polymerization process, from the beginning of clot formation until the clot is completely formed. They could be used for analyzing the rates of fiber growth and how/when branchpoints are created. Light sheet microscopy could also potentially be used for studying fibrin lysis, although we did not obtain any videos of fiber lysis for this work.

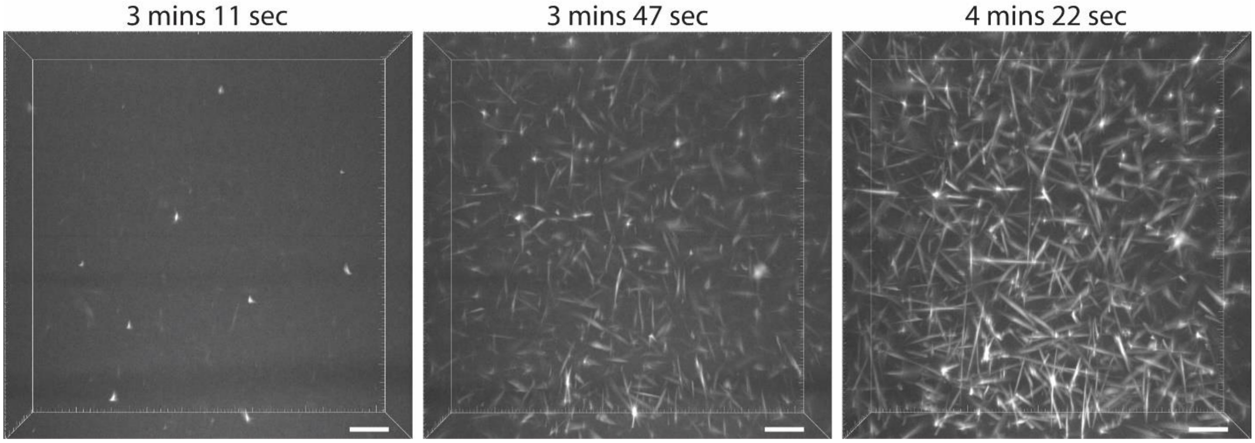

Fig. 42: Three time points taken from one of the light sheet microscopy time series videos capturing the polymerization of a clot containing 3 mg/mL fibrinogen and 0.1 NIH-U/mL thrombin (scale bar 20 µm).

REFERENCES

[1] Belcher HA, Litwa K, Guthold M, Hudson NE. The applicability of current turbidimetric approaches for analyzing fibrin fibers and other filamentous networks. Biomolecules. 2022;12(6):807. https://doi.org/10.3390/biom12060807.

[2] Weisel JW. Fibrinogen and Fibrin. Adv Protein Chem. 2005; 70:247-299. https://doi.org/10.1016/S0065-323370008-5.

[3] Hudson NE. Biophysical mechanisms mediating fibrin fiber lysis. Hindawi Biomed Research Int. 2017. https://doi.org/10.1155/2017/2748340.

[4] Dunn EJ, Ariëns RAS, Grant PJ. The influence of type 2 diabetes on fibrin structure and function. Diabetologia. 2005; 48:1198-1206. https://doi.org/10.1007/s00125-005-1742-2.

[5] Siniarski A, Baker SR, Duval C, Malinowski KP, Gajos G, Nessler J, Ariëns RAS. Quantitative analysis of clot density, fibrin fiber radius, and protofibril packing in acute phase myocardial infarction. Thromb Res. 2021; 205:110-19. https://doi.org/10.1016/j.thromres.2021.06.024.

[6] Undas A, Slowik A, Wolkow P, Szczudlik A, Tracz W. Fibrin clot properties in acute ischemic stroke: relation to neurological deficit. Thromb Res. 2010; 125(4):357-61. https://doi.org/10.1016/j.thromres.2009.11.013.

[7] Undas A, Ariëns RAS. Fibrin clot structure and function: a role in the pathophysiology of arterial and venous thromboembolic diseases. Arterioscler Thromb Vas Biol. 2011; 31:88-99. https://doi.org/10.1161/ATVBAHA.111.230631.

[8] de Vries JJ, Visser C, Geers L, Slotman JA, van Kleef ND, Maas C, Bax HI, Miedema JR, van Gorp ECM, Goeijenbier M, van den Akker JPC, Endeman H, Rijken DC, Kruip MJHA, de Maat MPM. Altered fibrin network structure and fibrinolysis in intensitve care unit patients with COVID-19, not entirely explaining the increased risk of thrombosis. J Thromb Haemost. 2022; 20(6):1412-20. https://doi.org/10.1111/jth.15708.

[9] Wolberg AS. Plasma and cellular contributions to fibrin network formation, structure and stability. Haemophilia. 2010; 16:7-12. https://doi.org/10.1111/j.1365-2516.2010.02253.x.

[10] Zimm BH, Dandliker WB. Theory or light scattering and refractive index of solutions of large colloidal particles. J Phys Chem. 1954; 58:644-648. https://doi.org/10.1021/j150518a012.

[11] Pieters M, Guthold M, Nunes CM, de Lange Z. Interpretation and validation of maximum absorbance data obtained from turbidimetry analysis of plasma clots. Thromb Haemost. 2020; 120:44-54. https://doi.org/10.1055/s-0039-1698460.

[12] Dassi C, Sevve L, García X, Bigo E, Marlu R, Caton F, Polack B. Fibrinography: a multiwavelength light-scattering assay of fibrin structure. HemaSphere. 2019; 3:e166. https://doi.org/10.1097/HS9. 0000000000000166.

[13] Kurniawan NA, Grimbergen J, Koopman J, Koenderink GH. Factor XIII stiffens fibrin clots by causing fiber compaction. J Thromb Haemost. 2014; 12:1687-1696. https://doi.org/10.1111.jth.12705.

[14] IUPAC. Compendium of Chemical Terminology, 2nd ed.; (the "Gold Book"). McNaught AD, Wilkinson A. Blackwell Scientific Publications. Oxford, UK. 1997. https://doi.org/10.1351/goldbook.R05159.

[15] Chapter 7: Light Scattering. n.d. https://www.eng.uc.edu/~beaucag/Classes/Properties/ZimmIASLightScat.pdf.

[16] Øgendal LH. Light scattering demystified: theory and practice. University of Copenhagen. København, Denmark, 2019.

[17] Kerker M. The scattering of light and other electromagnetic radiation; Academic Press. Cambridge, MA, USA. 1969. https://doi.org/10.1016/C2013-0-06195-6.

[18] Ferri F, Calegari GR, Molteni M, Cardinali B, Magatti D, Rocco M. Size and density of fibers in fibrin and other filamentous networks from turbidimetry: beyond a revisited Carr-Hermans method, accounting for fractality and porosity. Macromolecules. 2015; 48(15):5423-32. https://doi.org/10.1021/acs.macromol.5b00893.

[19] Carr ME, Hermans J. Size and density of fibrin fibers from turbidity. Macromolecules. 1978; 11(1):46-50. https://doi.org/10.1021/ma60061a009.

[20] Yeromonahos C, Polack B, Caton F. Nanostructure of the fibrin clot. Biophys J. 2010; 99(7):2018-27. https://doi.org/10.1016/j.bpj.2010.04.059.

[21] Yeromonahos C. Nanostructure des fibres de fibrine. PhD Thesis Universite de Grenoble. 2011. HAL Id:tel-00639435.

[22] Ferry JD, Morrison PR. Preparation and properties of serum and plasma proteins. VIII. The conversion of human fibrinogen to fibrin under various conditions. J Am Chem Soc. 1947; 69:388-400. https://doi.org/10.1021/ja01194a066.

[23] Casassa EF. Light scattering from very long rod-like particles and an application to polymerized fibrinogen. J Chem Phys. 1955; 23:596-597. https://doi.org/10.1063/1.1742048.

[24] Marguerie G, Pouit L, Suscillon M. Macromolecular associations in dilute solutions of activated fibrinogen. Thromb Res. 1973; 3:675-689. https://doi.org/10.1016/0049-384890015-7.

[25] Philo J. SEDNTERP. Version 3.0.3. 2021. http://www.jphilo.mailway.com/download.htm.

[26] Schuck P. SEDFIT. Version 16.1c. National Institutes of Health. Betesda, MD, USA, 2018.

[27] Schuck P. Size-distribution analysis of macromolecules by sedimentation velocity ultracentrifugation and Lamm equation modeling. Biophys J. 2000; 78:1606-1619. https://doi.org/10.1016/S0006-349576713-0.

[28] Locke M, Longstaff C. Extracellular histones inhibit fibrinolysis through noncovalent and covalent interactions with fibrin. Thromb Haemost. 2021; 121:464-476. https://doi.org/10.1055/s-0040-1718760.

[29] Baker SR, Zabczyk M, Macrae FL, Duval C, Undas A, Ariëns RA. Recurrent venous thromboembolism patients form clots with lower elastic modulus than those formed by patients with non-recurrent disease. J Thromb Haemost. 2019; 17:618-626. https://doi.org/10.1111/jth.14402.

[30] Staneva R, Burla F, Koenderink G, Descroix S, Vignjevic DM, Attieh Y, Verhulsel M. A new biomimetic assay reveals the temporal role of matrix stiffening in cancer cell invasion. Mol Biol Cell. 2018; 29:2979-2988. https://doi.org/10.1091/mbc.E18-01-0068.

[31] García X, Seyve L, Tellier Z, Chevreux G, Bihoreau N, Polack B, Caton F. Aggregates dramatically alter fibrin ultrastructure. Biophys J. 2020; 118(1):172-81. https://doi.org/10.1016/j.bpj.2019.10.034.

[32] Ryan EA, Mockros LF, Weisel JW, Lorand L. Structural origins of fibrin clot rheology. Biophys J. 1999; 77(5):2813-26. https://doi.org/10.1016/S0006-3495(99)77113-4.

[33] Pretorius E, Steyn H, Engelbrecht M, Swanepoel AC, Oberholzer HM. Differences in fibrin fiber diameters in healthy individuals and thromboembolic ischemic stroke patients. Blood Coagul Fibrinolysis. 2011; 22(8):696-700. https://doi.org/10.1097/MBC.0b013e32834bdb32.

[34] Vos BE. Fibrin structure and mechanics: a journey across scales. PhD Thesis Vrije Universiteit Amsterdam. 2018. ISBN:978-94-92323-21-7.

[35] Contant G, Polack B, Caton F, Dassi C. Method for determining the structural profile of a fibrin clot reflecting the stability thereof, in order to predict the risk of bleeding, thrombosis, or rethrombosis. 2017. PCT No: PCT/FR2015/052050.

[36] Sheppard N, Willis HA, Rigg JC. Names, symbols, definitions and units of quantities in optical spectroscopy. Pure Appl Chem. 1985; 57:105-120. https://doi.org/10.1351/pac198557010105.

[37] Lampinen J, Raitio M, Perälä A, Oranen H, Harinen RR. Microplate based pathlength correction method for photometric DNA quantification assay. Tech Rep Thermo Fisher Sci. 2012. https://static.thermoscientific.com/images/D20827~.pdf.

[38] Alharbi I, Algethami A, Almteri T. Management of congenital afibrinogenemia: report of two cases. Clin Med Rev Case Report. 2017; 4(12):196. https://doi.org/10.23937/2378-3656/1410196.

[39] Qiu J, Yu Y, Fu Y, Ye F, Xie X, Lu W. Preoperative plasma fibrinogen, platelet count and prognosis in epithelial ovarian cancer. J Obstet Gynaecol Res. 2012; 38(4):651-57. https://doi.org/10.1111/j.1447-0756.2011.01780.x.

[40] García PS, Ciavatta VT, Fidler JA, Woodbury A, Levy JH, Tyor WR. Concentration-dependent dual role of thrombin in protection of cultured rat cortical neurons. Neurochem Res. 2015; 40:2220-29. https://doi.org/10.1007/s11064-015-1711-1.

[41] Kattula S, Byrnes JR, Martin SM, Holle LA, Cooley BC, Flick MJ, Wolberg AS. Factor XIII in plasma, but not in platelets, mediates red blood cell retention in clots and venous thrombus size in mice. Blood Adv. 2018; 2(1):25-35. https://doi.org/10.1182/bloodadvances.2017011890.

[42] Dvilansky A, Britten AF, Loewy AG. Factor XIII assay by an isotope method. I. Factor XIII (transamidase) in plasma, serum, leucocytes, erythrocytes and platelets and evaluation of screening tests of clot solubility. Br J Haematol. 1970; 18(4):399-410. https://doi.org/10.1111.j.1365-2141.1970.tb01453.x.

[43] Landini G. Fractals in microscopy. J Microscopy. 2011; 241:1-8. https://doi.org/10.1111/j.1365-2818.2010.03454.x.

[44] Münster M, Fabry B. A simplified implementation of the bubble analysis of biopolymer network pores. Biophys J. 2013; 104(12):2774-75. https://doi.org/10.1016/j.bpj.2013.05.016.

[45] Molteni M, Magatti D, Cardinali B, Rocco M, Ferri F. Fast two-dimension bubble analysis of biopolymer filamentous networks pore size from confocal microscopy thin data stacks. Biophys J. 2013; 104(5):1160-69. https://doi.org/10.1016/j.bpj.2013.01.016.

[46] Thompson RE, Larson DR, Webb WW. Precise nanometer localization analysis for individual fluorescent probes. Biophys J. 2002; 82:2775-2783. https://doi.org/10.1016/S0006-349575618-X.

[47] Gersh KC, Edmondson KE, Weisel JW. Flow rate and fibrin fiber alignment. J Thromb Haemost. 2011; 8(12):2826-28. https://doi.org/10.1111/j.1538-7836.2010.04118.x.

[48] Rust MJ, Bates M, Zhuang X. Sub-diffraction-limit imaging by stochastic optical reconstruction microscopy (STORM). Nat Methods. 2006; 3:793-96. https://doi.org/10.1038/nmeth929.

[49] Bates M, Jones SA, Zhuang X. Stochastic optical reconstruction microscopy (STORM): a method for superresolution fluorescence imaging. Cold Spring Harb Protoc. 2013; 6:498. https://doi.org/10.1101/pdb.top075143.

[50] de Vries JJ, Visser C, Geers L, Slotman JA, Endeman H, Kruip MJHA, de Maat, MPM. Does fibrin structure contribute to the increased risk of thrombosis in COVID-19 ICU patients? Blood. 2021; 138:3208. https://doi.org/10.1182/blood-2021-145307.

[51] Zong Y, Pruner I, Antovic A, Taxiarchis A, Vila ZP, Soutari N, Mobarrez F, Chaireti R, Widengren J, Piguet J, Antovic JP. Phosphatidylserine positive microparticles improve hemostasis in in-vitro hemophilia A plasma models. Sci Rep. 2020; 10:7871. https://doi.org/10.1038/s41598-020-64686-x.

[52] Sylman JL, Daalkhaijav U, Zhang Y, Gray EM, Farhang PA, Chu TT, Zilberman-Rudenko J, Puy C, Tucker EI, Smith SA, Morrissey JH, Walker TW, Nan XL, Gruber A, McCarty OJT. Differential roles for the coagulation factors XI and XII in regulating the physical biology of fibrin. Ann Biomed Eng. 2017; 45:1328-40. https://doi.org/10.1007/s10439-016-1771-7.

[53] Becatti M, Mannucci A, Argento FR, Gitto S, Vizzutti F, Marra F, Taddei N, Fiorillo C, Laffi G. Super-resolution microscopy reveals an altered fibrin network in cirrhosis: the key role of oxidative stress in fibrinogen structural modifications. Antioxidants. 2020; 9(8):737. https://doi.org/10.3390/antiox9080737.

[54] Weisel JW, Nagaswami C. Computer modeling of fibrin polymerization kinetics correlated with electron microscope and turbidity observations: clot structure and assembly are kinetically controlled. Biophys J. 1992; 63(1):111-28. https://doi.org/10.1016/S0006-3495(92)81594-1.

[55] Carr ME. Fibrin formed in plasma is composed of fibers more massive than those formed from purified fibrinogen. Thromb Haemost. 1988; 59(3):535-39. https://doi.org/10.1055/s-0038-1647529.

[56] Chiu CL, Hecht V, Duong H, Wu B, Tawil B. Permeability of three-dimensional fibrin constructs corresponds to fibrinogen and thrombin concentrations. Biores Open Access. 2012; 1(1):34-40. https://doi.org/10.1089/biores.2012.0211.

[57] Sabra A, Lawrence MJ, Curtis D, Hawkins K, Williams PR, Evans PA. In vitro clot model to evaluate fibrin-thrombin effects on fractal dimension of incipient blood clot. Clin Hemorheol Microcirc. 2019; 74(2):147-53. https://doi.org/10.3233/CH-190615.

[58] Hazra C, Samanta T, Mahalingam V. A resonance energy transfer approach for the selective detection of aromatic amino acids. J Mater Chem C. 2014; 2:10157-10163. https://doi.org/10.1039/c4tc01954g.

[59] Huang L, Lord ST. The isolation of fibrinogen monomer dramatically influences fibrin polymerization. Thrombosis Research. 2013; 131(6):e258-263. https://doi.org/10.1016/j.thromres.2013.02.003.

[60] Cardinali B, Profumo A, Aprile A, Byron O, Morris G, Harding SE, Stafford WF, Rocco M. Hydrodynamic and mass spectrometry analysis of nearly-intact human fibrinogen, chicken fibrinogen, and of a substantially monodisperse human fibrinogen fragment X. Arch Biochem Biophys. 2010; 493(2):157-168. https://doi.org/10.1016/j.abb.2009.10.008.

[61] Soe G, Kohno I, Inuzuka K, Itoh Y, Matsuda M. A monoclonal antibody that recognizes a neo-antigen exposed in the E domain of fibrin monomer complexed with fibrinogen or its derivatives: its application to the measurement of soluble fibrin in plasma. Blood. 1996; 88(6):2109-2117. https://doi.org/10.1182/blood.V88.6.2109.bloodjournal8862109.

[62] Wolberg AS, Gabriel DA, Hoffman M. Analyzing fibrin clot structure using a microplate reader. Blood Coagulation & Fibrinolysis. 2002; 13(6):533-539. ISSN:1473-5733.

[63] Hantgan R, Hermans J. Assembly of fibrin. A light scattering study. The Journal of Biological Chemistry. 1979; 254(22):11272-11281. PMID:500644.

[64] Pieters M, Phillippou H, Undas A, de Lange Z, Rijken DC, Mutch NJ. An international study on the feasibility of a standardized combined plasma clot turbidity and lysis assay: communication from the SSC of the ISTH. J Thromb Haemost. 2018; 16(5):1007-1012. https://doi.org/10.1111/jth.14002.

[65] McMeekin TL, Groves ML, Hipp NJ. Refractive indices of amino acids, proteins, and related substances. Adv Chem. 1964; 44:54-66. https://doi.org/10.1021/ba-1964-0044.ch004.

[66] Li W, Sigley J, Baker SR, Helms CC, Kinney MT, Pieters M, Brubaker PH, Cubcciotti R, Guthold M. Nonuniform internal structure of fibrin fibers: protein density and bond density strongly decrease with increasing diameter. BioMed Research International. 2017. https://doi.org/10.1155/2017/6385628.

[67] Carr ME, Shen LL, Hermans J. Mass-length ratio of fibrin fibers from gel permeation and light scattering. Biopolymers. 1977; 16:1-15. https://doi.org/10.1002/bip.1977.360160102.

[68] Chernysh IN, Nagaswami C, Weisel JW. Visualization and identification of the structures formed during early stages of fibrin polymerization. Blood. 2011; 117(17):4609-4614. https://doi.org/10.1182/blood-2010-07-297671.

[69] Light-Sheet Microscopes: MuVi SPIM. Bruker. https://www.bruker.com/en/products-and-solutions/fluorescence-microscopy/light-sheet-microscopes/muvi-spim-family.html.

APPENDIX A: APPROXIMATIONS TO FULL LIGHT SCATTERING THEORY

(Extension of Chapter 1)

A.1: Validity of Approximations to Full Light Scattering Theory

The turbidimetric fitting approaches make several approximations in order to simplify full light scattering theory so that it can be applied to experimental data. The first approximation made by the Carr-Hermans, Original Yeromonahos, and Corrected Yeromonahos approaches is that the fiber length is infinite (L>>λ). This allows for the simplification of the term $Si(qL) \approx \frac{\pi}{2}$, since if L goes to infinity, $Si(qL) = \int_0^\infty \frac{sinx}{x} dx = \frac{\pi}{2}$. It also allows for the simplification that $\left[\frac{\sin\left(\frac{qL}{2}\right)}{\frac{qL}{2}}\right]^2 \approx 0$ since the denominator approaches infinity. However, in some cases, L~λ, making L>>λ a poor assumption. As Ryan et al. [32] show, the average length can be as low as 0.3 μm, which is comparable to the lowest wavelength values used (0.35 μm) in some fitting approaches. However, the smallest average length we recorded from confocal imaging was 1.45 μm, which is considerably larger than the wavelengths used for measurement.

The next assumption made by all three approaches is that $\frac{qd}{2} \ll 1$, which would be true if the fibers are very thin (d<<λ). This allows for the Bessel function to be expanded and keeping the first two terms, $S_{sec} = 1 - \frac{(qd)^2}{16} + \frac{(qd)^4}{1024}$. Then the $\frac{(qd)^4}{1024}$ term can be neglected since if $\frac{qd}{2} \ll 1$, $\frac{(qd)^4}{1024}$ would also be much less than 1. To assess whether $\frac{qd}{2} \ll 1$, we inserted realistic values into the term. For the lowest diameter value we investigated, 10 nm, $\frac{q_{max}d}{2} = 0.18$ where $q_{max} = \frac{4\pi}{350nm} \sin\left(\frac{\pi}{2}\right)$. In this case, $\frac{q_{max}d}{2}$ is much less than 1. For the largest diameter value investigated for the majority of the theoretical analysis, 200 nm, $\frac{q_{max}d}{2} = 3.59$, which is greater than 1, making the assumption invalid. This may explain the increase in error for larger diameter values, especially when using lower wavelength ranges. However, keeping the $\frac{(qd)^4}{1024}$ term in this Taylor expansion would lead to a complicated polynomial equation that cannot be used to accurately determine the parameters.

While the above two assumptions are not always true, these simplifications of the full light scattering theory Rayleigh ratio are necessary in order to get linear equations for fitting experimental turbidity datasets.

Carr and Hermans also use the assumption that $\frac{23}{77}\pi^2 n^2 d^2 \frac{1}{\lambda^2} \ll 1$ in order to make the approximation $\left[1 - \frac{23}{77}\pi^2 n^2 d^2 \frac{1}{\lambda^2}\right]^{-1} = 1 + \frac{23}{77}\pi^2 n^2 d^2 \frac{1}{\lambda^2}$ by keeping the first two terms of the Taylor expansion. The third term in the Taylor expansion would be $\frac{529}{5929}\pi^4 n^4 \frac{d^4}{\lambda^4}$, which for a diameter of 100 nm and a wavelength of 350 nm would be 0.19. Compared to the previous term in the Taylor expansion, $\frac{23}{77}\pi^2 n^2 d^2 \frac{1}{\lambda^2}$, which would be 0.44 for the same diameter and wavelength, this term is not negligible, as assumed. However, Ferri [18] argues that this approximation balances with the previous two approximations, resulting in the linear behavior continuing beyond its limits of applicability. Our theoretical results fitting the turbidimetric approaches to a full light scattering theory dataset confirm this, since the Carr-Hermans approach contains less error than the Original Yeromonahos approach for all of the diameter/length combinations explored, when the Original Yeromonahos approach makes the previous two approximations, but not this one.

We attempted to improve the current approaches by applying fewer simplifications to full light scattering theory, with the hope that it would provide more accurate estimates of the diameter and mass-length ratio. Among the attempted improvements, we tried keeping the sine term in P_{rod}, while making the above simplification that $\frac{2Si(qL)}{qL} \approx \frac{\pi}{qL}$, so that $P_{rod} = \frac{\pi}{qL} -$

$\left[\frac{\sin\left(\frac{qL}{2}\right)}{\frac{qL}{2}}\right]^2$. We also attempted to keep $S_{sec} = 1 - \frac{(qd)^2}{16} + \frac{(qd)^4}{1024}$, instead of neglecting the last term, as described above. Additionally, we tried keeping one more term in the Taylor expansion used by Carr and Hermans so that $\left[1 - \frac{23}{77}\pi^2 n^2 d^2 \frac{1}{\lambda^2}\right]^{-1} = 1 + \frac{23}{77}\pi^2 n^2 d^2 \frac{1}{\lambda^2} + \frac{529}{5929}\pi^4 n^4 d^4 \frac{1}{\lambda^4}$. Finally, we tried adjusting the Carr-Hermans equation by the 2/3 term Yeromonahos added in their correction. Unfortunately, none of these attempts were successful at creating a more accurate fitting approach, as they either led to polynomial equations that were too complicated to fit to the data, imaginary values of diameter, or just increased error in the calculations.

A.2: Determining the Refractive Index and Specific Refractive Index Increment Wavelength Dependence Equations

In order to determine the refractive index of the solution, the program SEDNTERP [25] was used. This program works by inserting the buffer components with their respective concentrations (150 mM sodium chloride, 20 mM HEPES), as well as the pH of the buffer (7.4), and it provides the refractive index for a chosen wavelength. This was done for wavelength values of 350-800 nm, every 50 nm. The refractive index values were then plotted versus $1/\lambda^2$, as seen in Figure A.1, and the linear fit line provided the equation for the wavelength dependence of the refractive index. The refractive index of HBS was also experimentally determined using a portable refractometer, which provided a refractive index of 1.33545 at a wavelength of 588.08 nm, which is in good agreement with the values obtained from the program.

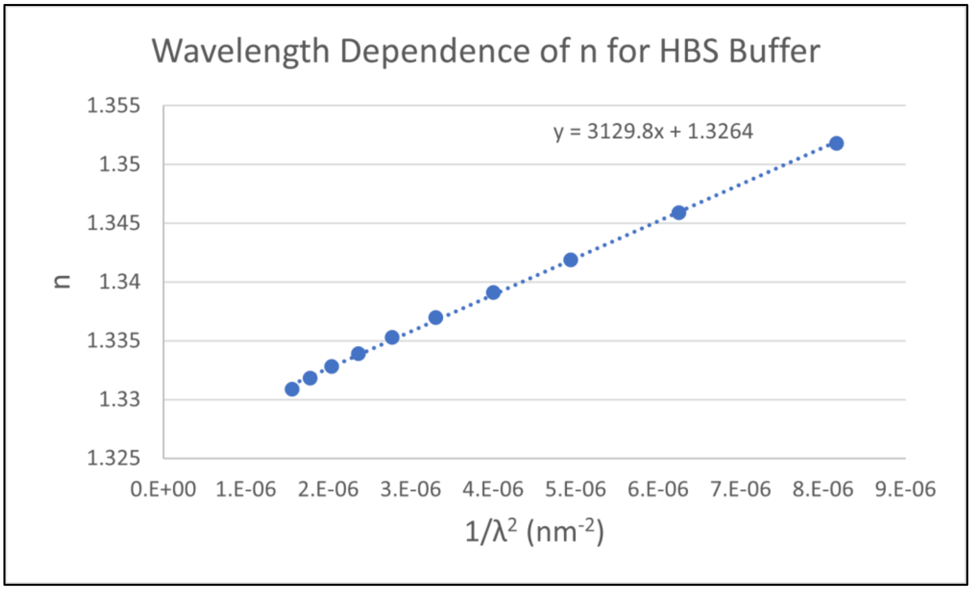

Fig. A.1: Refractive index wavelength dependence determination using the program SEDNTERP.

In order to determine the wavelength dependence of the specific refractive index increment, the program SEDFIT was used [26,27]. This program works by inserting the amino acid sequence of the protein, as well as the refractive index of the buffer at a set wavelength, and it outputs the specific refractive index increment for that wavelength. This was done using the refractive index values obtained using SEDFIT to determine the specific refractive index increment every 50 nm from 350-800 nm. A plot was then made of the specific refractive index increment versus $1/\lambda^2$, as shown in Figure A.2, and the linear fit line provided the equation for the wavelength dependence of the specific refractive index increment.

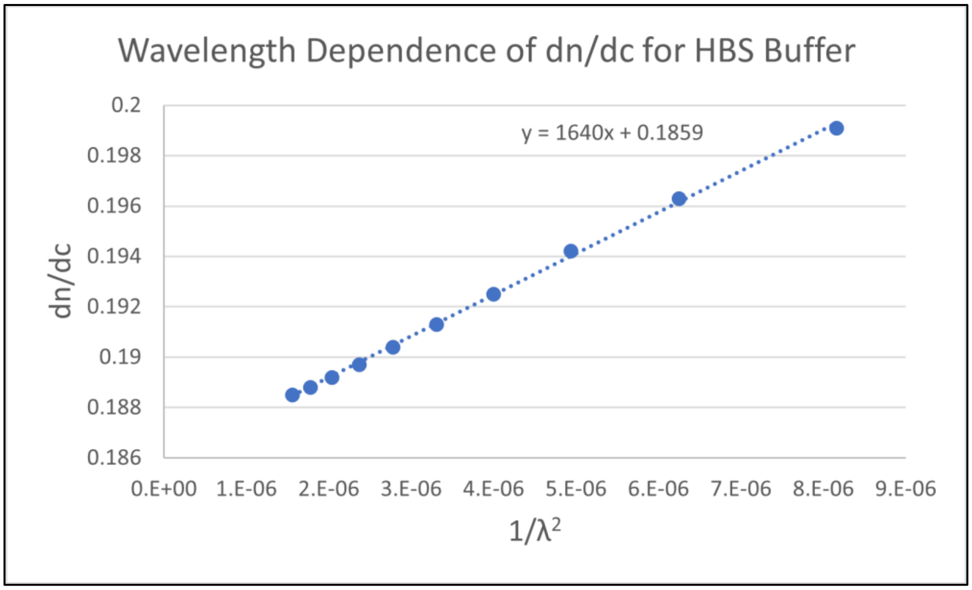

Fig. A.2: Specific refractive index increment wavelength dependence determination using the program SEDFIT.

A.3: Errors in Deriving the "Correction" to the Yeromonahos Approach

In analyzing the "correction" to the Original Yeromonahos approach [21], we discovered that there are several apparent errors in the derivation of obtaining the corrected equation (equations 10.17-10.26 in reference 21). These errors will be briefly discussed. To reduce confusion, all equations from reference 21 will begin with "10" and all equations being introduced in this text will begin with "A.".

The first error is that according to reference 21, integrating Equation 10.16 leads to the equation:

$$P(\theta) = \frac{1}{4k_0L^2}\Big[-2Csc^2\left(\frac{\theta}{2}\right) + 2\cos\Big(2k_0Lsin\left(\frac{\theta}{2}\right)Csc^2\left(\frac{\theta}{2}\right)\Big] + \frac{k_0r^2}{4k_0L^2}[4 -$$

$$\cos\Big(2k_0Lsin\left(\frac{\theta}{2}\right)Csc^2\left(\frac{\theta}{2}\right) + cos\theta\cos\Big(2k_0Lsin\frac{\theta}{2}\Big)Csc^2\left(\frac{\theta}{2}\right)\Big] - \frac{k_0r^2}{4k_0L^3}Csc\left(\frac{\theta}{2}\right)\sin\,(2k_0Lsin\frac{\theta}{2} +$$

$$\frac{1}{k_0 L}\left[Csc\left(\frac{\theta}{2}\right) SinIntegral\left(2k_0 Lsin\frac{\theta}{2}\right)\right] + \frac{k_0 r^2}{4k_0 L}\left[-2Csc\left(\frac{\theta}{2}\right) SinIntegral\left(2k_0 Lsin\frac{\theta}{2}\right) + cos\theta Csc\left(\frac{\theta}{2}\right) SinIntegral\left(2k_0 Lsin\frac{\theta}{2}\right)\right]. \qquad [A.1]$$

where k_0 is the wave number. However, integrating Equation 10.16 using Mathematica 12.1 (Wolfram, Champaign, IL) actually provides the equation:

$$P(\theta) = \frac{1}{4k_0^2 L^3}[4L\left(k_0^2 r^2 - Csc^2\left(\frac{\theta}{2}\right)\right)\sin^2\left(k_0 Lsin\left(\frac{\theta}{2}\right)\right) + k_0 r^2\left(2k_0 L - Csc\left(\frac{\theta}{2}\right)\sin\left(2k_0 Lsin\left(\frac{\theta}{2}\right)\right)\right) + 2k_0 L^2(2 - k_0^2 r^2 + k_0^2 r^2 cos\theta)Csc\left(\frac{\theta}{2}\right) SinIntegral\left(2k_0 Lsin\left(\frac{\theta}{2}\right)\right)]. \qquad [A.2]$$

which does not seem to simplify to Equation A.1.

Next, according to Equation 10.22 in reference 21, $\tau = A\int_0^{\pi} P(\theta)sin\theta(\cos^2\theta + 1)d\theta$ where A is defined as: $A = \frac{2\pi^2 n_s^2}{\lambda^4} m_f^2 \left(\frac{dn}{dc}\right)^2$, where m_f is the protein mass of one fiber. However, based on Equation 10.21, $A = \frac{4\pi^3 n_s^2 c}{\lambda^4} m_f \left(\frac{dn}{dc}\right)^2$, and based on another source [18], A should also include Avogadro's number. Therefore, the correct form of A is given by:

$$A = \frac{4\pi^3 n_s^2 c}{N_A \lambda^4} m_f \left(\frac{dn}{dc}\right)^2. \qquad [A.3]$$

An analytical solution to Equation 10.22 is then given; however, using the correct value of P(θ) as given in Equation A.2 above, the integral cannot be solved analytically using Mathematica 12.1 (Wolfram, Champaign, IL).

Then, only keeping the first order terms in Equation 10.24 would lead to:

$$\int_0^{\pi} P(\theta)\sin\ \theta(\cos^2\theta + 1)d\theta = 4\pi\left(\frac{77 - 23k_0^2 r^2}{105k_0 L}\right) \qquad [A.4]$$

where k_0 is squared in the numerator. However, it is not squared in Equation 10.25 of reference 21.

Finally, combining Equations 10.22 and Equations 10.25 do not provide Equation 10.26 as suggested. Using the equations as given in reference 21, the solution would instead be:

$$\tau\lambda^5 = \pi^2 n\mu^2 L \left(\frac{dn}{dc}\right)^2 \frac{44}{15}\left[\lambda^2 - \frac{46}{77}r^2\pi n\lambda\right]. \qquad \text{[A.5]}$$

However, Equation A.5 uses the incorrect value of A. Using the correct value of A along with erroneous Equation 10.25 provides:

$$\tau\lambda^5 = \frac{\pi^3 cn\mu}{N_A}\left(\frac{dn}{dc}\right)^2 \frac{88}{15}\left[\lambda^2 - \frac{46}{77}r^2\pi n\lambda\right]. \qquad \text{[A.6]}$$

and using the correct value of A as well as the k_0 value being squared as in Equation A.4, the solution would then be:

$$\tau\lambda^5 = \frac{\pi^3 cn\mu}{N_A}\left(\frac{dn}{dc}\right)^2 \frac{88}{15}\left[\lambda^2 - \frac{92}{77}\pi^2 r^2 n^2\right] \qquad \text{[A.7]}$$

which is actually the original Yeromonahos equation (Equation 26). However, none of these results provide the “corrected” Yeromonahos equation (Equation 35), as suggested. Thus, the factor of 2/3 that differentiates Equation 26 from Equation 35 has no physical basis.

APPENDIX B: EFFECTS OF CHANGING PARAMETERS ON SIMULATED RESULTS

(Extension of Chapter 2)

B.1: Trapezoidal Summation vs. Numerical Integration of Rayleigh Ratio

In order to confirm that the Mathematica numerical integration was performing properly to solve Equation 9, we also performed a trapezoidal rule summation, which makes the assumption that:

$$\int_a^b f(x)dx \approx (b-a)\frac{f(a)-f(b)}{2}. \qquad \text{[B.1]}$$

Plugging arbitrary values for n, dn/dc, λ, c, μ, and L into the Rayleigh ratio, and breaking the function into 20 equal parts from a to b, the trapezoidal summation provided a value that had a percent difference of only 0.6% from the value reported by the Mathematica numerical summation, showing that the Mathematica numerical simulation was working properly.

B.2: Wavelength Dependence of the Refractive Index and Specific Refractive Index Increment

As discussed in Chapter 2, many people use constant values of n and dn/dc, when those terms actually contain a dependence on the wavelength being used for measurements. This dependence on the wavelength can be seen in Figure B.1 where the values of n and dn/dc are plotted versus the wavelength for fibrin fibers in HBS buffer. As García et al. [31] discussed, the two terms contain a larger dependence on the wavelength range at smaller wavelength values, but as seen in the results in Chapter 2, there is still a significant amount of added error when using constant values for these terms rather than accounting for their wavelength dependence.

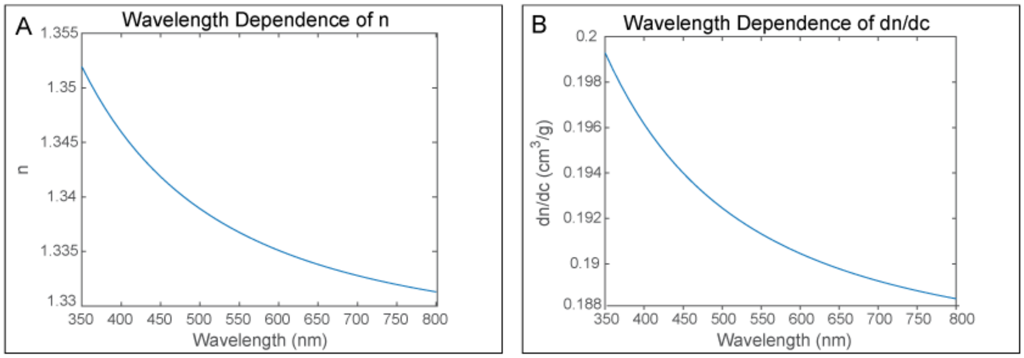

Fig. B.1: The wavelength dependence of A) the refractive index, and B) the specific refractive index increment for fibrin fibers in HBS buffer from 350-800 nm.

As described in the main text, experimental data must be plotted in a different format when accounting for the wavelength dependence of n and dn/dc in the turbidimetric fitting approaches so that the equations using the slope and y-intercept to solve for the diameter and mass-length ratio do not include the n(λ) and dn/dc(λ) terms. Figure B.2 below shows the turbidimetry data created using full light scattering theory plotted in the original formats, as well as the wavelength corrected formats for each of the approaches for a wavelength range of 350-800 nm.

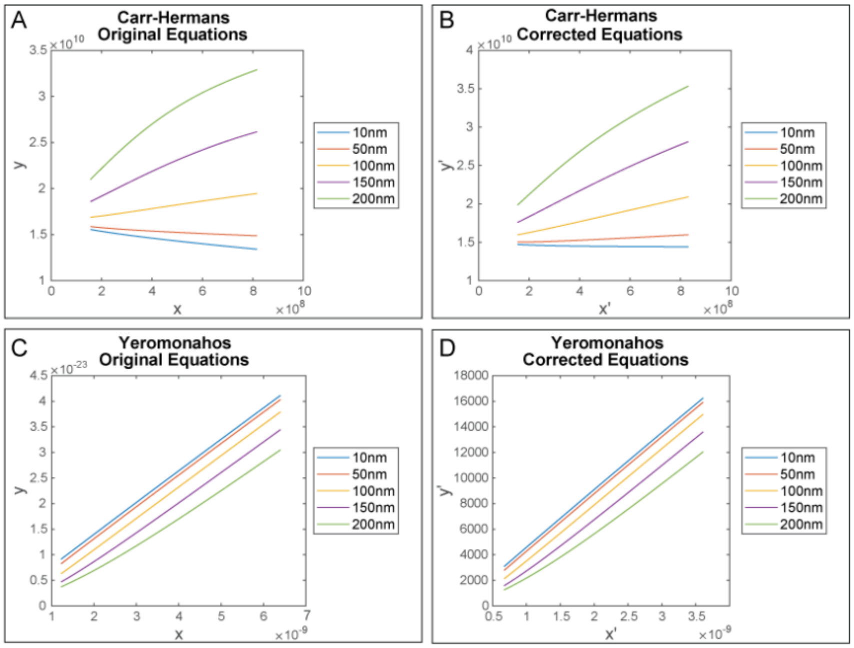

Fig. B.2: A theoretical turbidity dataset created using full light scattering theory (Equations 7-9) plotted as A) $\frac{c}{\tau\lambda^3}$ vs. $\frac{1}{\lambda^2}$, B) $\frac{\left[\left(\frac{dn}{dc}\right)(\lambda)\right]^2}{<\frac{dn}{dc}>^2}\frac{n(\lambda)}{<n>}\frac{c}{\tau\lambda^3}$ vs. $\frac{n^2(\lambda)}{<n>^2}\frac{1}{\lambda^2}$, C) $\tau\lambda^5$ vs. λ^2, and D) $\frac{\tau\lambda^5}{A'}$ vs. $\frac{\lambda^2}{n(\lambda)^2}$, for diameters of 10, 50, 100, 150, and 200 nm. (L=5 μm, c=0.0001 g/cm^3, μ=4.73*10^{12} Da/cm, λ=350-800 nm, values of n and dn/dc for HBS buffer).

B.3: Diameter/Mass-Length Ratio Values Given by Fits

Table B.1 gives the values of diameter calculated by the fitting approaches for lengths of 0.5 and 5 μm and diameters of 50 and 150 nm. For all three of the approaches at both wavelength ranges, when the length is small (0.5 μm) and the diameter is small (50 nm), fitting the full light scattering theory data with the turbidimetric approaches provides imaginary values for the diameter, which we assigned a value of 100% error for plotting purposes. This is shown by the purple bars in Figure 5 for small diameter values.

The amount of error in the estimates of diameter by the approaches then decreases for increasing diameter, as well as increasing length, other than an increase in the error by the Original and Corrected Yeromonahos approaches for diameters of 150 nm with lengths of 5 μm, as compared to the error for a diameter of 50 nm and length of 5 μm.

A

Carr-Hermans	Input L (μm)	Input d (nm)	d from Fit (nm)	% Error in d
350-650 nm	0.5	50	Imaginary	*100
	0.5	150	127.52	14.99
	5	50	44.37	11.26
	5	150	139.04	7.31
500-800 nm	0.5	50	Imaginary	*100
	0.5	150	118.15	21.23
	5	50	35.35	29.30
	5	150	145.84	2.77

B

Original Yeromonahos	Input L (μm)	Input d (nm)	d from Fit (nm)	% Error in d
350-650 nm	0.5	50	Imaginary	*100
	0.5	150	96.20	35.87
	5	50	41.39	17.22
	5	150	101.96	32.03
500-800 nm	0.5	50	Imaginary	*100
	0.5	150	98.62	34.25
	5	50	33.10	33.80
	5	150	116.64	22.24

C

Corrected Yeromonahos	Input L (μm)	Input d (nm)	d from Fit (nm)	% Error in d
350-650 nm	0.5	50	Imaginary	*100
	0.5	150	117.83	21.45
	5	50	50.69	1.38
	5	150	124.88	16.75
500-800 nm	0.5	50	Imaginary	*100
	0.5	150	120.78	19.48
	5	50	40.53	18.94
	5	150	142.86	4.76

Table B.1: Values of diameter (input d) at lengths of 0.5 μm and 5 μm (input L) used in the full light scattering theory equation (Equations 7-9) to create the turbidity dataset, compared to the value given out from a linear line of best fit to that data (d from fit) using the A) Carr-Hermans approach, B) Original Yeromonahos approach, and C) Corrected Yeromonahos approach, and the calculated percent error between the input value and the value given by the approach (% error in d). (c=0.0001 g/cm^3; μ=4.73*10^{12} Da/cm; imaginary diameters assigned a value of 100% error).

Figure B.3 shows which approach is best for determining the diameter for each fiber length/diameter combination (shown by the color), as well as the approaches that result in less than ten percent error for that length/diameter combination (shown by the letters). If no approaches result in less than ten percent error for a length/diameter combination, no information is given.

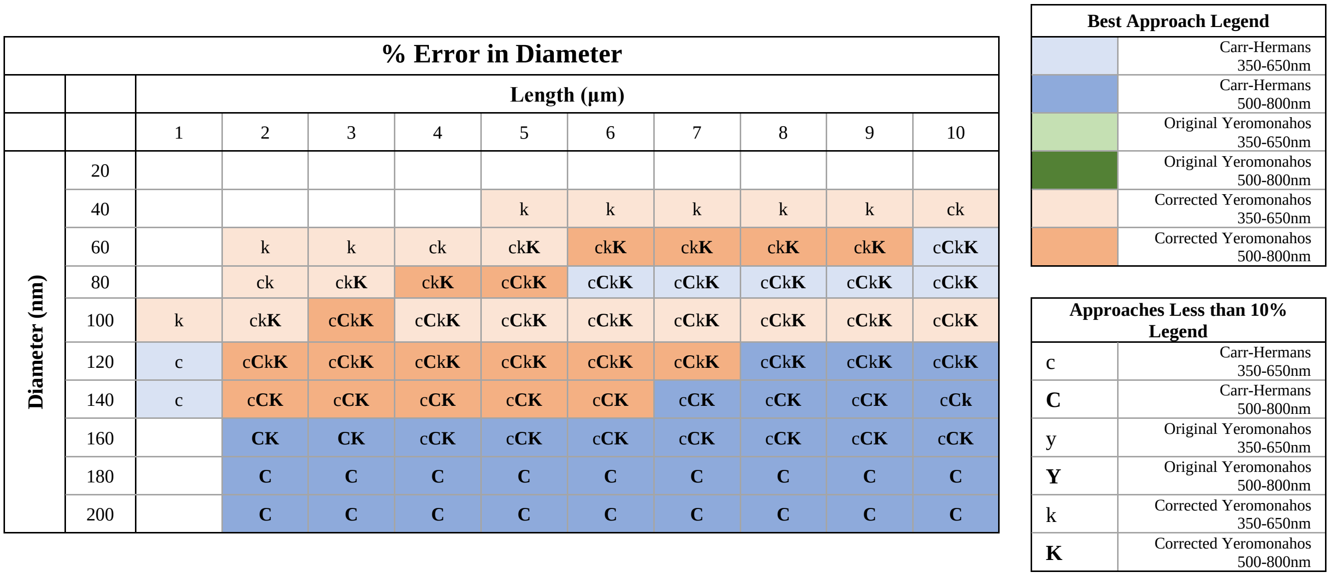

% Error in Diameter

Diameter (nm)		Length (µm)									
		1	2	3	4	5	6	7	8	9	10
	20										
	40					k	k	k	k	k	ck
	60		k	k	ck	ck**K**	ck**K**	ck**K**	ck**K**	ck**K**	c**C**k**K**
	80		ck	ck**K**	ck**K**	c**C**k**K**	c**C**k**K**	c**C**k**K**	c**C**k**K**	c**C**k**K**	c**C**k**K**
	100	k	ck**K**	c**C**k**K**	c**C**k**K**	c**C**k**K**	c**C**k**K**	c**C**k**K**	c**C**k**K**	c**C**k**K**	c**C**k**K**
	120	c	c**C**k**K**	c**C**k**K**	c**C**k**K**	c**C**k**K**	c**C**k**K**	c**C**k**K**	c**C**k**K**	c**C**k**K**	c**C**k**K**
	140	c	c**CK**	c**CK**	c**CK**	c**CK**	c**CK**	c**CK**	c**CK**	c**CK**	c**C**k
	160		**CK**	**CK**	c**CK**	c**CK**	c**CK**	c**CK**	c**CK**	c**CK**	c**CK**
	180		**C**	**C**	**C**	**C**	**C**	**C**	**C**	**C**	**C**
	200		**C**	**C**	**C**	**C**	**C**	**C**	**C**	**C**	**C**

Best Approach Legend	
🟦	Carr-Hermans 350-650nm
🟦	Carr-Hermans 500-800nm
🟩	Original Yeromonahos 350-650nm
🟩	Original Yeromonahos 500-800nm
🟧	Corrected Yeromonahos 350-650nm
🟧	Corrected Yeromonahos 500-800nm

Approaches Less than 10% Legend	
c	Carr-Hermans 350-650nm
C	Carr-Hermans 500-800nm
y	Original Yeromonahos 350-650nm
Y	Original Yeromonahos 500-800nm
k	Corrected Yeromonahos 350-650nm
K	Corrected Yeromonahos 500-800nm

Fig. B.3: Summary of best approaches/approaches that provide less than 10% error for determining fibrin diameter at lengths of 1-10 µm and diameters of 20-200 nm. The color shows the best approach for that diameter/length combination and the letters show the approaches that provide less than 10% error for that diameter/length combination.

Table B.2 shows the actual mass-length ratio values calculated by the approaches for lengths of 0.5 and 5 µm and diameters of 50 and 150 nm. As can be seen, for all three approaches the percent error in the mass-length ratio increases with increasing diameter and decreases with increasing length.

A

Carr-Hermans	Input L (μm)	Input d (nm)	Input μ (Da/cm * 10^{-12})	μ from Fit (Da/cm * 10^{-12})	% Error in μ
350-650 nm	0.5	50	4.73	3.45	27.06
	0.5	150	4.73	3.14	33.62
	5	50	4.73	4.52	4.44
	5	150	4.73	4.31	8.88
500-800 nm	0.5	50	4.73	3.20	32.35
	0.5	150	4.73	3.05	35.52
	5	50	4.73	4.46	5.71
	5	150	4.73	4.43	6.34

B

Yeromonahos	Input L (μm)	Input d (nm)	Input μ (Da/cm * 10^{-12})	μ from Fit (Da/cm * 10^{-12})	% Error in μ
350-650 nm	0.5	50	4.73	3.40	28.12
	0.5	150	4.73	2.93	38.05
	5	50	4.73	4.50	4.86
	5	150	4.73	3.97	16.07
500-800 nm	0.5	50	4.73	3.14	33.62
	0.5	150	4.73	2.96	37.42
	5	50	4.73	4.46	5.71
	5	150	4.73	4.23	10.57

Table B.2: Values of mass-length ratio (input μ) at diameters of 50 and 150 nm (input d) and lengths of 0.5 μm and 5 μm (input L) used in the full light scattering theory equation to create the turbidity dataset, compared to the value given out from a linear line of best fit to that data (μ from fit) using the A) Carr-Hermans approach, and B) Original and Corrected Yeromonahos approaches, and the calculated percent error between the input value and value given by the fit (% error in μ). ($c=0.0001$ g/cm^3).

Figure B.4 shows which approach is best for determining the mass-length ratio for each fiber length/diameter combination (shown by the color), as well as the approaches that result in less than ten percent error for that length/diameter combination (shown by the letters). If no approaches result in less than ten percent error for a length/diameter combination, no information is given.

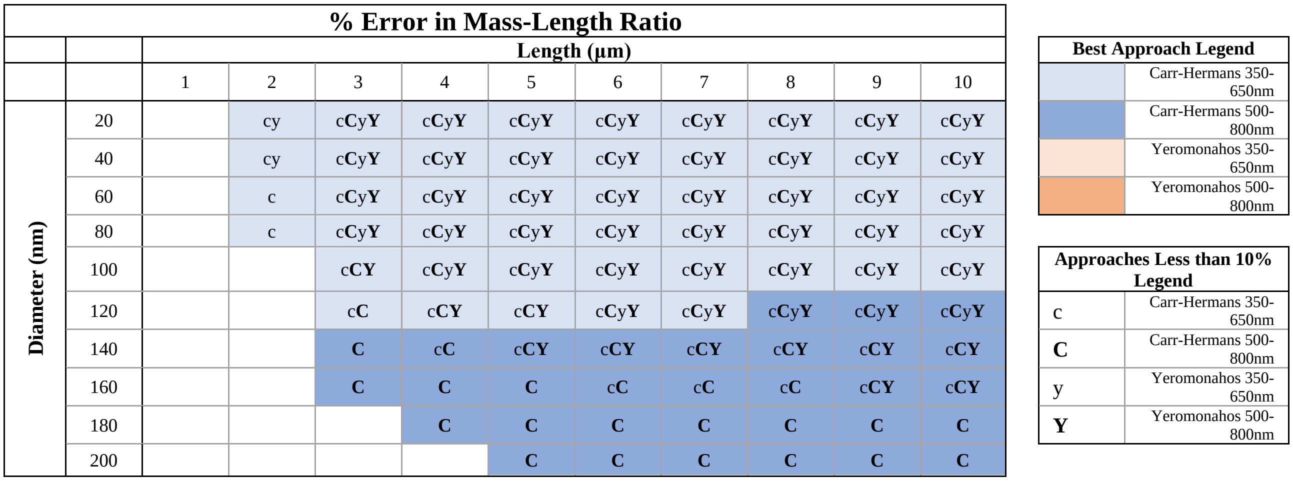

% Error in Mass-Length Ratio											
		Length (µm)									
		1	2	3	4	5	6	7	8	9	10
Diameter (nm)	20		cy	cCyY	cCyY	cCyY	cCyY	cCyY	cCyY	cCyY	cCyY
	40		cy	cCyY	cCyY	cCyY	cCyY	cCyY	cCyY	cCyY	cCyY
	60		c	cCyY	cCyY	cCyY	cCyY	cCyY	cCyY	cCyY	cCyY
	80		c	cCyY	cCyY	cCyY	cCyY	cCyY	cCyY	cCyY	cCyY
	100			cCY	cCyY	cCyY	cCyY	cCyY	cCyY	cCyY	cCyY
	120			cC	cCY	cCY	cCyY	cCyY	cCyY	cCyY	cCyY
	140			C	cC	cCY	cCY	cCY	cCY	cCY	cCY
	160			C	C	C	cC	cC	cC	cCY	cCY
	180				C	C	C	C	C	C	C
	200					C	C	C	C	C	C

Best Approach Legend	
	Carr-Hermans 350-650nm
	Carr-Hermans 500-800nm
	Yeromonahos 350-650nm
	Yeromonahos 500-800nm

Approaches Less than 10% Legend	
c	Carr-Hermans 350-650nm
C	Carr-Hermans 500-800nm
y	Yeromonahos 350-650nm
Y	Yeromonahos 500-800nm

Fig. B.4: Summary of best approaches/approaches that provide less than 10% error for determining fibrin mass-length ratio at lengths of 1-10 µm and diameters of 20-200 nm. The color shows the best approach for that diameter/length combination and the letters show the approaches that provide less than 10% error for that diameter/length combination.

B.4: Effects of Changing Fibrinogen Concentration, Fiber Diameter, Fiber Length, and Mass-Length Ratio on Simulated Results

Effects of Fibrinogen Concentration

A theoretical turbidity dataset was created using the full light scattering theory (Equations 7-9) for concentrations of 0.001 g/cm^3 (1 mg/mL), 0.008 g/cm^3 (8 mg/mL), 0.0001 g/cm^3 (0.1 mg/mL), and 0.00001 g/cm^3 (0.01 mg/mL) (physiological values are between 0.0015 and 0.004 g/cm^3). There was no difference in the percent error between the values calculated using the three approaches compared to the values used to create the full light scattering theory dataset with changing fibrinogen concentration. Therefore, the percent error is independent of fibrinogen concentration. This is due to the fact that the Rayleigh ratio, R(θ), depends linearly on concentration, and therefore turbidity depends linearly on the concentration. Then since for the Carr-Hermans approach (corrected for the wavelength dependence of n and dn/dc) the y-data in the plots contains c in the numerator and turbidity in the denominator ($\frac{\left(\frac{dn}{dc}(\lambda)\right)^2}{<\frac{dn}{dc}>^2}\frac{n(\lambda)}{<n>}\frac{c}{\tau\lambda^3}$), the concentration dependence will cancel out, resulting in the full light scattering data being independent of fibrinogen concentration. Similarly, for the Yeromonahos approaches (corrected for the wavelength dependence of n and dn/dc), turbidity is in the numerator and concentration is in the denominator for the y-data in the plots ($\frac{\tau\lambda^5}{\left(\frac{88}{15}\right)\pi^3 n(\lambda)^3 \frac{c}{N_A}\left(\frac{dn}{dc}(\lambda)\right)^2}$), so since turbidity is linearly dependent on concentration, the concentration dependence will cancel out. Therefore, the datasets do not change with changing fibrinogen concentration, causing the percent error in the different approaches to also be independent of fibrinogen concentration.

Effects of Fiber Diameter

The effect of changing diameter on full light scattering theory (Equations 7-9) can be seen in Figure B.5. As can be seen with the Carr-Hermans plots, for the small diameter values (10 and 50 nm), the slopes of the plots are negative, whereas they are positive for diameters of 100, 150, and 200 nm. Since the diameter is solved for by taking the square root of the slope, this translates to an imaginary value of the diameter. Then, for the Yeromonahos plots, there is a positive y-intercept for fibers with small diameters, and since the diameter is solved for by taking the square root of the negative of the y-intercept, a positive y-intercept would result in an imaginary value of the diameter. The imaginary numbers were assigned a value of 100% error for plotting purposes, and they are shown in purple in Figure 5. The reasoning for this change in slope and y-intercept for the full light scattering theory data is unclear, due to the fact that Equation 9 cannot be integrated analytically, and therefore, it cannot be written in terms of the plotted y’ and x’ variables used for the fitting approaches ($\frac{\left[\frac{dn}{dc}(\lambda)\right]^2}{\langle\frac{dn}{dc}\rangle^2}\frac{n(\lambda)}{\langle n\rangle}\frac{c}{\tau\lambda^3}$ and $\frac{n^2(\lambda)}{\langle n\rangle^2}\frac{1}{\lambda^2}$ for the Carr-Hermans approach, and $\frac{\tau\lambda^5}{\left(\frac{88}{15}\right)\pi^3 n(\lambda)^3\frac{c}{N_A}\left[\frac{dn}{dc}(\lambda)\right]^2}$ and $\frac{\lambda^2}{n(\lambda)^2}$ for the Yeromonahos approaches).

The increased error in the calculations of both the diameter and mass-length ratios for large diameter fibers for all three approaches can be accounted for by the fact that the full light scattering theory plots are nonlinear for large diameters, especially at small wavelength values, as seen in Figure B.5. This nonlinearity results in a poor fit of the linear line, which results in inaccurate calculations of both the diameters and mass-length ratios for fibers with large diameters.

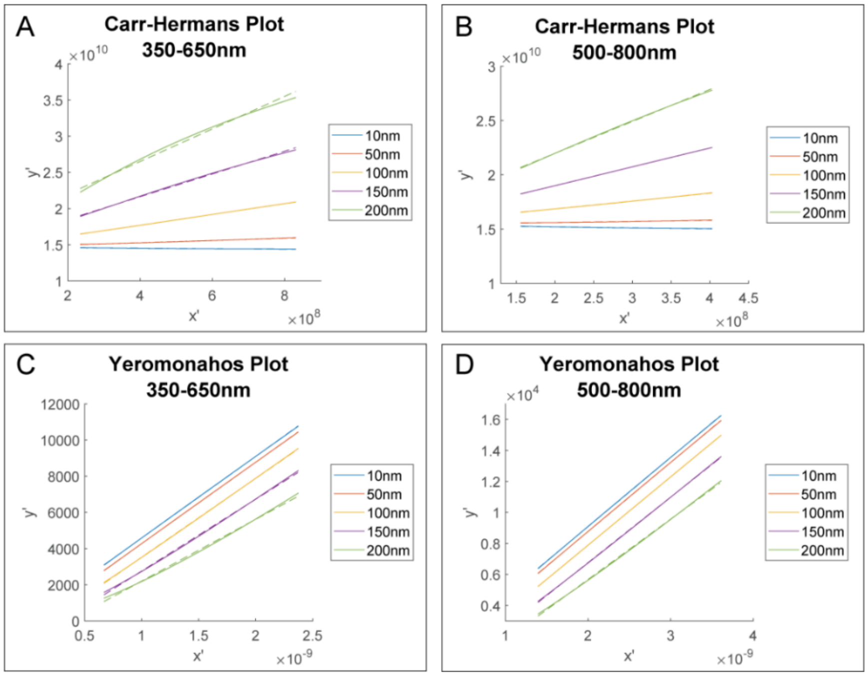

Fig. B.5: A theoretical turbidity dataset created using full light scattering theory for diameters of 10, 50, 100, 150, and 200 nm plotted in A) the Carr-Hermans method of $\frac{\left(\frac{dn}{dc}(\lambda)\right)^2}{<\frac{dn}{dc}>^2}\frac{n(\lambda)}{<n>}\frac{c}{\tau\lambda^3}$ vs. $\frac{n^2(\lambda)}{<n>^2}\frac{1}{\lambda^2}$ for the 350-650 nm wavelength range and B) 500-800 nm wavelength range and C) the Yeromonahos method of $\frac{\tau\lambda^5}{A'}$ vs. $\frac{\lambda^2}{n(\lambda)^2}$ for the 350-650 nm wavelength range and D) 500-800 nm wavelength range (c=0.0001 g/cm^3; μ=4.73*10^{12} Da/cm, L=5 μm; the dashed lines represent the best linear fit to each dataset).

Figures B.6 and B.7 below show the percent error in the diameter and mass-length ratio, respectively, for diameters ranging from 20-400 nm, instead of for 10-200 nm as in Figures 5 and 6. The error in all three turbidimetry approaches increases for both the estimates of the diameter and the mass-length ratio above diameters of 200 nm. This is the case for both the 350-650 nm wavelength range as well as the 500-800 nm wavelength range. The full light scattering theory (Equations 7-9) uses a form factor for "thin" rods, suggesting that as diameters increase and approach the wavelength, the form factor equation becomes less applicable. This may explain why the percent error increases above diameters of 200 nm.

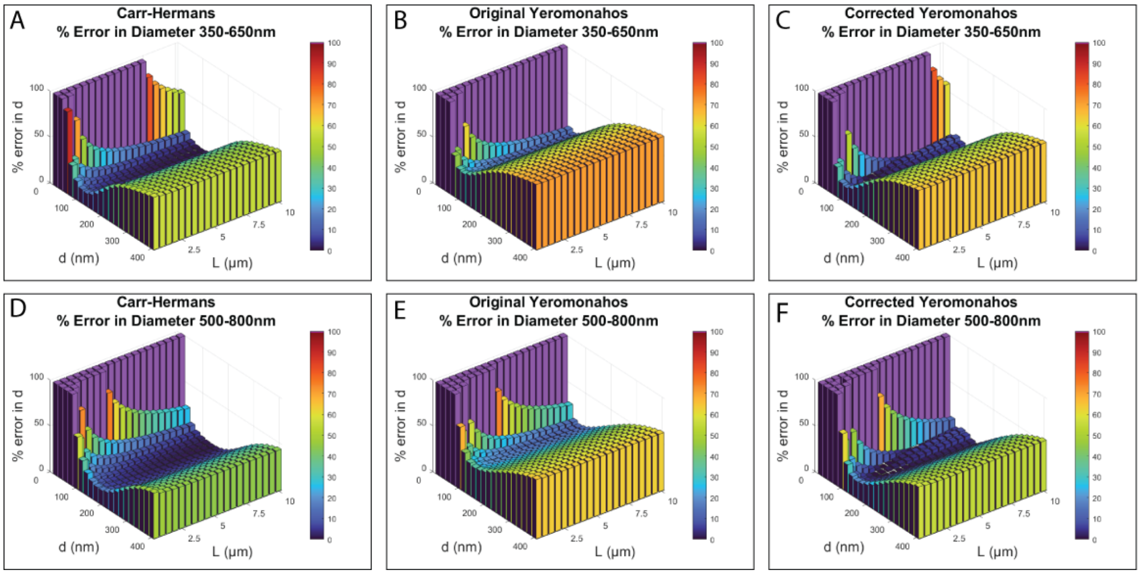

Fig. B.6: Percent error between the diameter obtained from fitting the three approaches to theoretical turbidity values created using full light scattering theory and the value used to create the initial dataset for lengths of 0.5-10 μm and diameters of 20-400 nm for wavelength ranges of 350-650 nm (A-C) and 500-800 nm (D-F). (c=0.0001 g/cm^3, μ=4.73*10^{12} Da/cm, dn/dc and n corrected for wavelength dependence for fibers in HBS buffer; the purple bars represent imaginary diameter values calculated from the fit and were assigned a value of 100% error).

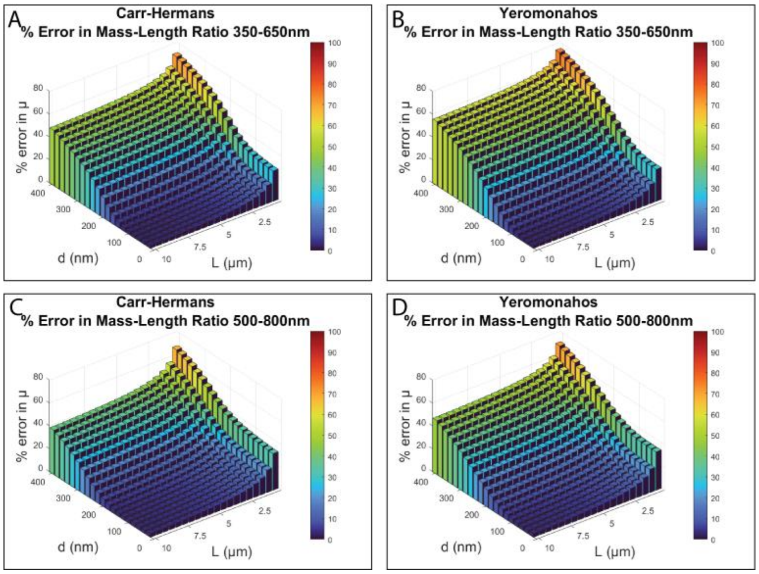

Fig. B.7: Percent error between the mass-length ratio obtained from fitting the approaches to theoretical turbidity values created using full light scattering theory and the value used to create the initial dataset for lengths of 0.5-10 μm and diameters of 20-400 nm for wavelength ranges of 350-650 nm (A-B) and 500-800 nm (C-D). (c=0.0001 g/cm^3, μ=4.73*10^{12} Da/cm, dn/dc and n corrected for wavelength dependence for fibers in HBS buffer).

Effects of Fiber Length

All three of the methods evaluated to extract diameter and mass-length ratio from turbidimetry values assume that the fibers are infinitely long, but it has been found that fiber lengths range from 0.3-4.8 μm [32]. Figure B.8 shows the representative plots of $\frac{\left(\frac{dn}{dc}(\lambda)\right)^2}{<\frac{dn}{dc}>^2}\frac{n(\lambda)}{<n>}\frac{c}{\tau\lambda^3}$ vs. $\frac{n^2(\lambda)}{<n>^2}\frac{1}{\lambda^2}$ and $\frac{\tau\lambda^5}{A'}$ vs. $\frac{\lambda^2}{n(\lambda)^2}$ for fibers of 100 nm diameter and 4.73*10^{12} Da/cm mass-length ratio created using full light scattering theory (Equations 7-9) at lengths ranging from 0.5-10 μm. As can be seen, the data from the full light scattering theory are less linear with decreasing fiber lengths, although this is less obvious in the Yeromonahos plot formats. Since the three approaches apply a linear fit to the data, this nonlinearity in the full light scattering data results in some inaccuracies in the values determined by the approaches for fibers with small lengths.

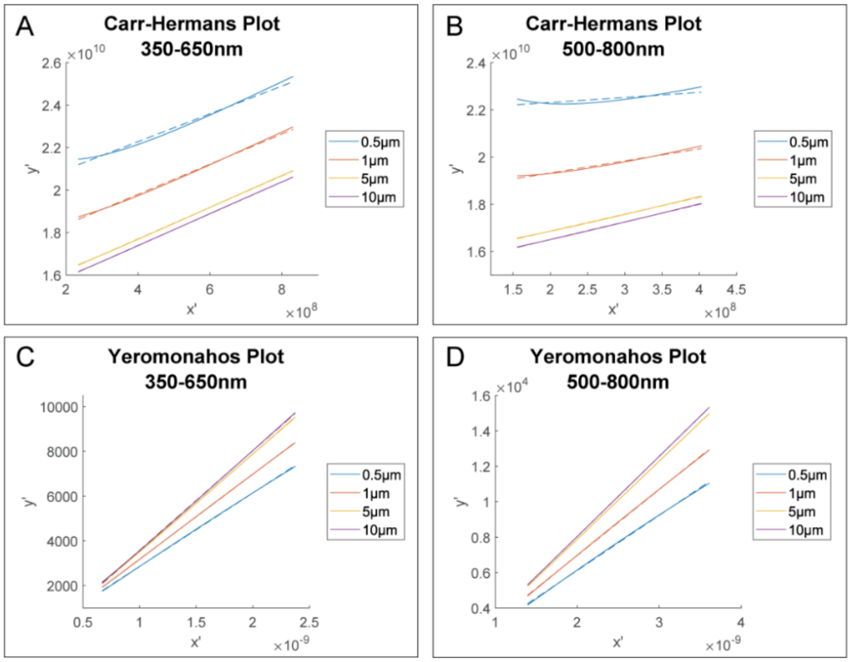

Fig. B.8: Theoretical turbidity values created using full light scattering theory for lengths of 0.5, 1, 5, and 10 µm plotted in A) the Carr-Hermans format of $\frac{\left(\frac{dn}{dc}(\lambda)\right)^2}{<\frac{dn}{dc}>^2}\frac{n(\lambda)}{<n>}\frac{c}{\tau\lambda^3}$ vs. $\frac{n^2(\lambda)}{<n>^2}\frac{1}{\lambda^2}$ for 350-650 nm and B) 500-800 nm and C) the Yeromonahos format of $\frac{\tau\lambda^5}{A'}$ vs. $\frac{\lambda^2}{n(\lambda)^2}$ for 350-650 nm and D) 500-800 nm. (d=100 nm, µ=4.73*10^{12} Da/cm, c=0.0001 g/cm^3; the dashed lines represent the best linear fit to each dataset).

Effects of Mass-Length Ratio

A theoretical turbidity dataset was created using the full light scattering theory (Equations 7-9) for mass-length ratios of 2*10^{11} Da/cm, 4.73*10^{11} Da/cm, 4.73*10^{12} Da/cm, and 4.73*10^{13} Da/cm. There was no difference in the percent error between the values calculated using the three approaches compared to the values used to create the full light scattering theory dataset with changing mass-length ratio. Therefore, the percent error is independent of mass-length ratio. This is due to the fact that changing the mass-length ratio changes the Rayleigh ratio for full light scattering theory, which in turn changes the turbidity values. This results in a change to the y-data for full light scattering theory plotted in the formats for analysis ($\frac{\left(\frac{dn}{dc}(\lambda)\right)^2}{<\frac{dn}{dc}>^2}\frac{n(\lambda)}{<n>}\frac{c}{\tau\lambda^3}$ for the

Carr-Hermans approach with n and dn/dc corrected for wavelength dependence and $\frac{\tau\lambda^5}{\left(\frac{88}{15}\right)\pi^3 n(\lambda)^3 \frac{c}{N_A}\left(\frac{dn}{dc}(\lambda)\right)^2}$ for the Yeromonahos approaches with n and dn/dc corrected for wavelength dependence). Therefore, a change in mass-length ratio would cause an upward or downward shift in the dataset by a certain factor, but it does not change the overall shape of the dataset, and therefore does not impact the fit of a linear line to the data. Thus, the actual values calculated for the diameter and mass-length ratio will change with changing mass-length ratio, but the percent error in the calculations would be unaffected.

APPENDIX C: EXTENDED EXPERIMENTAL ANALYSIS OF FIBRIN FIBER STRUCTURE (Extension of Chapter 3)

C.1: Crosslinking of Fibrin by FXIIIa

A western blot was performed in order to confirm that the fibrinogen was being crosslinked by the FXIIIa, as shown in Figure C.1. As seen, there is a clear Aα, Bβ, and γ chain for the non-crossed fibrin sample, with no visible higher bands. For the crosslinked sample containing FXIIIa, the Aα and γ chains are much fainter, as some of those chains are now crosslinked, leading to the higher α polymer and γ-γ crosslinking bands. This shows that the fibrin is in fact being cross-linked by the presence of the FXIIIa in the solution.

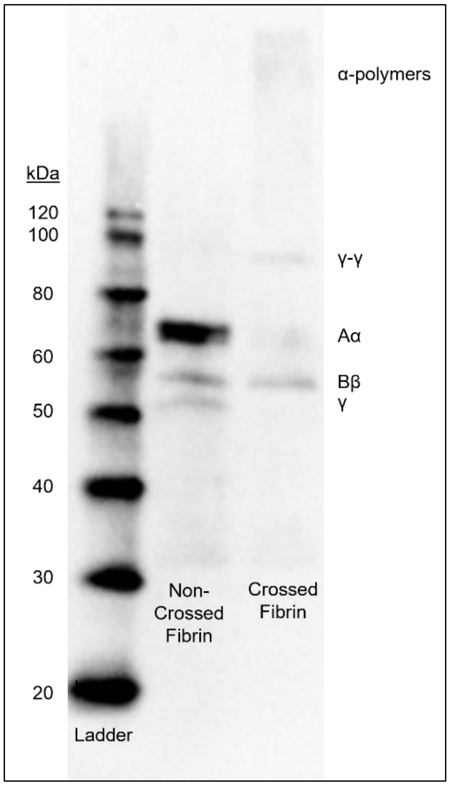

Fig. C.1: Western blot of fibrin with and without FXIIIa, with a MagicMark standard providing reference masses in kDa.

C.2: SEM vs. STORM Imaging

An image showing the methods for preparing a fibrin clot for SEM imaging is shown in Figure C.2. A fibrin clot prepared for STORM imaging is shown in Figure C.3.

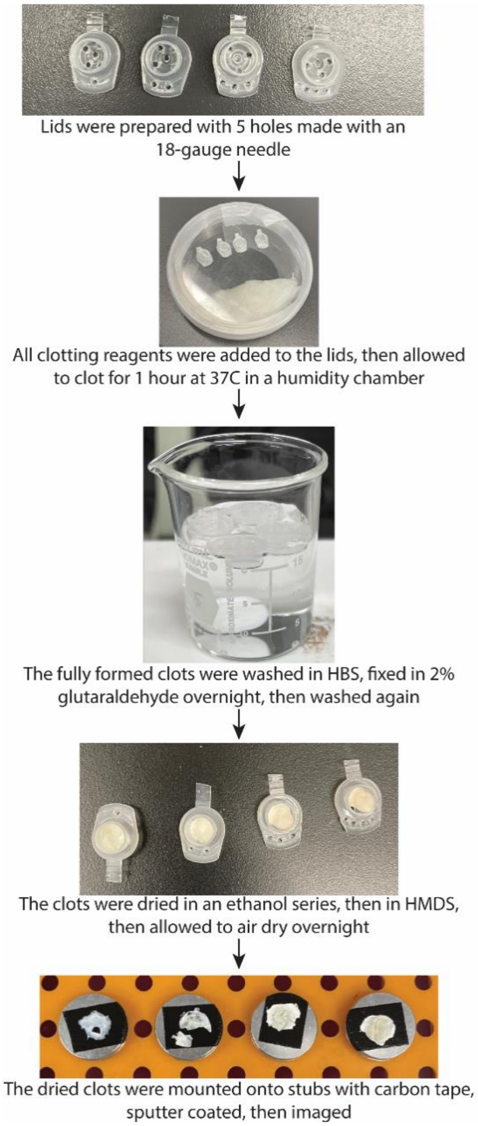

Fig. C.2: The methods of preparing a fibrin clot for SEM imaging.

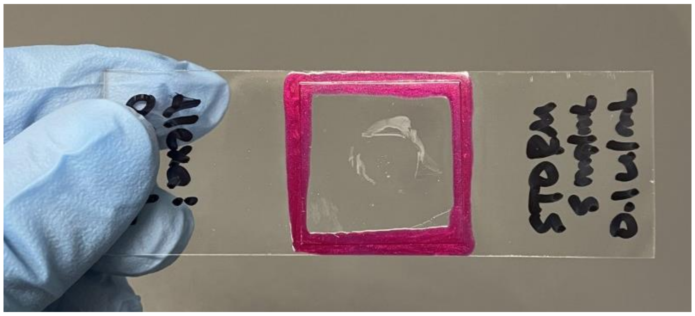

Fig. C.3: A representative fibrin clot prepared for STORM imaging.

Representative SEM and STORM images for each investigated fibrinogen/thrombin concentration can be seen in Figure C.4 and C.5, respectively. The average diameter obtained for each clot condition using the two methods is provided in Table C.1. Using a single factor ANOVA test, $p<0.001$ for the diameters obtained using SEM imaging for the changing fibrinogen concentrations, and for the changing thrombin concentrations, showing that there is a significant difference in the diameter with changing clot conditions.

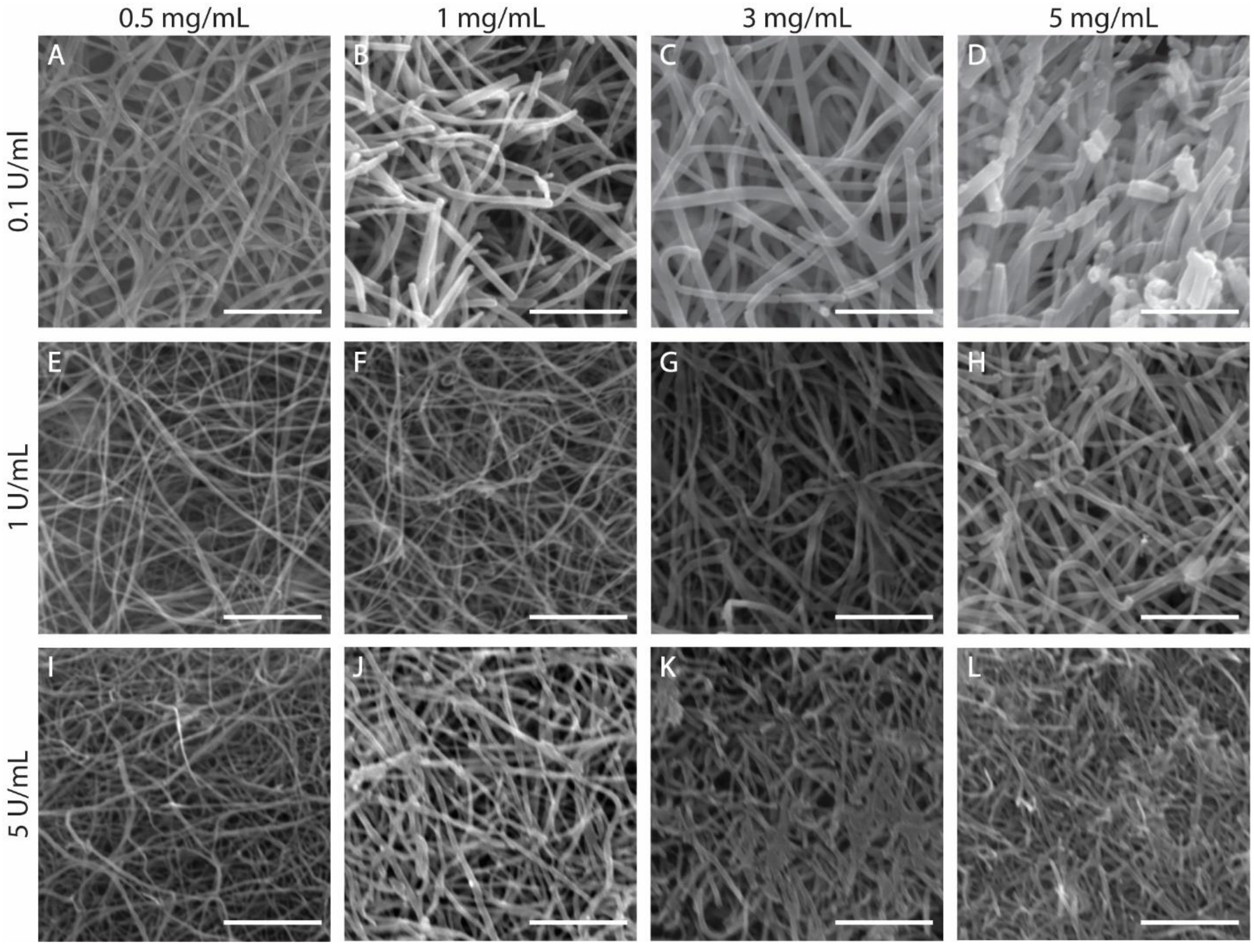

Fig. C.4: Representative SEM images for each investigated fibrinogen and thrombin concentration (noted by column and row headings, respectively) imaged at 21.96 kx magnification at 15 kV using a Zeiss EVO 10 (scale bars 3 μm).

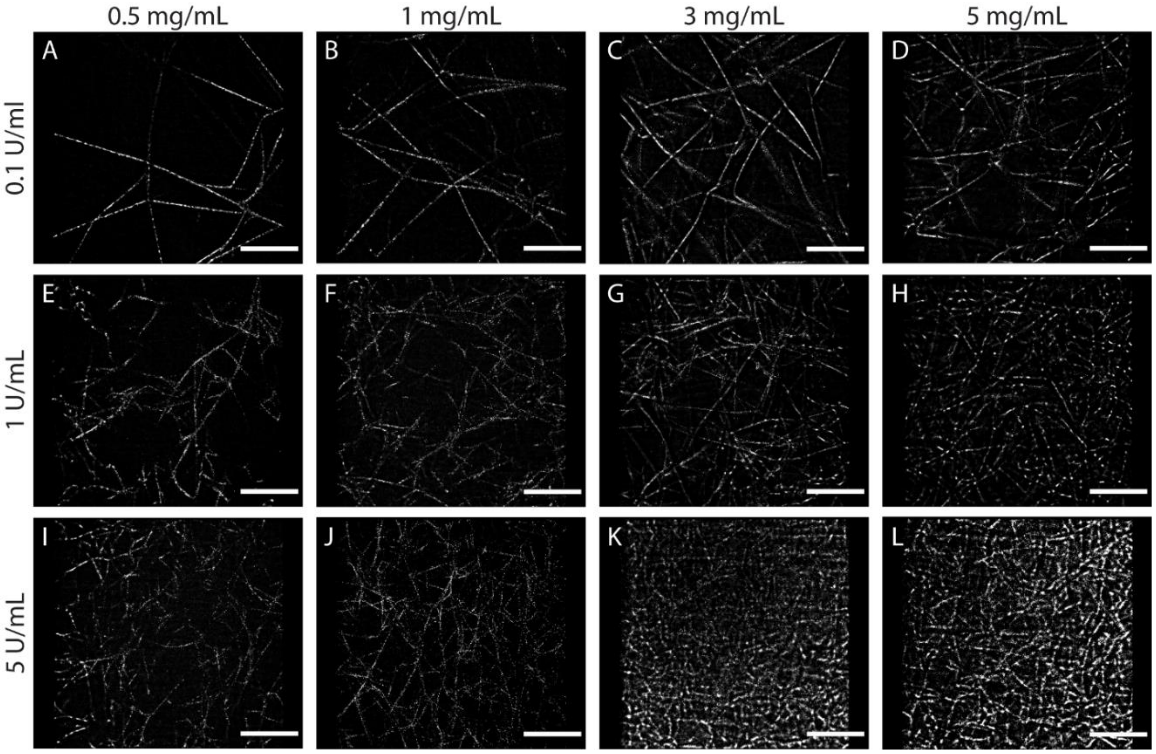

Fig. C.5: Representative STORM images for each investigated fibrinogen/thrombin concentration (noted by column and row headings, respectively). AlexaFluor-647-labeled fibrinogen ratios relative to the wild type fibrinogen concentration is A) 1:55, B) 1:110, C) 1:100, D) 1:100, E) 1:55, F) 1:83, G) 1:80, H) 1:89, I) 1:44, J) 1:67, K) 1:100, L) 1:103 (scale bar 10 μm).

A

Fibrinogen Concentration (mg/mL)	SEM Diameter (nm)	STORM Diameter (nm)	P-Value
0.5	157 ± 34 (n=225)	173 ± 35 (n=140)	4.16e-5
1	218 ± 40 (n=212)	218 ± 52 (n=128)	0.93 (ns)
3	244 ± 43 (n=252)	242 ± 41 (n=202)	0.73 (ns)
5	258 ± 47 (n=230)	251 ± 41 (n=153)	0.13 (ns)

B

Fibrinogen Concentration (mg/mL)	SEM Diameter (nm)	STORM Diameter (nm)	P-Value
0.5	102 ± 20 (n=190)	110 ± 24 (n=127)	1.4e-3
1	114 ± 23 (n=240)	117 ± 16 (n=19)	0.45 (ns)
3	180 ± 32 (n=191)	153 ± 26 (n=61)	1.07e-9
5	201 ± 35 (n=169)	176 ± 31 (n=85)	1.11e-8

C

Fibrinogen Concentration (mg/mL)	SEM Diameter (nm)	STORM Diameter (nm)	P-Value
0.5	94 ± 17 (n=121)	101 ± 22 (n=79)	0.02
1	109 ± 18 (n=145)	114 ± 37 (n=41)	0.44 (ns)
3	136 ± 19 (n=126)	138 ± 32 (n=87)	0.56 (ns)
5	165 ± 30 (n=119)	165 ± 28 (n=60)	0.96 (ns)

Table C.1: Diameter values obtained using SEM imaging and STORM imaging for fibrinogen concentrations of 0.5, 1, 3, and 5 mg/mL, at thrombin concentrations of A) 0.1 U/mL, B) 1 U/mL, and C) 5 U/mL (uncertainty is standard error; number of measurements provided in parentheses; p-values obtained using two-sample t-test assuming unequal variance with significance threshold of 0.05).

Although identical preparation was used for both samples imaged with SEM for each clot condition, sample preparation requires drying, fixation, sputter coating, and imaging in vacuum, and slight alterations at any step could lead to differing fiber diameters between the two samples. To test this, we compared the diameter values obtained from the two imaged samples at each investigated concentration in order to determine that there were not significant differences between the samples. As seen by the p-values in Table C.2, there was not a significant difference between the diameter values obtained for the two separate samples for nearly all of the investigated clot conditions. For the three clot conditions in which the p-values show that there is a significant difference, the average diameter ± standard deviation still overlaps for the two samples. It makes sense that the sample with the largest difference is that with 0.5 mg/mL fibrinogen and 0.1 NIH-U/mL thrombin, as we would expect the most heterogeneity with the lowest concentrations. Since the diameter values agree so well between the two samples for most concentrations, there does not appear to be differences caused by the sample preparation.

Concentrations of Fibrinogen and Thrombin	**Sample 1 Average Diameter ± SD (nm)**	**Sample 2 Average Diameter ± SD (nm)**	**P-Value of Diameters Between Two Samples**
0.5 mg/mL + 0.1 U/mL	164 ± 37	145 ± 23	2.6e-6
1 mg/mL + 0.1 U/mL	213 ± 45	226 ± 30	0.01
3 mg/mL + 0.1 U/mL	246 ± 44	239 ± 40	0.24 (ns)
5 mg/mL + 0.1 U/mL	255 ± 51	262 ± 41	0.21 (ns)
0.5 mg/mL + 1 U/mL	102 ± 22	102 ± 16	0.99 (ns)
1 mg/mL + 1 U/mL	111 ± 22	119 ± 24	0.02
3 mg/mL + 1 U/mL	181 ± 34	180 ± 29	0.79 (ns)
5 mg/mL + 1 U/mL	204 ± 35	195 ± 34	0.11 (ns)
0.5 mg/mL + 5 U/mL	93 ± 20	94 ± 15	0.83 (ns)
1 mg/mL + 5 U/mL	109 ± 18	111 ± 18	0.33 (ns)
3 mg/mL + 5 U/mL	135 ± 19	136 ± 19	0.90 (ns)
5 mg/mL + 5 U/mL	164 ± 36	166 ± 27	0.76 (ns)

Table C.2: Average diameter ± standard deviation (SD) for two separate SEM samples at each concentration and p-values of diameter between two separate samples (p-values determined using a two-sample t-test assuming unequal variances with significance threshold of 0.05).

C.3: Effects of Varying AlexaFluor-647-Labeled Fibrinogen Concentration

In order to determine the effect of changing AlexaFluor-647 concentrations on the STORM diameter measurements, turbidity measurements were performed in triplicate on clots containing ratios of 1:25, 1:45, 1:65, 1:85, and 1:100 of AlexaFluor-647-labeled fibrinogen to wild type fibrinogen. The results are shown in Figure C.6. Since the maximum absorbance value corresponds to the fiber diameter, the p-values were determined for the maximum absorbance value between each fluorophore concentration and the control containing no Alexa, as shown in Table C.3. The differences were statistically insignificant except for the 1:25 ratio of fluorophore labeled fibrinogen to wild type fibrinogen. Since the lowest ratio used for STORM sample preparation was 1:44, it should not have caused a significant difference in the diameter estimation.

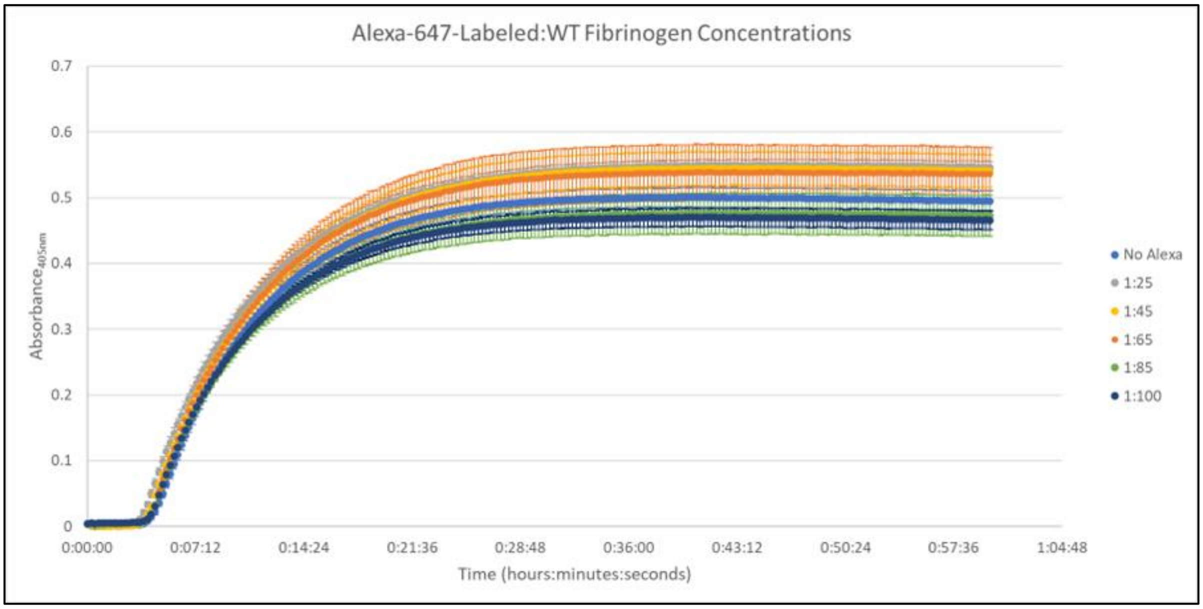

Fig. C.6: Turbidity measurements on samples containing 1:25, 1:45, 1:65, 1:85, and 1:100 ratios of AlexaFluor-647-labeled fibrinogen to wild type fibrinogen concentrations, as well as a control containing no fluorophore (Error bars represent standard deviation).

Ratio of AlexaFluor-647-Labeled Fibrinogen to Wild Type Fibrinogen	**Max Absorbance P-Value**
1:25	0.02
1:45	0.08 (ns)
1:65	0.28 (ns)
1:85	0.30 (ns)
1:100	0.06 (ns)

Table C.3: Significance levels of max absorbance from polymerization curves between the control with no fluorophore and each investigated ratio of AlexaFluor-647-labeled fibrinogen to wild type fibrinogen (p-values determined using two-sample t-test assuming unequal variances with a significance threshold of 0.05).

To further test the effect of changing fluorophore concentration on the diameter estimation according to STORM analysis, we created a MATLAB code which simulated a circular fiber cross-section of 195 nm, filled with circular protofibrils of 5 nm diameter. To avoid overcomplicating the situation, we did not account for the non-uniform internal structure of the fiber [66], but rather assumed that the protofibrils were spaced evenly to fill the fiber cross-section. We then randomly selected a certain fraction of the protofibrils to represent the fraction that would be fluorophore-labeled and recorded the distance between the far edges of the two furthest apart fluorophore-labeled protofibrils, as shown in Figure C.7, which corresponded to the measured diameter. We repeated this for 1,000 iterations, then took the average of the 1,000 fiber diameters. These diameter measurement values can be seen in Table C.4 for each investigated ratio of fluorophore-labeled fibrinogen to wild type fibrinogen.

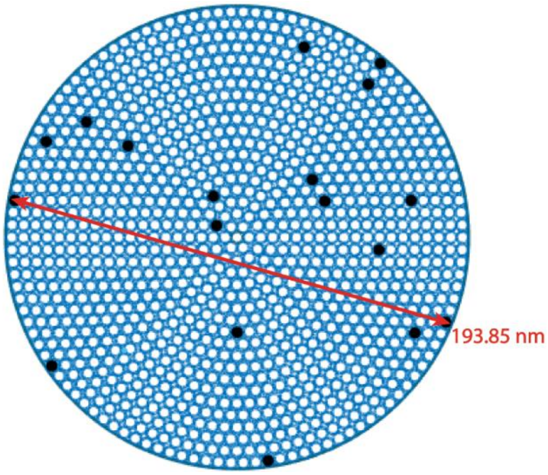

Fig. C.7: A simulated circular cross-section of a fiber with a diameter of 195 nm, filled with protofibrils of 5 nm diameter, with 1/65 the protofibrils randomly selected (filled black) and the longest distance between the edges of two selected protofibrils noted in red.

Ratio of Fluorophore-Labeled to Wild Type Fibrinogen	Simulated Average Diameter (nm)	Percent Error
1:25	191 ± 4	1.9
1:45	187 ± 7	3.9
1:65	182 ± 10	6.7
1:85	177 ± 12	9.1
1:100	174 ± 13	10.6
1:110	172 ± 14	11.6

Table C.4: A simulated circular cross-section of a fibrin fiber with a diameter of 195 nm, filled with protofibrils of 5 nm diameter.

As expected, with decreasing amounts of fluorophore-labeled fibrinogen, the error in the measured fiber diameters increases. However, when looking at the average diameters ± standard deviation, there is overlap between all of the samples except those with ratios of 1:25 and 1:110. Since the largest and smallest ratios used in our STORM samples were 1:44 and 1:110, respectively, this means that there should not have been a considerable difference in the obtained fiber diameters between the samples based on the amount of fluorophore added.

This simulation is also assuming that we are able to perfectly measure the center points of each protofibril. When you account for the resolution limitations of STORM (20 nm), the measurements would actually not be so precise, resulting in the measurements being slightly larger than those simulated. Furthermore, the simulation assumes that we are measuring a perfect cross-section of the fiber. However, we are often imaging perpendicular to the fiber rather than through the cross-section, which would result in our image containing information from the entire thickness of the fiber projected together. Therefore, our actual error should be less than that simulated, implying that there is not very much error in the diameter measurements despite the chosen fluorophore concentrations.

C.4: Pore Size Measurements

When using the bubble method to determine the pore size from confocal images, the program would include measurements that were due to a region where the fluorescence wasn't completely filled in rather than from an actual pore between fibers. In order to remove these values, a manual measurement was performed on the smallest visible pore in the confocal images for each sample concentration using the line measurement tool in ImageJ in order to determine what the smallest pore size should be. The pore size measurements obtained using the bubble method were then filtered so that any values lower than the established minimum were removed. These minimum pore size values are provided in Table C.5 for each fibrinogen/thrombin concentration.

Fibrinogen + Thrombin Concentration	**Minimum Pore Size (μm)**
0.5 mg/mL + 0.1 U/mL	5.01
1 mg/mL + 0.1 U/mL	4.01
3 mg/mL + 0.1 U/mL	2.38
5 mg/mL + 0.1 U/mL	2.02
0.5 mg/mL + 1 U/mL	2.38
1 mg/mL + 1 U/mL	2.02
3 mg/mL + 1 U/mL	1.58
5 mg/mL + 1 U/mL	1.39
0.5 mg/mL + 5 U/mL	1.39
1 mg/mL + 5 U/mL	1.19
3 mg/mL + 5 U/mL	0.99
5 mg/mL + 5 U/mL	0.79

Table C.5: Minimum pore size measurements for each fibrinogen/thrombin concentration.

Figure C.8 shows plots of the pore sizes determined manually compared to those obtained using the "bubble method". The actual averages and uncertainty are shown in Table C.6, as well as the number of measurements for that method. As seen, there is good agreement between the two methods for the investigated fibrinogen and thrombin concentrations.

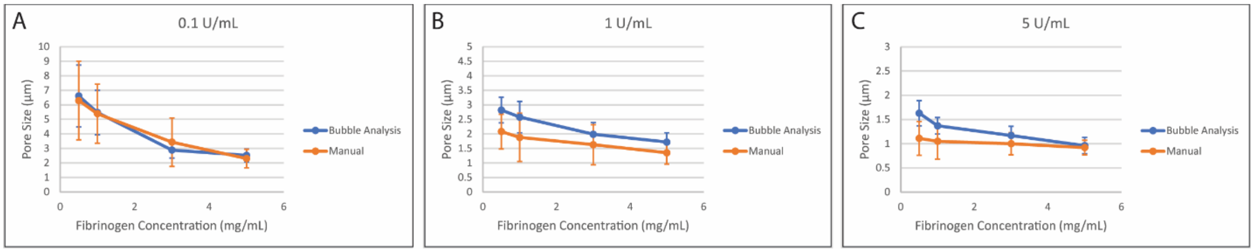

Fig. C.8: Pore sizes obtained using the "bubble method" and obtained manually using Imaris for fibrinogen concentrations of 0.5, 1, 3, and 5 mg/mL, and thrombin concentrations of A) 0.1 U/mL, B) 1 U/mL, and C) 5 U/mL (error bars represent the standard deviation).

A

Fibrinogen Concentration (mg/mL)	Bubble Analysis Pore Size (µm)	Manual Pore Size (µm)	P-Values Between Bubble Analysis and Manual Pore Sizes
0.5	6.61 ± 2.13 (n=228)	6.29 ± 2.71 (n=10)	0.73 (ns)
1	5.47 ± 1.53 (n=323)	5.39 ± 2.03 (n=10)	0.91 (ns)
3	2.88 ± 0.54 (n=730)	3.43 ± 1.67 (n=10)	0.36 (ns)
5	2.52 ± 0.44 (n=1152)	2.30 ± 0.64 (n=10)	0.33 (ns)

B

Fibrinogen Concentration (mg/mL)	Bubble Analysis Pore Size (µm)	Manual Pore Size (µm)	P-Values Between Bubble Analysis and Manual Pore Sizes
0.5	2.82 ± 0.44 (n=488)	2.08 ± 0.60 (n=10)	0.006
1	2.58 ± 0.54 (n=606)	1.88 ± 0.83 (n=10)	0.04
3	1.99 ± 0.40 (n=1142)	1.63 ± 0.69 (n=10)	0.16 (ns)
5	1.72 ± 0.32 (n=2054)	1.35 ± 0.39 (n=10)	0.02

C

Fibrinogen Concentration (mg/mL)	Bubble Analysis Pore Size (µm)	Manual Pore Size (µm)	P-Values Between Bubble Analysis and Manual Pore Sizes
0.5	1.63 ± 0.26 (n=1514)	1.11 ± 0.35 (n=10)	0.002
1	1.37 ± 0.17 (n=2115)	1.05 ± 0.37 (n=10)	0.03
3	1.17 ± 0.19 (n=3616)	1.00 ± 0.23 (n=10)	0.05 (ns)
5	0.96 ± 0.17 (n=5988)	0.92 ± 0.15 (n=10)	0.41 (ns)

Table C.6: Pore size measurements obtained using the "bubble method" and obtained manually using Imaris for fibrinogen concentrations of 0.5, 1, 3, and 5 mg/mL, at thrombin concentrations of A) 0.1 U/mL, B) 1 U/mL, and C) 5 U/mL (number of measurements provided in parentheses; p-values determined using a two-sample t-test assuming unequal variances with significance threshold of 0.05).

C.5: Turbidimetric Fitting Plots

The methods of performing turbidimetry analysis of a fibrin clot is shown in Figure C.9.

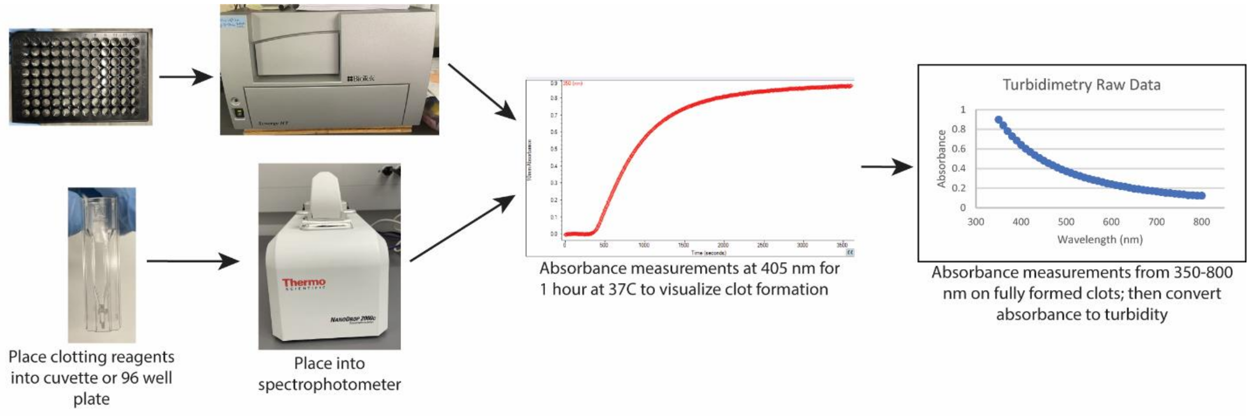

Place clotting reagents into cuvette or 96 well plate

Place into spectrophotometer

Absorbance measurements at 405 nm for 1 hour at 37C to visualize clot formation

Absorbance measurements from 350-800 nm on fully formed clots; then convert absorbance to turbidity

Fig. C.9: Methods for taking turbidimetry measurements of fibrin clot.

A representative turbidimetric fitting plot for each approach, with the corresponding fit line, can be seen in Figure C.10. For the Carr-Hermans and Yeromonahos plots, the linear fit line corresponding to the wavelength range of 350-650 nm is shown in orange and the fit line for a wavelength range of 500-800 nm is shown in gray. The R squared values for the fit line is shown in orange for a wavelength range of 350-650 nm, in gray for a wavelength range of 500-800 nm, and in blue for a wavelength range of 350-800 nm. As seen, with the exception of the Ferri approach, the wavelength range of 350-800 nm has the lowest R squared value for all plots.

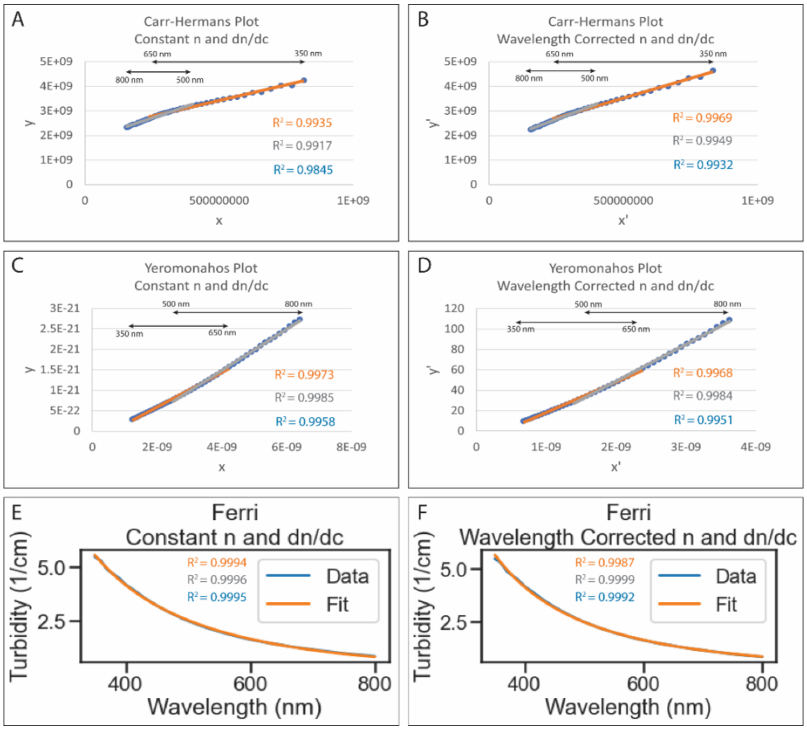

Fig. C.10: Representative turbidimetric plots for each of the approaches, in the appropriate plotting format for using constant values of n and dn/dc (left column) and for using wavelength corrected values of n and dn/dc (right column) (R squared values shown in orange for wavelength range of 350-650 nm, in gray for 500-800 nm, and in blue for 350-800 nm; dataset for 1 mg/mL fibrinogen with 0.1 U/mL thrombin and 25 L-U/mL FXIIIa taken in a cuvette using a wavelength range of 350-800 nm; for Carr-Hermans plots $x = \frac{1}{\lambda^2}, x' = \frac{n(\lambda)^2}{\langle n\rangle^2}\frac{1}{\lambda^2}, y = \frac{c}{\tau\lambda^3}, y' = \frac{\left(dn/dc(\lambda)\right)^2}{\langle dn/dc\rangle^2}\frac{n(\lambda)}{\langle n\rangle}\frac{c}{\tau\lambda^3}$; for the Yeromonahos plots, $x = \lambda^2, x' = \frac{\lambda^2}{n(\lambda)^2}, y = \tau\lambda^5, y' = \frac{\tau\lambda^5}{\left(\frac{88}{15}\right)\pi^3 n(\lambda)^3 \frac{c}{N_A}\left[\left(\frac{dn}{dc}\right)(\lambda)\right]^2}$).

The squared correlation coefficient for each clot condition are shown in Figure C.11, with the approach with the best correlation for each condition highlighted in green.

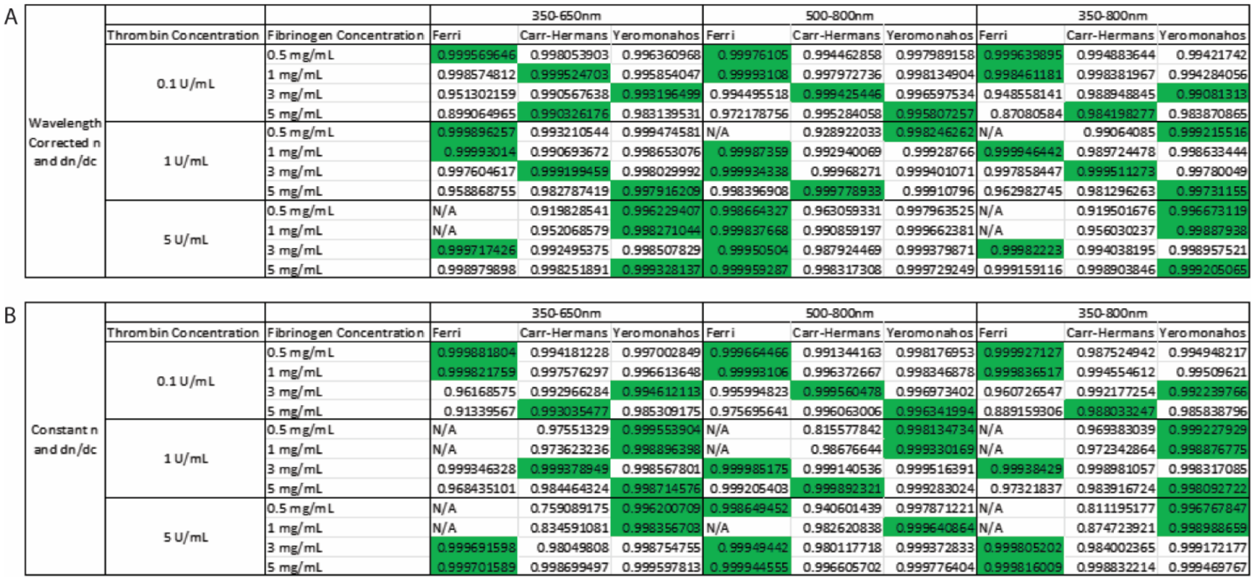

A

			350-650nm			500-800nm			350-800nm		
	Thrombin Concentration	Fibrinogen Concentration	Ferri	Carr-Hermans	Yeromonahos	Ferri	Carr-Hermans	Yeromonahos	Ferri	Carr-Hermans	Yeromonahos
Wavelength Corrected n and dn/dc	0.1 U/mL	0.5 mg/mL	**0.999569646**	0.998053903	0.996360968	**0.99976105**	0.994462858	0.997989158	**0.999639895**	0.994883644	0.99421742
		1 mg/mL	0.998574812	**0.999524703**	0.995854047	**0.99993108**	0.997972736	0.998134904	**0.998461181**	0.998381967	0.994284056
		3 mg/mL	0.951302159	0.990567638	**0.993196499**	0.994495518	**0.999425446**	0.996597534	0.948558141	0.988948845	**0.99081313**
		5 mg/mL	0.899064965	**0.990326176**	0.983139531	0.972178756	0.995284058	**0.995807257**	0.87080584	**0.984198277**	0.983870865
	1 U/mL	0.5 mg/mL	**0.999896257**	0.993210544	0.999474581	N/A	0.928922033	**0.998246262**	N/A	0.99064085	**0.999215516**
		1 mg/mL	**0.99993014**	0.990693672	0.998653076	**0.99987359**	0.992940069	0.99928766	**0.999946442**	0.989724478	0.998633444
		3 mg/mL	0.997604617	**0.999199459**	0.998029992	**0.999934338**	0.99968271	0.999401071	0.997858447	**0.999511273**	0.99780049
		5 mg/mL	0.958868755	0.982787419	**0.997916209**	0.998396908	**0.999778933**	0.99910796	0.962982745	0.981296263	**0.99731155**
	5 U/mL	0.5 mg/mL	N/A	0.919828541	**0.996229407**	**0.998664327**	0.963059331	0.997963525	N/A	0.919501676	**0.996673119**
		1 mg/mL	N/A	0.952068579	**0.998271044**	**0.999837668**	0.990859197	0.999662381	N/A	0.956030237	**0.99887938**
		3 mg/mL	**0.999717426**	0.992495375	0.998507829	**0.99950504**	0.987924469	0.999379871	**0.99982223**	0.994038195	0.998957521
		5 mg/mL	0.998979898	0.998251891	**0.999328137**	**0.999959287**	0.998317308	0.999729249	0.999159116	0.998903846	**0.999205065**

B

			350-650nm			500-800nm			350-800nm		
	Thrombin Concentration	Fibrinogen Concentration	Ferri	Carr-Hermans	Yeromonahos	Ferri	Carr-Hermans	Yeromonahos	Ferri	Carr-Hermans	Yeromonahos
Constant n and dn/dc	0.1 U/mL	0.5 mg/mL	**0.999881804**	0.994181228	0.997002849	**0.999664466**	0.991344163	0.998176953	**0.999927127**	0.987524942	0.994948217
		1 mg/mL	**0.999821759**	0.997576297	0.996613648	**0.99993106**	0.996372667	0.998346878	**0.999836517**	0.994554612	0.99509621
		3 mg/mL	0.96168575	0.992966284	**0.994612113**	0.995994823	**0.999560478**	0.996973402	0.960726547	0.992177254	**0.992239766**
		5 mg/mL	0.91339567	**0.993035477**	0.985309175	0.975695641	0.996063006	**0.996341994**	0.889159306	**0.988033247**	0.985838796
	1 U/mL	0.5 mg/mL	N/A	0.97551329	**0.999553904**	N/A	0.815577842	**0.998134734**	N/A	0.969383039	**0.999227929**
		1 mg/mL	N/A	0.973623236	**0.998896398**	N/A	0.98676644	**0.999330169**	N/A	0.972342864	**0.998876775**
		3 mg/mL	0.999346328	**0.999378949**	0.998567801	**0.999985175**	0.999140536	0.999516391	**0.99938429**	0.998981057	0.998317085
		5 mg/mL	0.968435101	0.984464324	**0.998714576**	0.999205403	**0.999892321**	0.999283024	0.97321837	0.983916724	**0.998092722**
	5 U/mL	0.5 mg/mL	N/A	0.759089175	**0.996200709**	**0.998649452**	0.940601439	0.997871221	N/A	0.811195177	**0.996767847**
		1 mg/mL	N/A	0.834591081	**0.998356703**	N/A	0.982620838	**0.999640864**	N/A	0.874723921	**0.998988659**
		3 mg/mL	**0.999691598**	0.98049808	0.998754755	**0.99949442**	0.980117718	0.999372833	**0.999805202**	0.984002365	0.999172177
		5 mg/mL	**0.999701589**	0.998699497	0.999597813	**0.999944555**	0.996605702	0.999776404	**0.999816009**	0.998832214	0.999469767

Fig. C.11: The squared correlation coefficient for each of the turbidimetric approaches at wavelength ranges of 350-650 nm, 500-800 nm, and 350-800 nm, A) with the wavelength dependence of n and dn/dc accounted for and B) using constant values of n and dn/dc. The highest squared correlation coefficient for each clot condition is highlighted in green.

C.6: Effect of Error in Pore Size and Mass Fractal Dimension

Ferri et al determined through simulations that error in the pore size and mass fractal dimension doesn't have a very large impact on the determination of the diameter if the fibers are relatively large (≥100 nm), but that inaccurate values of the mass fractal dimension causes a large amount of error in the diameter calculations for thin fibers (≤50 nm).

We decided to test this ourselves by applying a 10% increase or decrease to the average mass fractal dimension and pore size values for three clot conditions and seeing how it impacted the calculation of the diameter, as shown in Tables C.7 and C.8 below. We found similar trends to those reported by Ferri et al. [18] that variations in the mass fractal dimension have increased effects on the diameter calculations as the fibers become thinner, and that the effect of variations in the pore size does not cause a very large difference in the diameter calculations.

Sample Concentrations	**SEM Diameter (nm)**	**Ferri Diameter 10% Underestimate for D_m**	**Ferri Diameter Original D_m**	**Ferri Diameter 10% Overestimate for D_m**
5 mg/mL + 0.1 U/mL	258	283.9	282.2	281.2
3 mg/mL + 1 U/mL	180	212.7	200.5	186.5
0.5 mg/mL + 5 U/mL	94	139.0	114.8	51.8

Table C.7: The effect of a 10% increase/decrease in the mass fractal dimension on fiber diameter calculations for three clot conditions (using wavelength corrected n and dn/dc and a wavelength range of 500-800 nm).

Sample Concentrations	**SEM Diameter (nm)**	**Ferri Diameter 10% Underestimate for ξ**	**Ferri Diameter Original ξ**	**Ferri Diameter 10% Overestimate for ξ**
5 mg/mL + 0.1 U/mL	258	280.5	282.2	283.7
3 mg/mL + 1 U/mL	180	206.5	200.5	195.5
0.5 mg/mL + 5 U/mL	94	124.4	114.8	105.3

Table C.8: The effect of a 10% increase/decrease in the pore size on fiber diameter calculations for three clot conditions (using wavelength corrected n and dn/dc and a wavelength range of 500-800 nm).

We then tested how these two parameters vary between different clot locations. We did this by analyzing a stack of confocal images taken at 2-3 different locations. For 4/12 of the investigated clot conditions, two image stacks were analyzed, with each from different samples at the same concentrations. For 8/12 of the investigated clot conditions, three image stacks were analyzed, with one of the image stacks coming from one sample and two of the image stacks coming from a second sample at the same concentrations.

The difference in the mass fractal dimension at the different clot locations for each investigated concentration is represented by the p-values in Table C.9. While there is a significant difference in the obtained mass fractal dimensions between the different imaged locations for the majority of the samples according to the p-values, the average percent difference between the mass fractal dimension at the various locations was only 2.4%, with the maximum difference being 6.5%. Therefore, the effect of the varying mass fractal dimension with changing clot location should not have as drastic of an impact on the diameter calculations using the Ferri approach as suggested by the analysis above.

Concentrations of Fibrinogen and Thrombin	**Sample 1 Average Mass Fractal Dimension ± SD**	**Sample 2 Average Mass Fractal Dimension ± SD**	**Sample 3 Average Mass Fractal Dimension ± SD**	**P-Value of Mass Fractal Dimension Between Samples**
0.5 mg/mL + 0.1 U/mL	1.43 ± 0.09	1.42 ± 0.08	1.41 ± 0.03	0.60 (ns)
1 mg/mL + 0.1 U/mL	1.36 ± 0.03	1.39 ± 0.03	1.43 ± 0.01	2e-13
3 mg/mL + 0.1 U/mL	1.65 ± 0.02	1.584 ± 0.009	N/A	4e-7
5 mg/mL + 0.1 U/mL	1.64 ± 0.01	1.736 ± 0.006	N/A	2e-21
0.5 mg/mL + 1 U/mL	1.56 ± 0.06	1.65 ± 0.04	1.64 ± 0.02	7e-9
1 mg/mL + 1 U/mL	1.66 ± 0.01	1.73 ± 0.01	N/A	4e-22
3 mg/mL + 1 U/mL	1.71 ± 0.02	1.74 ± 0.02	N/A	4e-4
5 mg/mL + 1 U/mL	1.73 ± 0.01	1.775 ± 0.004	1.770 ± 0.006	3e-23
0.5 mg/mL + 5 U/mL	1.75 ± 0.05	1.76 ± 0.04	1.87 ± 0.02	8e-14
1 mg/mL + 5 U/mL	1.76 ± 0.02	1.77 ± 0.02	1.74 ± 0.02	6e-5
3 mg/mL + 5 U/mL	1.842 ± 0.009	1.81 ± 0.02	1.86 ± 0.01	5e-12
5 mg/mL + 5 U/mL	1.853 ± 0.008	1.86 ± 0.03	1.86 ± 0.02	0.77 (ns)

Table C.9: Average mass-fractal dimension ± standard deviation (SD) and p-values of the mass-fractal dimension between different clot locations according to confocal imaging analysis (p-values determined using a single factor ANOVA test when there were three images compared and using a two-sample t-test assuming unequal variances when two images were compared, significance threshold of 0.05; N/A under sample 3 means only two locations were imaged for that concentration).

We also analyzed how the pore size changed for a single clot condition depending on the location of imaging (using the bubble method described in Chapter 3 to determine the pore size), finding that on average there was a 4.4% difference in the pore size between sample locations. Since it was found in the analysis above that up to a 10% difference in the pore size has very little impact on the obtained fiber diameter with the Ferri approach, this variability should not have had a significant impact on the diameter estimations.

Since the mass fractal dimension needs to be known very accurately in order for the Ferri approach to provide accurate diameter estimations, and the mass fractal dimension varies significantly with the location of imaging, this is one possible cause of the Ferri fitting approach not working as well as the other approaches for some clot conditions. However, the large impact of the mass fractal dimension should be most prevalent for thin fibers, and there are some cases where the fiber diameter was thick, but the Ferri approach still did not work well, so this is not the only explanation for the poor accuracy of the Ferri fitting approach in our analysis.

C.7: Cuvette vs. 96 Well Plate

Plots showing the percent error in the diameter value obtained using each of turbidimetric approaches compared to the values according to SEM imaging can be seen in Figure C.12 versus fiber diameter for measurements taken in both a cuvette and a 96 well plate. Those plots show that there is no clear trend for which diameter values measurements taken in a cuvette or 96 well plate are more accurate.

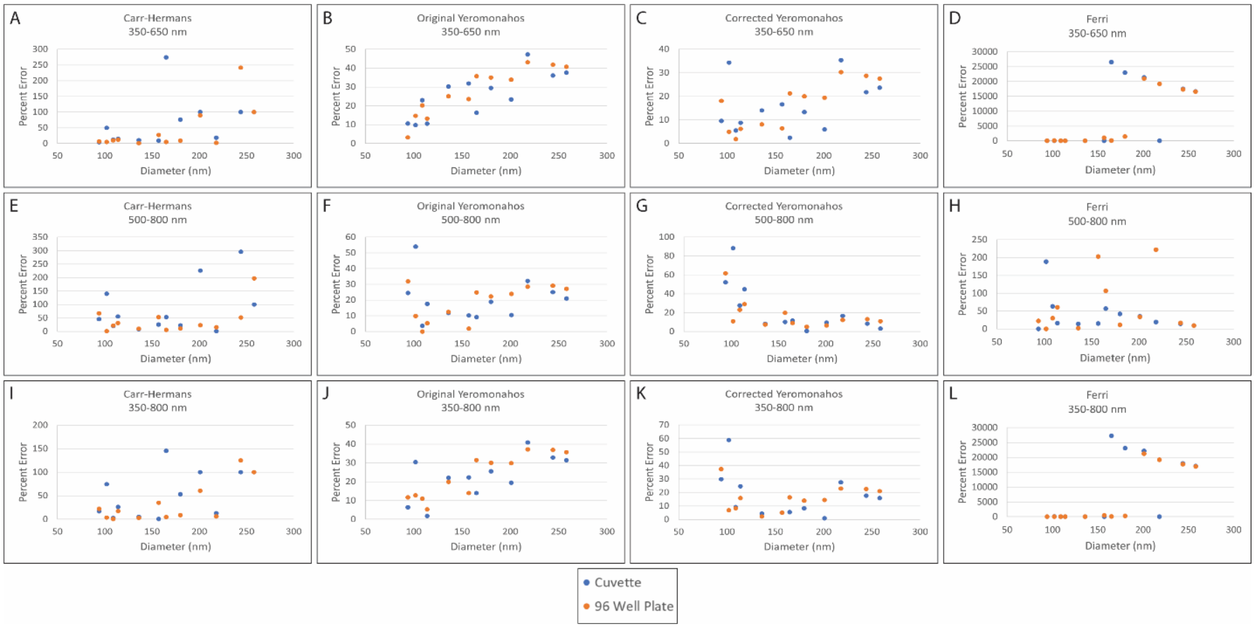

Fig. C.12: The percent error versus diameter for each turbidimetric fitting approaches using a cuvette (blue) and 96 well plate (orange) for measurements, with a wavelength range of 350-650 nm (top row), 500-800 nm (middle row), and 350-800 nm (bottom row) (wavelength dependence of n and dn/dc accounted for).

Figure C.13 shows plots of the percent error in the diameter values obtained using each turbidimetric approach compared to those obtained from SEM imaging versus fibrinogen concentration for measurements performed in both a cuvette and 96 well plate. Based on those plots, there is no clear trend on which fibrinogen concentrations either a cuvette or 96 well plate provides more accurate diameter values.

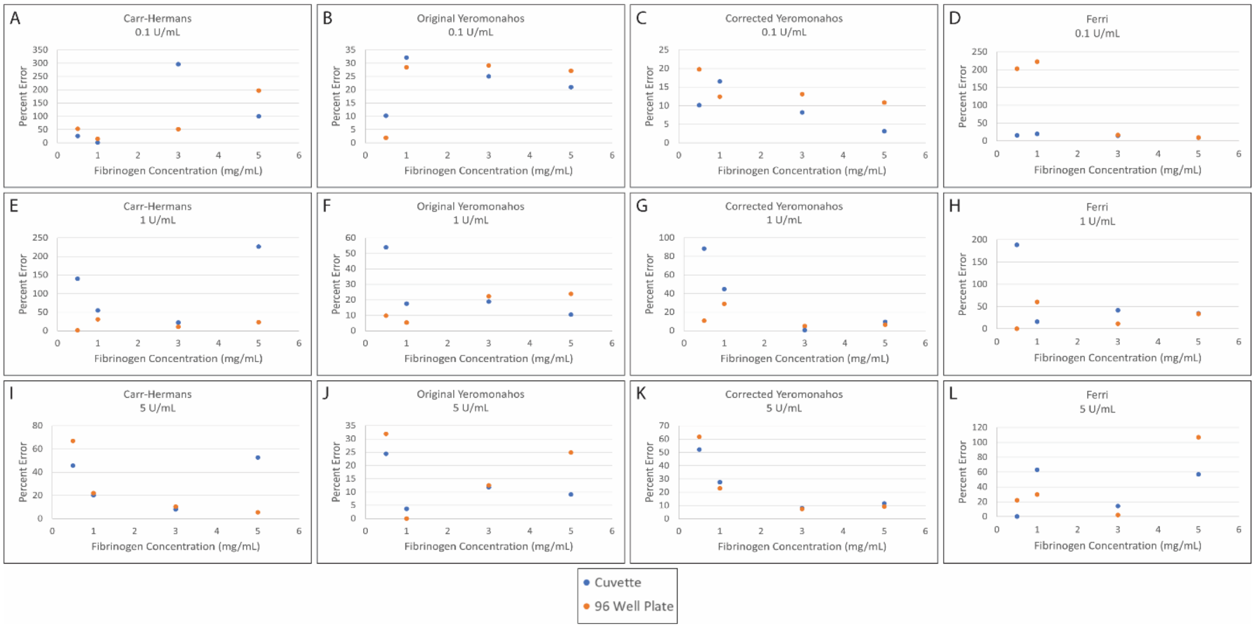

Fig. C.13: The percent error versus fibrinogen concentration for each turbidimetric fitting approaches using a cuvette (blue) and 96 well plate (orange) for measurements, for thrombin concentrations of 0.1 U/mL (top row), 1 U/mL (middle row), and 5 U/mL (bottom row) (wavelength range of 500-800 nm, with the wavelength dependence of n and dn/dc accounted for).

Figure C.14 shows a color-coded table of the percent error in the diameter values obtained using each turbidimetric approach compared to those obtained from SEM imaging for each investigated clot condition using both a cuvette and 96 well plate. The differences between the results when using a cuvette and when using a 96 well plate is discussed in more detail in the main text (see Chapter 3).

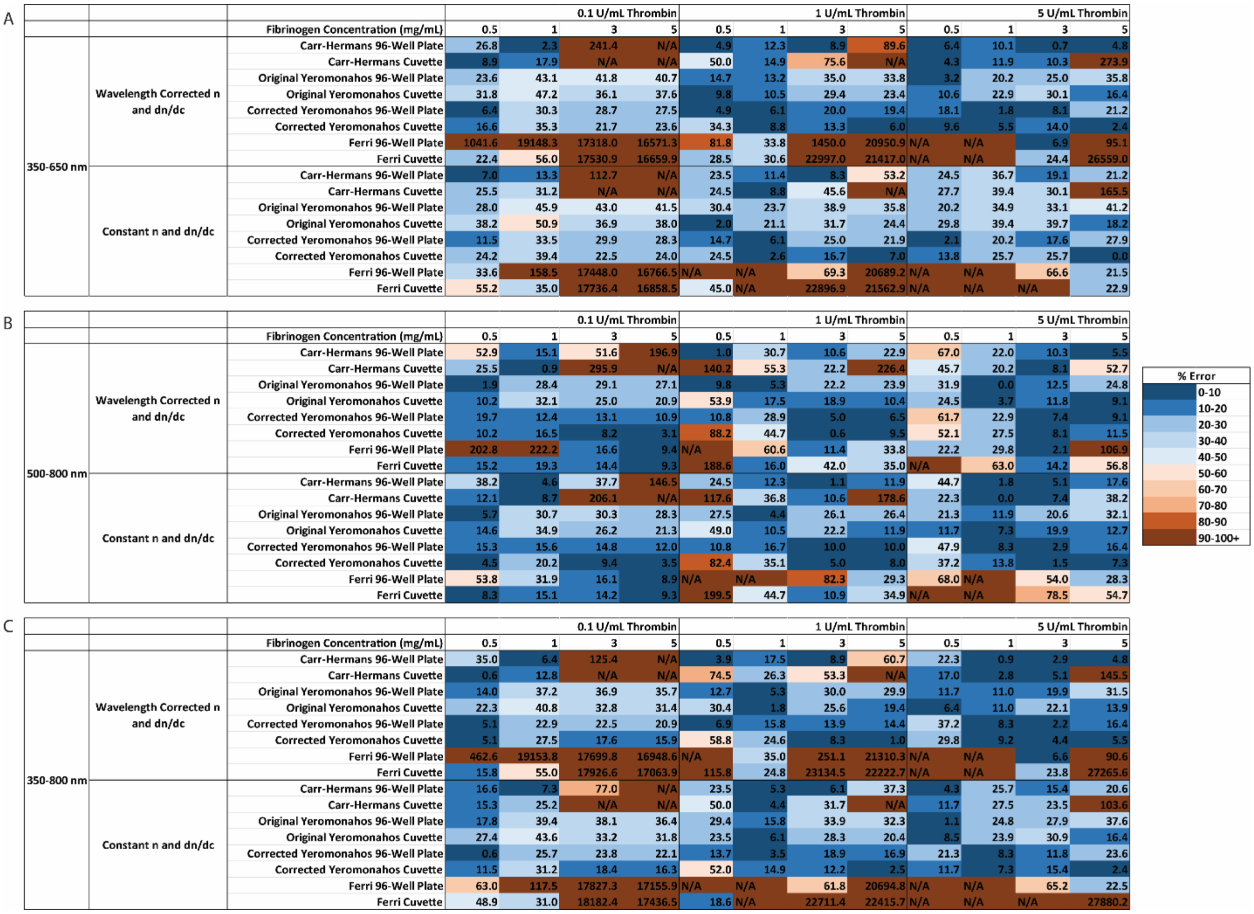

A

			0.1 U/mL Thrombin				1 U/mL Thrombin				5 U/mL Thrombin			
		Fibrinogen Concentration (mg/mL)	0.5	1	3	5	0.5	1	3	5	0.5	1	3	5
350-650 nm	Wavelength Corrected n and dn/dc	Carr-Hermans 96-Well Plate	26.8	2.3	241.4	N/A	4.9	12.3	8.9	89.6	6.4	10.1	0.7	4.8
		Carr-Hermans Cuvette	8.9	17.9	N/A	N/A	50.0	14.9	75.6	N/A	4.3	11.9	10.3	273.9
		Original Yeromonahos 96-Well Plate	23.6	43.1	41.8	40.7	14.7	13.2	35.0	33.8	3.2	20.2	25.0	35.8
		Original Yeromonahos Cuvette	31.8	47.2	36.1	37.6	9.8	10.5	29.4	23.4	10.6	22.9	30.1	16.4
		Corrected Yeromonahos 96-Well Plate	6.4	30.3	28.7	27.5	4.9	6.1	20.0	19.4	18.1	1.8	8.1	21.2
		Corrected Yeromonahos Cuvette	16.6	35.3	21.7	23.6	34.3	8.8	13.3	6.0	9.6	5.5	14.0	2.4
		Ferri 96-Well Plate	1041.6	19148.3	17318.0	16571.3	81.8	33.8	1450.0	20950.9	N/A	N/A	6.9	95.1
		Ferri Cuvette	22.4	56.0	17530.9	16659.9	28.5	30.6	22997.0	21417.0	N/A	N/A	24.4	26559.0
	Constant n and dn/dc	Carr-Hermans 96-Well Plate	7.0	13.3	112.7	N/A	23.5	11.4	8.3	53.2	24.5	36.7	19.1	21.2
		Carr-Hermans Cuvette	25.5	31.2	N/A	N/A	24.5	8.8	45.6	N/A	27.7	39.4	30.1	165.5
		Original Yeromonahos 96-Well Plate	28.0	45.9	43.0	41.5	30.4	23.7	38.9	35.8	20.2	34.9	33.1	41.2
		Original Yeromonahos Cuvette	38.2	50.9	36.9	38.0	2.0	21.1	31.7	24.4	29.8	39.4	39.7	18.2
		Corrected Yeromonahos 96-Well Plate	11.5	33.5	29.9	28.3	14.7	6.1	25.0	21.9	2.1	20.2	17.6	27.9
		Corrected Yeromonahos Cuvette	24.2	39.4	22.5	24.0	24.5	2.6	16.7	7.0	13.8	25.7	25.7	0.0
		Ferri 96-Well Plate	33.6	158.5	17448.0	16766.5	N/A	N/A	69.3	20689.2	N/A	N/A	66.6	21.5
		Ferri Cuvette	55.2	35.0	17736.4	16858.5	45.0	N/A	22896.9	21562.9	N/A	N/A	N/A	22.9

B

			0.1 U/mL Thrombin				1 U/mL Thrombin				5 U/mL Thrombin			
		Fibrinogen Concentration (mg/mL)	0.5	1	3	5	0.5	1	3	5	0.5	1	3	5
500-800 nm	Wavelength Corrected n and dn/dc	Carr-Hermans 96-Well Plate	52.9	15.1	51.6	196.9	1.0	30.7	10.6	22.9	67.0	22.0	10.3	5.5
		Carr-Hermans Cuvette	25.5	0.9	295.9	N/A	140.2	55.3	22.2	226.4	45.7	20.2	8.1	52.7
		Original Yeromonahos 96-Well Plate	1.9	28.4	29.1	27.1	9.8	5.3	22.2	23.9	31.9	0.0	12.5	24.8
		Original Yeromonahos Cuvette	10.2	32.1	25.0	20.9	53.9	17.5	18.9	10.4	24.5	3.7	11.8	9.1
		Corrected Yeromonahos 96-Well Plate	19.7	12.4	13.1	10.9	10.8	28.9	5.0	6.5	61.7	22.9	7.4	9.1
		Corrected Yeromonahos Cuvette	10.2	16.5	8.2	3.1	88.2	44.7	0.6	9.5	52.1	27.5	8.1	11.5
		Ferri 96-Well Plate	202.8	222.2	16.6	9.4	N/A	60.6	11.4	33.8	22.2	29.8	2.1	106.9
		Ferri Cuvette	15.2	19.3	14.4	9.3	188.6	16.0	42.0	35.0	N/A	63.0	14.2	56.8
	Constant n and dn/dc	Carr-Hermans 96-Well Plate	38.2	4.6	37.7	146.5	24.5	12.3	1.1	11.9	44.7	1.8	5.1	17.6
		Carr-Hermans Cuvette	12.1	8.7	206.1	N/A	117.6	36.8	10.6	178.6	22.3	0.0	7.4	38.2
		Original Yeromonahos 96-Well Plate	5.7	30.7	30.3	28.3	27.5	4.4	26.1	26.4	21.3	11.9	20.6	32.1
		Original Yeromonahos Cuvette	14.6	34.9	26.2	21.3	49.0	10.5	22.2	11.9	11.7	7.3	19.9	12.7
		Corrected Yeromonahos 96-Well Plate	15.3	15.6	14.8	12.0	10.8	16.7	10.0	10.0	47.9	8.3	2.9	16.4
		Corrected Yeromonahos Cuvette	4.5	20.2	9.4	3.5	82.4	35.1	5.0	8.0	37.2	13.8	1.5	7.3
		Ferri 96-Well Plate	53.8	31.9	16.1	8.9	N/A	N/A	82.3	29.3	68.0	N/A	54.0	28.3
		Ferri Cuvette	8.3	15.1	14.2	9.3	199.5	44.7	10.9	34.9	N/A	N/A	78.5	54.7

% Error
0-10
10-20
20-30
30-40
40-50
50-60
60-70
70-80
80-90
90-100+

C

			0.1 U/mL Thrombin				1 U/mL Thrombin				5 U/mL Thrombin			
		Fibrinogen Concentration (mg/mL)	0.5	1	3	5	0.5	1	3	5	0.5	1	3	5
350-800 nm	Wavelength Corrected n and dn/dc	Carr-Hermans 96-Well Plate	35.0	6.4	125.4	N/A	3.9	17.5	8.9	60.7	22.3	0.9	2.9	4.8
		Carr-Hermans Cuvette	0.6	12.8	N/A	N/A	74.5	26.3	53.3	N/A	17.0	2.8	5.1	145.5
		Original Yeromonahos 96-Well Plate	14.0	37.2	36.9	35.7	12.7	5.3	30.0	29.9	11.7	11.0	19.9	31.5
		Original Yeromonahos Cuvette	22.3	40.8	32.8	31.4	30.4	1.8	25.6	19.4	6.4	11.0	22.1	13.9
		Corrected Yeromonahos 96-Well Plate	5.1	22.9	22.5	20.9	6.9	15.8	13.9	14.4	37.2	8.3	2.2	16.4
		Corrected Yeromonahos Cuvette	5.1	27.5	17.6	15.9	58.8	24.6	8.3	1.0	29.8	9.2	4.4	5.5
		Ferri 96-Well Plate	462.6	19153.8	17699.8	16948.6	N/A	35.0	251.1	21310.3	N/A	N/A	6.6	90.6
		Ferri Cuvette	15.8	55.0	17926.6	17063.9	115.8	24.8	23134.5	22222.7	N/A	N/A	23.8	27265.6
	Constant n and dn/dc	Carr-Hermans 96-Well Plate	16.6	7.3	77.0	N/A	23.5	5.3	6.1	37.3	4.3	25.7	15.4	20.6
		Carr-Hermans Cuvette	15.3	25.2	N/A	N/A	50.0	4.4	31.7	N/A	11.7	27.5	23.5	103.6
		Original Yeromonahos 96-Well Plate	17.8	39.4	38.1	36.4	29.4	15.8	33.9	32.3	1.1	24.8	27.9	37.6
		Original Yeromonahos Cuvette	27.4	43.6	33.2	31.8	23.5	6.1	28.3	20.4	8.5	23.9	30.9	16.4
		Corrected Yeromonahos 96-Well Plate	0.6	25.7	23.8	22.1	13.7	3.5	18.9	16.9	21.3	8.3	11.8	23.6
		Corrected Yeromonahos Cuvette	11.5	31.2	18.4	16.3	52.0	14.9	12.2	2.5	11.7	7.3	15.4	2.4
		Ferri 96-Well Plate	63.0	117.5	17827.3	17155.9	N/A	N/A	61.8	20694.8	N/A	N/A	65.2	22.5
		Ferri Cuvette	48.9	31.0	18182.4	17436.5	18.6	N/A	22711.4	22415.7	N/A	N/A	N/A	27880.2

Fig. C.14: Percent error in the diameter obtained from each investigated turbidimetric approach compared to diameters obtained from SEM for a wavelength range of A) 350-650 nm, B) 500-800 nm, and C) 350-800 nm for measurements performed in both a cuvette and a 96 well plate.

C.8: Density/Length Changes Throughout Sample Height

In order to test if the fibers toward the bottom of a sample are being compressed by the weight of the fibers on top of them, we analyzed an image stack obtained using a Bruker MuVi SPIM light sheet microscope. First, a time series was performed on a clot containing 3 mg/mL fibrinogen and 0.1 NIH-U/mL thrombin, with 1/65 the amount of AlexaFluor-647-labeled fibrinogen as wild type fibrinogen, for approximately 30 minutes or until polymerization was complete. An image stack was then obtained on the height of the sample, with a depth of 100 μm.

Analysis was performed on the reconstructed 3D image using the program Imaris. The reconstructed image contained sections where the fibers could be clearly visualized, with slightly blurred areas in between each section. In order to determine the fiber density, a 1000x1000x50 pixel section was chosen from the center of each section making up the image. The volume sum of the fibers in the selected section was then determined using the surface feature in Imaris. This was done for three separate samples, with identical settings used for analysis with each sample. The results are plotted in Figure C.15. As seen, for all three samples there is a slight increase overall in the volume density of fibers from the top of the sample to the bottom of the sample.

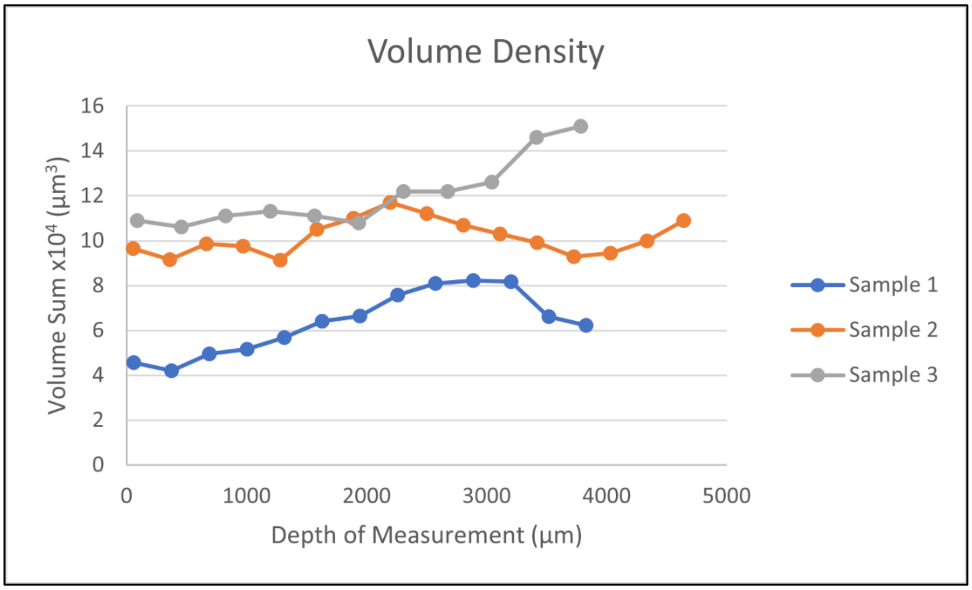

Fig. C.15: Volume sum of fibers within selected section versus the depth of the measurement (with 0 being the top of the sample) (3 mg/mL fibrinogen, 0.1 NIH-U/mL thrombin).

If the fibers are compressed toward the bottom of the sample, they would not have as much room to grow longitudinally, so it would be expected that those fibers would not be as long as those toward the top of the sample. In order to test this theory, manual fiber length measurements were performed in Imaris on one of the samples, with ten fibers measured per section of the image. The results can be seen in Figure C.16. There was a slight decrease in the average fiber length at the bottom of the sample compared to the top of the sample.

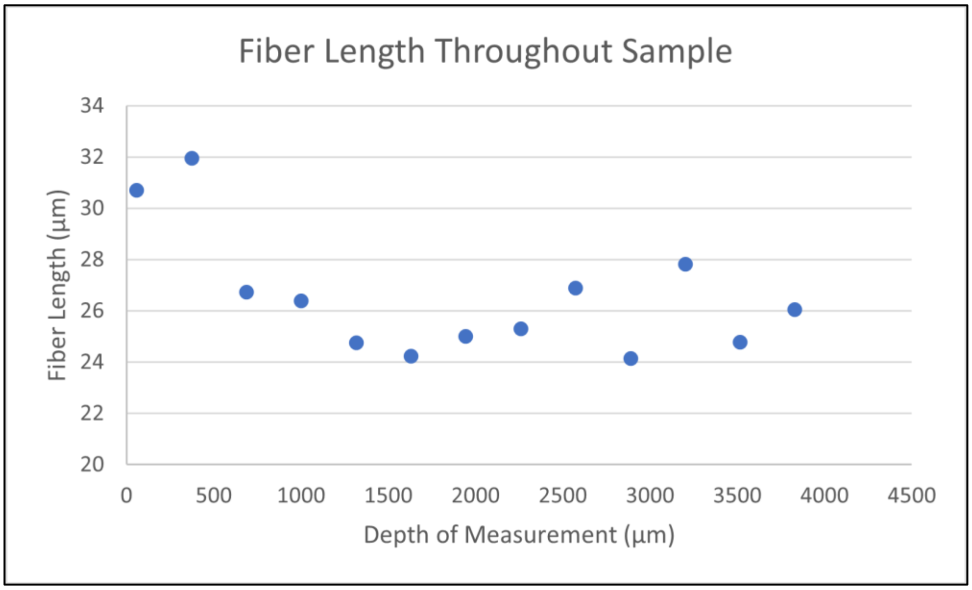

Fig. C.16: Average length of fibers versus the depth of the measurement (with 0 being the top of the sample) (3 mg/mL fibrinogen, 0.1 NIH-U/mL thrombin).

Based on these results, it appears that the fibers are shorter and more densely packed together toward the bottom of the sample than they are at the top of the sample, suggesting that the fibers at the bottom are being slightly compressed from the weight of the fibers on top of them. However, the changes could also be due to uneven mixing of thrombin, and therefore requires further analysis to be definitive. Nonetheless, the changes in density and length are very slight, and combined with the turbidity/turbidimetry analysis from Chapter 3, it does not appear that this causes a significant difference in the fiber diameter.

C.9: Uneven Light Blocking in Multiple Scattering Experiment

As shown in Figure 29, the diameter values obtained using the turbidimetric approaches were usually further from those obtained from SEM imaging when using covers in the attempt to block multiple scattered light. As seen in Figure C.17, the percent error in the obtained diameter values compared to those from SEM imaging was very large for small diameter values, with the turbidimetric approaches providing imaginary diameter values for those with average diameters of 165 nm or smaller when using two covers (plotted as 100% error).

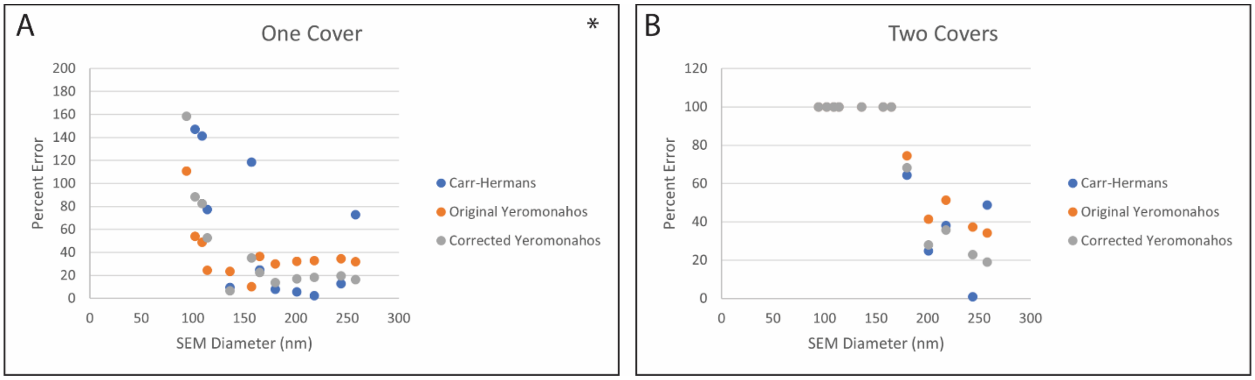

Fig. C.17: Percent error between the diameter values obtained using turbidimetry (with either the Carr-Hermans, Original Yeromonahos, or Corrected Yeromonahos approach) and those obtained from SEM imaging with A) one cover to block multiple scattered light, and B) two stacked covers to block multiple scattered light (*not all datapoints within the plot view; imaginary diameters plotted as 100% error).

These imaginary diameters are a result of some sample absorbance measurements being smaller than those of the background solution, resulting in negative absorbance values once the background is subtracted out. This could have resulted from the beam not being centered on the wells, resulting in an uneven amount of the transmitted light being blocked for different wells. If more of the light was blocked for the wells containing the background solution, this would lead to overestimates of the absorbance measurements, which could explain why the background measurements were sometimes higher than those for some samples. This would also explain why the percent error increases with increasing diameter, because as the diameter increases, the amount of light scattered increases, resulting in higher absorbance values, which would not be as sensitive to the overestimates of the background absorbance. In order to further test if part of the beam was being blocked, we compared the absorbance measurements for the background solution, which should have little to no multiple scattering, as it did not contain any fibers, only thrombin and FXIIIa. As seen in Figure C.18, there are slightly higher absorbance values when using one cover versus no cover, then even higher values when using both covers, further implying that part of the light beam is being blocked by the covers.

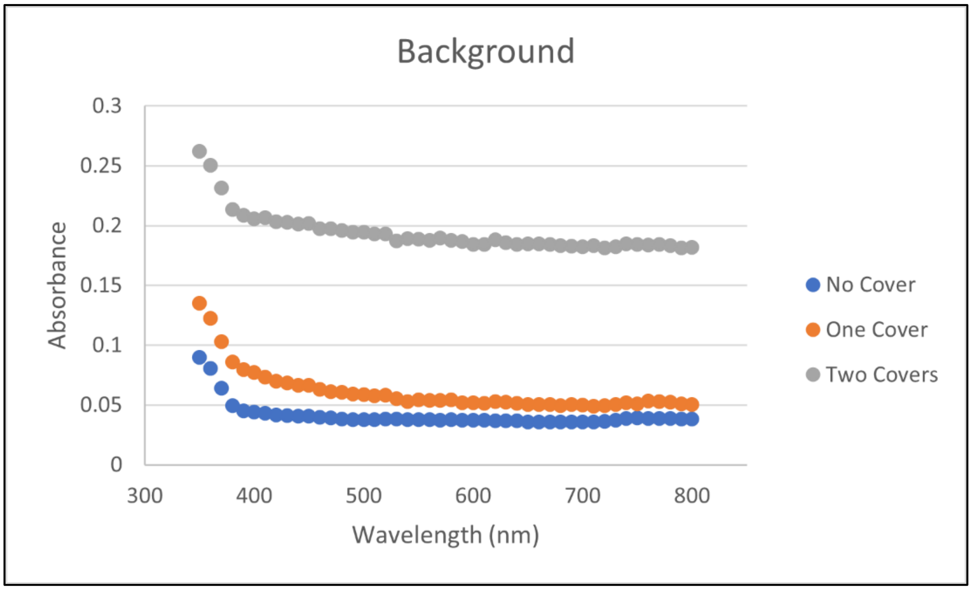

Fig. C.18: Absorbance measurements on background solution containing 25 L-U/mL FXIIIa and 5 U/mL thrombin, but with no fibrinogen, in a solution of HBS buffer with 5 mM $CaCl_2$ with no cover, one cover, or two covers.